12-2021

Development of Metamaterial-Based Near-Zero Refractive Index Structures in the Optical Regime

Andres Ochoa
The University of Texas Rio Grande Valley

DEVELOPMENT OF METAMATERIAL-BASED NEAR-ZERO REFRACTIVE INDEX STRUCTURES IN THE OPTICAL REGIME

A Thesis

by

ANDRES OCHOA

Submitted in Partial Fulfillment of the

Requirements for the Degree of

MASTER OF SCIENCE IN ENGINEERING

Major Subject: Electrical Engineering

The University of Texas Rio Grande Valley

December 2021

DEVELOPMENT OF METAMATERIAL-BASED NEAR-ZERO REFRACTIVE INDEX STRUCTURES IN THE OPTICAL REGIME

A Thesis
by
ANDRES OCHOA

COMMITTEE MEMBERS

Dr. Nantakan Wongkasem
Chair of Committee

Dr. Hasina Huq
Committee Member

Dr. Yong Zhou
Committee Member

December 2021

ABSTRACT

Ochoa, Andres, Development of Metamaterial-Based Near-Zero Refractive Index Structures in the Optical Regime. Master of Science in Engineering (MSE), December, 2021, 94 pp., 19 tables, 100 figures, references, 52 titles.

Multilayer combinations of plasmonic and dielectric materials can be designed as subwavelength structures to create a medium with unique parameters, but the development of optical metamaterials for the visible spectrum is hindered by the lack of plasmonic materials with suitable properties. A method to understand and design metamaterials for optical applications is examined as a solution for shifting the operating range from ultraviolet light to visible light. Special points of interest and corresponding parameters are identified to understand their effects on propagation. A hyperbolic near-zero refractive index metamaterial composed of alternating layers of metal and perovskite thin films is proposed for lenses and other optical devices. The results are intended to facilitate in the design of anisotropic media and selection of materials.

DEDICATION

The completion of this work would not have been possible without the support of my family. To my mother for her love and commitment for her family. The last few years have been difficult, but she worked tirelessly to provide comfort and care for her husband and sister. To my brother who has provided assistance throughout the years. To my aunt for supporting me during my undergraduate studies and following years. I have not lost hope that there are better years ahead. This work is dedicated especially to my father. He worked hard every day of his life for his mother, brothers, sisters and then for his wife and children when he started his own family. He was there when we needed him and would provide as much help as possible. I will remember all the good times we spent together. We'll just have to see each other again some other time.

ACKNOWLEDGMENTS

I give my sincerest gratitude to those whom have assisted me throughout my research. Many thanks to Dr. Wongkasem for providing guidance and encouragement during these difficult times while I was working towards my degree.

To my committee members Dr. Zhou and to Dr. Huq in providing access to laboratory resources. To Dr. Lozano and staff. To Roman Garcia, Jesus Valladares and Jorge Castillo. And to fellow colleagues throughout my graduate studies. I am very grateful for the opportunity to work with everyone.

TABLE OF CONTENTS

LIST OF TABLES

Page

LIST OF FIGURES

CHAPTER I

LITERATURE REVIEW AND MOTIVATION

In discussions of the history of metamaterials, Victor Veselago is mentioned as hypothesizing about a material with permittivity and permeability less than zero [1]. Veselago describes a coordinate system with major axes ε and μ, permittivity and permeability respectively, as shown in Figure 1.1. Most dielectrics are found in quadrant I and metals in quadrant II. These two regions encompass naturally occurring materials. [2] The materials found in quadrant III and IV are artificially created through metamaterials. Veselago's theoretical material, which he called left-handed substance, falls into quadrant III.

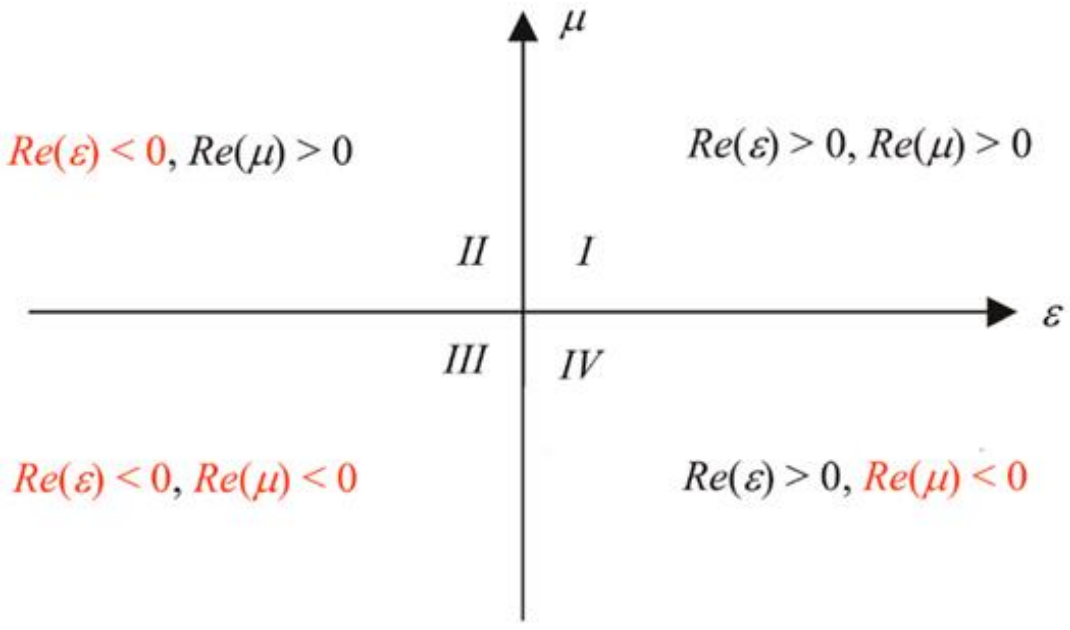

Figure 1.1: Classification of Materials on ε-μ Coordinate System [2]

In the mid-1990s, John Pendry wrote about how a structure made of infinite wires, in Figure 1.2, could control and produce negative permittivity in the Gigahertz range [3]. Pendry also developed a method to control permeability using an array of split rings on a planar structure shown in Figure 1.3 [4].

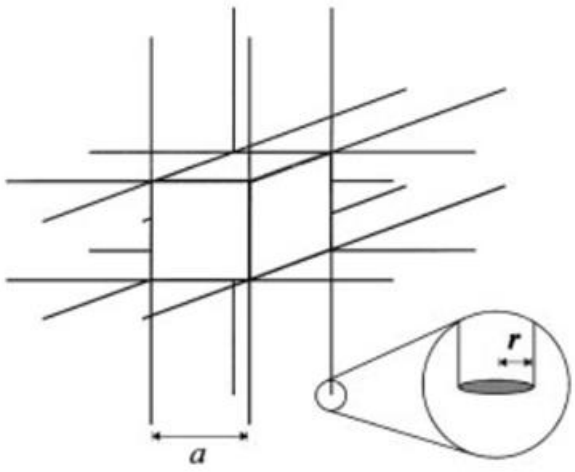

Figure 1.2: Model of Infinite Wire Structure [3]

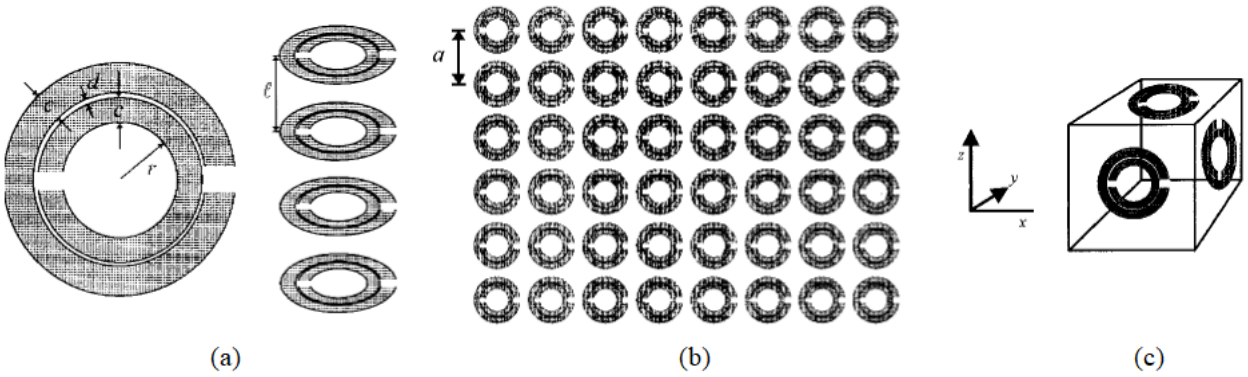

Figure 1.3: (a) Split Ring (b) Planar Array (c) Unit Cell [4]

The structure was verified by a team at UCSD, shown in Figure 1.4 [5][6][7]. These left-handed materials, known as metamaterials, are studied for their unique properties.

Figure 1.4: Construction of Metamaterial with Copper Strips and Split Rings [7]

1.1 Hyperbolic Metamaterials

Hyperbolic metamaterials have received a lot of attention in the past two decades. They are a class of metamaterials described by the hyperbolic dispersion relation in Equation 1.1 [8] where k_x, k_y *and* k_z represent the wavenumber along cartesian axes, ω is angular frequency, c is speed of light, and ε_{xx} and ε_{zz} are the lateral and perpendicular components for permittivity.

$$\frac{k_x^2 + k_y^2}{\varepsilon_{zz}} + \frac{k_z^2}{\varepsilon_{xx}} = \frac{\omega^2}{c^2} \tag{1.1}$$

Hyperbolic metamaterials are anisotropic crystals with permittivity and permeability tensors shown in Equations 1.2 and 1.3. They observe positive permittivity in certain directions and negative permittivity in others. Permeability in optical applications does not drop into the negative range nor get close to zero. It is common to set Equation 1.3 as a unit vector, however, more recent studies go further into permeability of optical metamaterials [9][10].

$$\bar{\varepsilon} = \begin{bmatrix} \varepsilon_{xx} & & \\ & \varepsilon_{yy} & \\ & & \varepsilon_{zz} \end{bmatrix} \tag{1.2}$$

$$\bar{\mu} = \begin{bmatrix} \mu_{xx} & & \\ & \mu_{yy} & \\ & & \mu_{zz} \end{bmatrix} \tag{1.3}$$

Equation 1.1 can be graphed for a specific wavelength as shown in Figure 1.5 for a Type I hyperbolic metamaterial in (b), a Type II hyperbolic metamaterial in (c) and dispersion for isotropic dielectrics in (a).

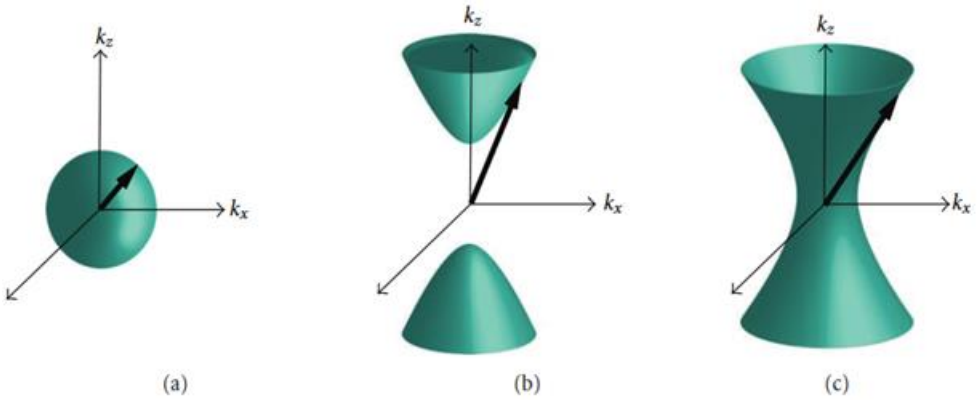

Figure 1.5: (a) Dispersion for isotropic dielectrics (b) Type I (c) Type II [11]

Type I metamaterials have positive permittivity in the x axis and y axes, $\varepsilon_{xx} > 0$ and $\varepsilon_{yy} > 0$, and negative permittivity in the z axis, $\varepsilon_{zz} > 0$. Type II metamaterials have their signs switched to have negative permittivity in the x axis and y axis, $\varepsilon_{xx} < 0$ and $\varepsilon_{yy} < 0$, and positive permittivity in the z axis, $\varepsilon_{zz} > 0$. [11]

A Type II metamaterial will reflect the incident wave [12]. Since permittivity changes with wavelength, the change in the epsilon values in the dispersion relation, Equation 1.1, will change the dispersion plots. This means that a Type I metamaterial can become a Type II metamaterial at different wavelengths.

The dispersion plot also describes the relationship between the wave vector and the Poynting vector. Shown in Figure 1.6, the Poynting vector, S, is orthogonal to the surface at the

point where the wave vector intersects the dispersion plot [9]. In this example, the wave vector has a positive angle and the resulting Poynting vector has a negative angle.

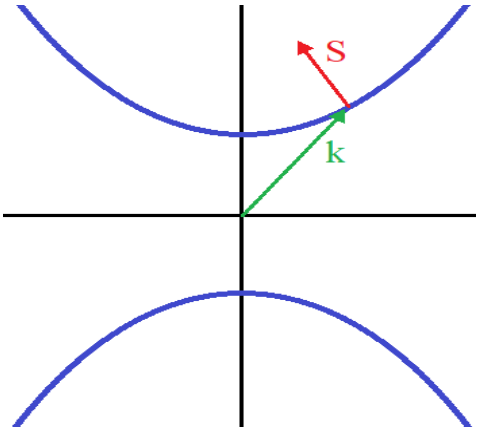

Figure 1.6: Relation Between Wave Vector and Poynting Vector

1.2 Effective Medium Theory

Hyperbolic metamaterials can take many forms, but there are two basic structures. These are multilayer thin films and nanorods, or nanowires, as shown in Figure 1.7. The size of the individual layers or rods are designed much smaller than the intended wavelength.

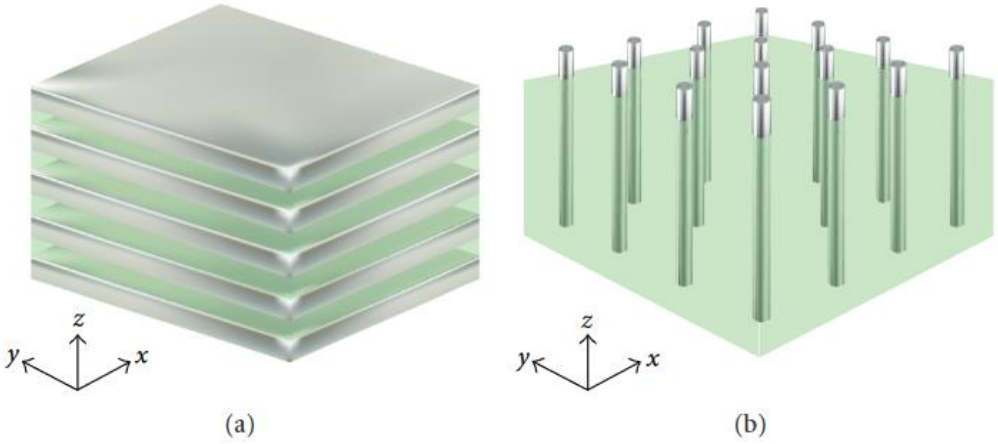

Figure 1.7: (a) Multilayer Thin Films (b) Nanorods [11]

Hyperbolic metamaterials are built as subwavelength structures where the individual thickness of the layers or the rods are significantly smaller than the desired wavelength. [11] The propagating wave sees the combination of parts as a solid material.

The values of permittivity are dependent on direction in the permittivity tensor. For multilayer thin films, Equation 1.4 relates the permittivity of the metal and dielectric, ε_m and ε_d, to the permittivity along the x and y axes. Equation 1.5 relates both of the material permittivity to the permittivity of the metamaterial along the z axis.

$$\varepsilon_{xx} = \varepsilon_{yy} = \rho\varepsilon_m + (1-\rho)\varepsilon_d \tag{1.4}$$

$$\varepsilon_{zz} = \left(\rho\frac{1}{\varepsilon_m} + (1-\rho)\frac{1}{\varepsilon_d}\right)^{-1} \tag{1.5}$$

Density, ρ, does not equal the physical density of the metal or dielectric but the amount of metal in the structure based on area [9]. Essentially, ρ is the percent volume of metal in the metamaterial. Density is calculated by the total thickness of all metal layers divided by the overall thickness of the hyperbolic metamaterial. If the total number of metal and dielectric layers are equal, density can be calculated using a two-layer metal and dielectric pair.

The effective medium theory equations change for nanorods. A different equation is used for the permittivity in the x and y direction of nanorods, while Equation 1.4 is used for the permittivity in the z direction in Equation 1.7 [9]. Density, ρ, is calculated by the total area of the cross-sections of the rods on the x-y plane, area of a circle, divided by the area of the hyperbolic metamaterial. If using only a specified area of the metamaterial, density is calculated using only the nanorods confined within that area.

$$\varepsilon_{xx} = \varepsilon_{yy} = \frac{[(1+\rho)\varepsilon_m + (1-\rho)\varepsilon_d]\cdot\varepsilon_d}{(1-\rho)\varepsilon_m + (1+\rho)\varepsilon_d} \tag{1.6}$$

$$\varepsilon_{zz} = \rho\varepsilon_m + (1-\rho)\varepsilon_d \tag{1.7}$$

1.3 Refractive Index Near Zero

Another point of interest lies around the origin of the coordinate system, in Figure 1.1, where permittivity and permeability are equal to zero. This property of near zero index metamaterials becomes difficult to achieve in the optical regime since permeability close to zero, as mentioned in section 1.1.

The simple refractive index equation in Equation 1.8 shows that it can be possible to create a refractive index near zero metamaterial if only permittivity is equal or close to zero with normal values for permeability [13].

$$n = \sqrt{\varepsilon \cdot \mu} \tag{1.8}$$

Hyperbolic metamaterials with refractive index near zero observe a collimation effect [14]. Waves travelling through the metamaterial will have a Poynting vector close to perpendicular to the surface from a flat thin film structure.

The Poynting vector is in the direction of the group velocity. Information can be obtained for a near zero refractive index metamaterial using the equation for phase velocity and group velocity [15][16][17][18].

From Equation 1.9, the phase velocity will increase faster than the speed of light. The group velocity will decrease with a refractive index near zero [9][13]. Impedance, η, will also increase as permittivity near zero, in Equation 1.11, affecting the Poynting vector.

$$v_p = \frac{\omega}{k} = \frac{c}{n} = \frac{c}{\sqrt{\varepsilon \cdot \mu}} \tag{1.9}$$

$$v_g = \frac{c}{n - \omega \cdot \frac{dn}{d\omega}} \tag{1.10}$$

$$\eta = \sqrt{\frac{\mu}{\varepsilon}} \tag{1.11}$$

The Poynting vector will fall within a cone where light will tend to travel. For refractive index near zero metamaterials, the direction will be close to an angle of 0°. [14][19]. The angle of the resonance cone, θ_{RC}, can be calculated using Equation 1.12.

$$\theta_{RC} = tan^{-1}\sqrt{\left|\frac{Re(\varepsilon_{xx})}{Re(\varepsilon_{zz})}\right|} \tag{1.12}$$

1.4 Anisotropy in Hyperbolic Metamaterials

The anisotropic properties and the resulting hyperbolic dispersion have an effect on transverse electric, TE, polarized light. [16] TE polarization is called s-polarization and transverse magnetic, TM, polarization is called p-polarization. The separation of these two polarizations can produce a birefringent effect where light is split into two rays.

P-polarized light will follow regular Snell's Law where permittivity in the x and y axis is used to calculate the refractive index. This ray is called the ordinary ray. S-polarized light will take a different path influenced by the permittivity of light in the z direction as well as the x and y direction. The result is a new refractive index along the path of the extraordinary ray.

These properties can occur naturally in uniaxial crystals having a single optic axis [16]. When applied to hyperbolic metamaterials, artificially created uniaxial crystals, the optic axis will fall along the z axis [20]. This property can simplify uniaxial crystal equations that require separate angles between the ray and optic axis and between the optic axis and the z axis.

1.5 Near Zero Design

Multiple methods of achieving a refractive index near zero were found while researching hyperbolic metamaterials. There are works that connect the dispersion relation, Equation 1.1, to

the wave vector. [20][21][22] A different form of Equation 1.13 is used where the dispersion relation is in terms of angle of the wave vector.

$$\frac{cos^2\theta}{\varepsilon_{zz}} + \frac{sin^2\theta}{\varepsilon_{xx}} = \frac{1}{n^2} \tag{1.13}$$

The effective medium theory can be substituted into Equation 1.13 to relate the refractive index to the material parameters and dimensions [21]. Other research includes the incident angle in the dispersion relation as part of the K_x component from equation 1.1 [22]. The dispersion plot can also be manipulated to form a Dirac cone shaped dispersion plot where two equal cones meet at the origin forming two intersecting lines on the x-z plane [13]. These are all different methods employed in research towards near zero refractive index.

Equation 1.13 is rearranged to have the refractive index in the numerator, shown in Equation 1.14. Where the resulting refractive index affects the extraordinary wave vector, the refractive index is now $n_e(\theta)$ in relation to the angle of the wave vector.

$$n = \frac{\sqrt{\varepsilon_{xx} \cdot \varepsilon_{zz}}}{\sqrt{\varepsilon_{xx} \cdot sin^2(\theta) + \varepsilon_{zz} \cdot cos^2(\theta)}} \tag{1.14}$$

Equation 1.8 is followed to convert permittivity to refractive index to get Equation 1.15. The refractive index along the z axis becomes the extraordinary refractive index, n_e, and the refractive index along the x axis becomes the ordinary refractive index, n_o.

$$n_e(\theta) = \frac{n_o \cdot n_e}{\sqrt{n_o^2 \cdot sin^2(\theta) + n_e^2 \cdot cos^2(\theta)}} \tag{1.15}$$

1.6 Applications of Hyperbolic Metamaterials

A field where metamaterials can be employed is in solar cell design. For best performance, solar panels are directed towards the sun. Fixed solar panels would benefit from

metamaterials that redirect more light into the solar panels. Even rotating solar panels would see an improvement. Metamaterials designed to allow the absorption of more light would increase absorption efficiency in solar panels [23].

The transmittance of evanescent wave in hyperbolic metamaterials can help in microscopy. Objects smaller than half the wavelength of light appear indistinct. A metamaterial lens would overcome this diffraction limit increasing the resolution of smaller objects [24].

Hyperbolic metamaterials can also be used as waveguides. Light is channeled from a source on a chip to a nanofiber. There would be no reflected light in the metamaterial due to the propagation of evanescent waves at the interface. Advanced in like these would help in the field of quantum information processing and quantum communications [25].

1.7 Motivation

The properties leading to the permittivity tensors of hyperbolic metamaterials are known and widely accepted. Developing a straightforward method to connect previous work with meaningful results would assist in the design of hyperbolic metamaterials throughout the optical regime. The objective of this research is to design and fabricate a near zero refractive index metamaterial in the visible spectrum. Materials are chosen to help shift zero index metamaterials from the ultraviolet spectrum towards the shorter wavelengths of light. The methods discussed could help spread the applications of hyperbolic metamaterials alongside the development of better materials for optical applications.

CHAPTER II

THEORY

Equations for describing the behavior of light in anisotropic crystals are known and applied to existing uniaxial crystals. The same equations are proposed for designing hyperbolic metamaterials where the direction of the wave and the refractive index can be directly calculated.

2.1 Axes of Permittivity

The ε parameter of permittivity is expressed in anisotropic crystals as the permittivity in the x, y and z axes. As modeled in Figure 2.1, the x axis and y axis now share permittivity expressed as epsilon parallel, $\varepsilon_{\parallel}$, and the permittivity along the z axis, orthogonal to the plane of interface, has permittivity expressed as epsilon perpendicular, $\varepsilon_{\perp}$.

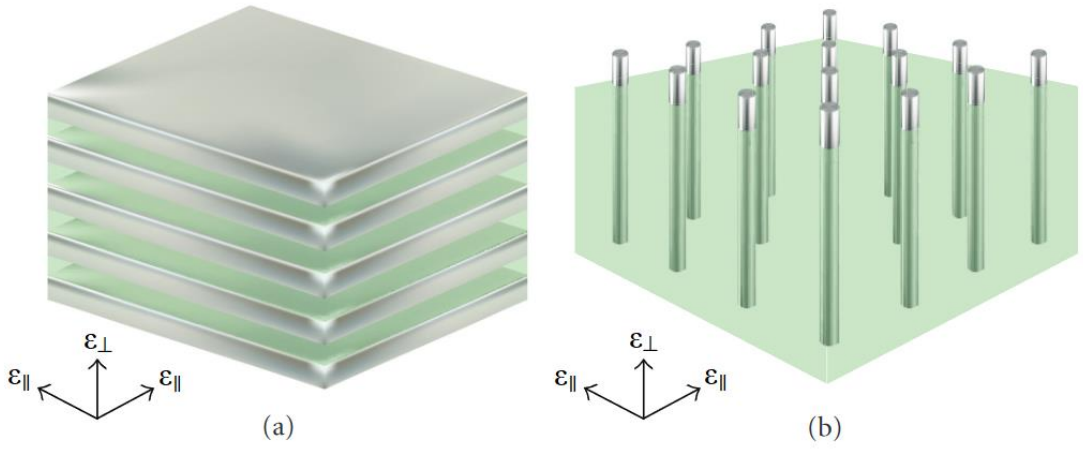

Figure 2.1: Epsilon Parallel and Perpendicular in Multilayer Thin Films and Nanorods [11]

2.2 Fill Fraction

An anisotropic multilayer structure is altered through the ratio between the thicknesses of the metal and dielectric layers. A multilayer structure will have a specified thickness for each materials The thickness of all metal layers over the combined thickness of both metal and dielectric layers is the density, ρ, of metal in the metamaterial expressed as a ratio and not the actual density of the material.

$$\rho = \frac{H_{m,total}}{H_{m,total} + H_{d,total}} \tag{2.1}$$

The combined thickness of metal layers is denoted as $H_{m,\,total}$ and $H_{d,total}$ for metal and dielectric layers. Since this value is a ratio, the volume of silver within the metamaterial is expressed as the Fill Fraction of the structure, *FF* in Equation 2.2 [26].

$$FF = \rho \times 100 \tag{2.2}$$

2.3 Effective Medium Theory

The electric field intensity, *E*, and the electric flux density, *D*, are related through Equation 2.3 where effective permittivity, ε, represents the permittivity of the structure [26].

$$D = \varepsilon E \tag{2.3}$$

2.3.1 Epsilon Parallel

For boundary conditions between dielectric and conductor layers, the tangential components of the electric field of metal and dielectric, $E_{m,\parallel}$ and $E_{d,\parallel}$, are equal to each other and are set equal to the tangential componential of the entire multilayer structure, $E_{\parallel}$.

$$E_{\parallel} = E_{m,\parallel} = E_{d,\parallel} \tag{2.4}$$

The relationship of the tangential electric flux density of the structure, $D_{\|}$, and of metal and dielectric layer contributions, $D_{m,\|}$ and $D_{d,\|}$, are written in Equation 2.3 form as the Equations 2.5a-b, where ε_m and ε_d are the dielectric constants of metal and dielectric materials.

$$D_{\|} = \varepsilon_{\|} E_{\|} \tag{2.5a}$$

$$D_{m,\|} = \varepsilon_m E_{m,\|} \tag{2.5b}$$

$$D_{d,\|} = \varepsilon_d E_{d,\|} \tag{2.5c}$$

Where the Fill Fraction is expressed as density of metal, ρ, the tangential electric flux density, $D_{\|}$, is composed of the electric flux density contributions of metal and dielectric in proportion to their density. The density of the dielectric is one minus the density of metal.

$$D_{\|} = \rho D_{m,\|} + (1-\rho) D_{d,\|} \tag{2.6}$$

Equations 2.5a-c are substituted into Equation 2.6 to obtain the electric field, $E_{\|}$, from its metal and dielectric contributions.

$$\varepsilon_{\|} E_{\|} = \rho \varepsilon_m E_{m,\|} + (1-\rho) \varepsilon_d E_{d,\|} \tag{2.7}$$

Since the electric field intensities are all equal, shown in Equation 2.4, then Equation 2.7 reduces further to epsilon parallel and the permittivity of metal and dielectric.

$$\epsilon_{\|} = \rho \varepsilon_m + (1-\rho) \varepsilon_d \tag{2.8}$$

Equation 2.1 for density is substituted into Equation 2.8 to obtain Equation 2.9a and reduced to Equation 2.9d. This relates thicknesses to permittivity of metal and dielectric layers.

$$\varepsilon_{\|} = \left(\frac{H_m}{H_m + H_d}\right) \varepsilon_m + \left[1 - \left(\frac{H_m}{H_m + H_d}\right)\right] \varepsilon_d \tag{2.9a}$$

$$\varepsilon_{\|} = \left(\frac{H_m}{H_m + H_d}\right) \varepsilon_m + \left[\left(\frac{H_m + H_d}{H_m + H_d}\right) - \left(\frac{H_m}{H_m + H_d}\right)\right] \varepsilon_d \tag{2.9b}$$

$$\varepsilon_{\|} = \left(\frac{H_m}{H_m + H_d}\right) \varepsilon_m + \left(\frac{H_d}{H_m + H_d}\right) \varepsilon_d \tag{2.9c}$$

$$\varepsilon_{\parallel} = \frac{H_m \varepsilon_d + H_d \varepsilon_d}{H_m + H_d} \tag{2.9d}$$

2.3.2 Epsilon Perpendicular

From the boundary conditions of a dielectric and conductor, the normal component of the electric flux density should be continuous. The normal flux density of the entire structure, $D_{\perp}$, is set equal to the normal flux density of metal and dielectric layers, $D_{m,\perp}$ and $D_{d,\perp}$.

$$D_{\perp} = D_{m,\perp} = D_{d,\perp} \tag{2.10}$$

The relationship between the electric field intensity is written, similar to Equation 2.6 using the metal density of the multilayer structure proportionally.

$$E_{\perp} = \rho E_{m,\perp} + (1-\rho) E_{d,\perp} \tag{2.11}$$

Equations 2.5a-c solved for electric field are substituted into Equation 2.11 to include the permittivity of the structure and materials. Since all the electric flux densities in Equation 2.12 are equal, as shown in Equation 2.10, they cancel out to get Equation 2.13.

$$\frac{D_{\perp}}{\varepsilon_{\perp}} = \rho \frac{D_{m,\perp}}{\varepsilon_m} + (1-\rho) \frac{D_{d,\perp}}{\varepsilon_d} \tag{2.12}$$

$$\frac{1}{\varepsilon_{\perp}} = \rho \frac{1}{\varepsilon_m} + (1-\rho) \frac{1}{\varepsilon_d} \tag{2.13}$$

Similar to epsilon parallel in Equation 2.9a, Equation 2.1 is substituted into Equation 2.13 to get an equation relating thicknesses to permittivity in Equation 2.14d.

$$\frac{1}{\varepsilon_{\perp}} = \left(\frac{H_m}{H_m + H_d}\right) \frac{1}{\varepsilon_m} + \left[1 - \left(\frac{H_m}{H_m + H_d}\right)\right] \frac{1}{\varepsilon_d} \tag{2.14a}$$

$$\frac{1}{\varepsilon_{\perp}} = \left(\frac{H_m}{H_m + H_d}\right) \frac{1}{\varepsilon_m} + \left[\left(\frac{H_m + H_d}{H_m + H_d}\right) - \left(\frac{H_m}{H_m + H_d}\right)\right] \frac{1}{\varepsilon_d} \tag{2.14b}$$

$$\frac{1}{\varepsilon_{\perp}} = \left(\frac{H_m}{H_m + H_d}\right)\frac{1}{\varepsilon_m} + \left(\frac{H_d}{H_m + H_d}\right)\frac{1}{\varepsilon_d} \tag{2.14c}$$

$$\frac{1}{\varepsilon_{\perp}} = \frac{\frac{H_m}{\varepsilon_m} + \frac{H_d}{\varepsilon_d}}{H_m + H_d} \tag{2.14d}$$

The two resulting equations for epsilon parallel and epsilon perpendicular, Equations 2.9d and 2.14d, are known as the effective medium theory of the metamaterial.

$$\varepsilon_{\parallel} = \frac{H_m\varepsilon_m + H_d\varepsilon_d}{H_m + H_d} \tag{2.15}$$

$$\varepsilon_{\perp} = \frac{H_m + H_d}{\frac{H_m}{\varepsilon_m} + \frac{H_d}{\varepsilon_d}} \tag{2.16}$$

Equations 2.15 and 2.16 form the basis for designing a hyperbolic metamaterial from alternating layers of metal and dielectric. By combining the permittivity of metal and dielectric layers, the structure will have anisotropic permittivity dependent on direction.

2.4 Tensors

Uniaxial crystals are anisotropic media with an equal value of refractive index on its two lateral axes. If described by their permittivity and permeability, they can be written as Equations 2.17 and 2.18 [27]. In an ideal application of light, permeability is assumed to be unity, in which case only Equation 2.17 is considered [9].

$$\bar{\varepsilon} = \begin{bmatrix} \varepsilon_{\parallel} & & \\ & \varepsilon_{\parallel} & \\ & & \varepsilon_{\perp} \end{bmatrix} \tag{2.17}$$

$$\bar{\mu} = \begin{bmatrix} \mu_{\parallel} & & \\ & \mu_{\parallel} & \\ & & \mu_{\perp} \end{bmatrix} \tag{2.18}$$

2.5 Ordinary Refractive Index

Uniaxial crystals are birefringent and split an approaching wave into two separate waves at the interface. The ordinary wave behaves like a regular wave transmitted into nonbirefringent material. Ordinary refractive index, n_o, is used to solve the ordinary wave vector angle [16].

$$n_o = \sqrt{\varepsilon_o \cdot \mu_o} \tag{2.19}$$

Epsilon parallel, $\varepsilon_\parallel$, and mu parallel, $\mu_\parallel$, can be used instead of epsilon ordinary, ε_o, and mu ordinary, μ_o, as seen in Equation 2.20 to avoid confusion. The terms ordinary and extraordinary will be used strictly for the refractive indices in Snell's Law instead of the refractive indices of the tangential and normal components.

$$n_o = \sqrt{\varepsilon_\parallel \cdot \mu_\parallel} = n_\parallel \tag{2.20}$$

Snell's Law is then written as Equation 2.21 [15][16].

$$n_i \cdot \sin(\theta_i) = n_o \cdot sin\left(\theta_{t,o}\right) \tag{2.21}$$

2.6 Extraordinary Refractive Index

Unlike Equation 2.21, the extraordinary refractive index, n_e in Equation 2.22, written similar to equation 2.20, cannot be used for the extraordinary refractive index in Snell's Law since the refractive index changes with direction within the metamaterial.

$$n_e \neq \sqrt{\varepsilon_e \cdot \mu_e} \tag{2.22}$$

The right side of Equation 2.2 is only the refractive index in the normal component refractive index perpendicular, $n_\perp$, written with epsilon perpendicular, $\varepsilon_\perp$, and mu perpendicular, $\mu_\perp$, written as Equation 2.3

$$n_e \neq \sqrt{\varepsilon_\perp \cdot \mu_\perp} = n_\perp \tag{2.23}$$

Equation 2.24 is the refractive index for uniaxial crystals, $n_e(\theta)$, relative to the angle between the extraordinary wave vector and the optic axis, θ, as expressed generally.

$$n_e(\theta) = \frac{n_o \cdot n_e}{\sqrt{n_o^2 \cdot sin^2(\theta) + n_e^2 \cdot cos^2(\theta)}} \tag{2.24}$$

Equation 2.25, used with Equations 2.20 and 2.23, is preferred instead.

$$n_{t,e}(\theta) = \frac{n_{\parallel} \cdot n_{\perp}}{\sqrt{n_{\parallel}^2 \cdot sin^2(\theta) + n_{\perp}^2 \cdot cos^2(\theta)}} \tag{2.25}$$

Snell's Law is then written as Equation 2.26, where $\theta_{t,e}$ is the angle between the extraordinary wave vector and the Z axis [15][16].

$$n_i \cdot \sin(\theta_i) = n_{t,e}(\theta) \cdot sin\left(\theta_{t,e}\right) \tag{2.26}$$

Equation 2.25 is substituted into Equation 2.26 resulting in two different wave vector angles, θ and $\theta_{t,e}$.

$$n_i \cdot \sin(\theta_i) = \left(\frac{n_{\parallel} \cdot n_{\perp}}{\sqrt{n_{\parallel}^2 \cdot sin^2(\theta) + n_{\perp}^2 \cdot cos^2(\theta)}} \right) \cdot sin\left(\theta_{t,e}\right) \tag{2.27}$$

The manner in which the multilayer structure is fabricated will result in the metamaterial having the optic axis parallel to the Z axis. This means that θ in Equation 2.27 can be written as $\theta_{t,e}$, the extraordinary wave vector angle for this special case.

$$n_i \cdot \sin(\theta_i) = \left(\frac{n_{\parallel} \cdot n_{\perp}}{\sqrt{n_{\parallel}^2 \cdot sin^2\left(\theta_{t,e}\right) + n_{\perp}^2 \cdot cos^2\left(\theta_{t,e}\right)}} \right) \cdot sin\left(\theta_{t,e}\right) \tag{2.28}$$

Equation 2.28 is rearranged to have a single wave vector angle by solving for $\theta_{t,e}$. [16]

$$\tan\left(\theta_{t,e}\right) = \frac{n_{\perp}}{n_{\parallel}} \cdot \frac{n_i \sin\left(\theta_i\right)}{\sqrt{n_{\perp}^2 - n_i^2 sin^2(\theta_i)}} \tag{2.29}$$

Equation 2.29 can be further rearranged to look similar to Snell's Law. The refractive index of the medium of the approaching wave, n_i, is retained throughout the derivation of Equation 2.30. Derivations for Equation 2.30 are performed in the Appendix.

$$n_i \cdot \sin(\theta_i) = \sqrt{n_{\parallel}^2 + \left(\frac{n_{\perp}^2 - n_{\parallel}^2}{n_{\perp}^2}\right) \cdot n_i^2 \cdot sin^2(\theta_i)} \cdot sin\left(\theta_{t,e}\right) \tag{2.30}$$

The radical before $\sin(\theta_{t,e})$ can now be interpreted as Equation 2.31, the refractive index of uniaxial crystals having an optical axis perpendicular to the surface in terms of the refractive index of the initial medium and the angle of incident wave.

$$n_{t,e}(\theta_i) = \sqrt{n_{\parallel}^2 + \left(\frac{n_{\perp}^2 - n_{\parallel}^2}{n_{e\perp}^2}\right) \cdot n_i^2 \cdot sin^2(\theta_i)} \tag{2.31}$$

2.7 Poynting Vector

The wave vector does not always correspond to the direction of propagation of energy, or the Poynting vector. This is especially true for anisotropic crystals. Assuming that the optic axis is on the z axis which is perpendicular to the surface, Equation 2.32 is used to determine the Poynting vector, θ_S [16].

$$tan(\theta_S) = \left(\frac{n_o^2}{n_e^2}\right) \cdot tan(\theta_t) \tag{2.32}$$

Following the same substitutions with Equations 2.20 and 2.23 from previous equations, Equation 2.33 shows the Poynting vector, $\theta_{S,e}$, in terms of refractive index parallel and perpendicular.

$$tan\left(\theta_{S,e}\right) = \left(\frac{n_{\parallel}^2}{n_{\perp}^2}\right) \cdot tan\left(\theta_{t,e}\right) \tag{2.33}$$

2.8 Group Refractive Index

While the Poynting vector equation contains terms similar to a refractive index, the actual refractive index observed in the direction of the Poynting vector is unknown. Since the design is a near zero refractive index metamaterial, the refractive index in the direction of the Poynting vector is expected to be close to zero.

An equation similar to the refractive index of the wave vector, Equations 2.25, was found in order to solve for the Poynting vector's refractive index [28]. This equation represents group refractive index, n_g, where the refractive index equals the speed of light, c, divided by the group velocity, v_g.

$$n_g = \frac{c}{v_g} = \sqrt{n_e^2 \cdot sin^2\theta_S + n_o^2 \cdot cos^2\theta_S} \tag{2.33}$$

Using the previous set of equations, the goal is to model the direction of light throughout the visible spectrum to identify the parameters and Fill Fraction that will produce a metamaterial with near zero refractive index. The following step is in finding materials that can produce epsilon parallel and perpendicular models with patterns that produce hyperbolic metamaterials.

CHAPTER III

DESIGN

Preliminary modeling of metals and dielectrics, their properties and their effects on the hyperbolic metamaterial were performed prior to the final design. The difficulty in creating metamaterials for the visible spectrum lies in the availability of metals and other plasmonic materials for optical application. Materials were chosen based on their real and imaginary parts of permittivity which determined how effective they would work as metamaterial components.

3.1 Materials

3.1.1 Metal

Metals are plasmonic materials since they have negative permittivity in the visible spectrum. Other nonmetallic plasmonic materials exhibit similar qualities including reflection of light. Specific applications require low imaginary values of permittivity [29].

Silver and gold become attractive metals for this reason. Real permittivity of silver drops at longer wavelengths. This limits several applications to the shorter wavelengths of violet and into blue light. The permittivity of gold drops less severely than silver with increasing wavelengths, but experiences higher dielectric loss. Copper is only slightly worse than gold in dielectric loss. While common in optical applications, aluminum’s extremely negative dielectric function cannot be matched by dielectric with high permittivity. The oxidation of copper and aluminum becomes an issue for long term use of metamaterials.

Nitrides have been proposed as substitutes to metals since they display similar metallic properties in visible light. [30]. Metamaterials using nitrides could be created in the longer wavelengths within red and yellow light, but permittivity can vary with deposition recipe. Silver is chosen based on its low imaginary loss and extensive research into its refractive index.

3.1.2 Dielectric

To counteract the low permittivity of silver, a dielectric with very high permittivity, and refractive index, is required. Titanium Dioxide is a common dielectric used for high permittivity applications. Naturally occurring TiO2 has three polymorphs: rutile, anatase and brookite crystal [31]. Rutile has higher refractive index than the other two, but the refractive indices of all three crystals drop after deposition.

Perovskites with high permittivity appeared frequently while searching for dielectrics. The perovskites that stood out for their high refractive indices were Strontium Titanate (STO, SrTiO3O), Barium Titanate (BTO, BaTiO3), Barium Strontium Titanate (BST, $Ba_xSr_{1-x}TiO3$), Lead Zirconate Titanate (PZT), and Bismuth Titanate. Lead Zirconate Titanate (BIT). The variable *x* in BST represents the ratio of BTO to STO.

PZT had very high permittivity but was avoided due to its lead content. The other perovskites were evaluated based on their transmittance. BIT showed very low transmittance around 35% to 40% [32][33]. STO had similar transmittance to BIT [34]. BTO appeared to have better transmittance with 50% at around 400 nm [35]. BST, which is a combination of BTO and STO, showed better results between 60% to 80% transmittance [36][37][38].

Different ratios of BTO to STO within BST can be requested from target manufacturers. Based on research conducted in observing the refractive index of different BST compositions,

the best results appeared to have more STO than BTO [39]. The BST target used in fabricating the metamaterial is 30% BST and 70% STO. The manufacturer provided the data in Table 3.1 confirming the composition of BST.

Table 3.1: $Ba_{0.3}Sr_{0.7}TiO3$ Composition

Composition	wt.%	mol.%
BaTiO3	35.27	30
SrTiO3	64.73	70

3.1.3 Substrate

The targets are deposited on glass substrates which must withstand temperatures at around 800° C. The available options for glass that can withstand high annealing temperatures were narrowed down to fused silica and BK7. Fused silica was chosen over BK7 since it has a slightly lower refractive index. Double side polished fused silica wafers were ordered with dimensions of 50.8 mm wide and 500 μm thick.

3.2 Dielectric Functions

3.2.1 Dielectric Functions of Silver

Dielectric functions are plots of dielectric constants or permittivity across a range of wavelengths. The Lorentz-Drude model is used to obtain a dielectric function of silver where ω^2_p represents the plasma frequency of silver [40][41]. Metals above their plasma frequency begin to exhibit dielectric properties.

$$\varepsilon_{L-D}(\omega) = 1 - \frac{f_0 \cdot \omega_{p,0}^2}{\omega^2 + i \cdot \Gamma_0 \cdot \omega} + \sum_{j=1}^{j_{max}} \frac{f_j \cdot \omega_{p,j}^2}{\omega_j^2 - \omega^2 - i \cdot \Gamma_j \cdot \omega} \tag{3.1}$$

For a range of frequencies, ω, multiple oscillations are described with resonant frequencies, ω_j, strengths, f_j, and damping factors, Γj. The values for silver used in the Lorentz-

Drude model in Equation 3.1 are shown in Table 3.2. The first set of values are used in the initial oscillation and the last five are used in the last term of the equation.

Table 3.2: Lorentz-Drude Values [41]

	f_j	ω^2_p [rad/s]	ω_j[rad/s]	Γj [rad/s]
j = 0	0.845	13.69×10^{15}	0.0000	0.07292×10^{15}
j = 1	0.065	13.69×10^{15}	1.240×10^{15}	5.904×10^{15}
j = 2	0.124	13.69×10^{15}	6.808×10^{15}	0.6867×10^{15}
j = 3	0.011	13.69×10^{15}	12.44×10^{15}	0.09875×10^{15}
j = 4	0.840	13.69×10^{15}	13.80×10^{15}	1.392×10^{15}
j = 5	5.646	13.69×10^{15}	30.83×10^{15}	3.675×10^{15}

Figure 3.1 graphs the resulting dielectric function of silver for the entire visible spectrum. The negative permittivity can be seen dropping as the wavelength increases. In other words, light observes a different dielectric constant of silver for different wavelengths. For this reason, lists and tables of dielectric constants cannot be used unless they are for a wide range of wavelengths for a single element or material.

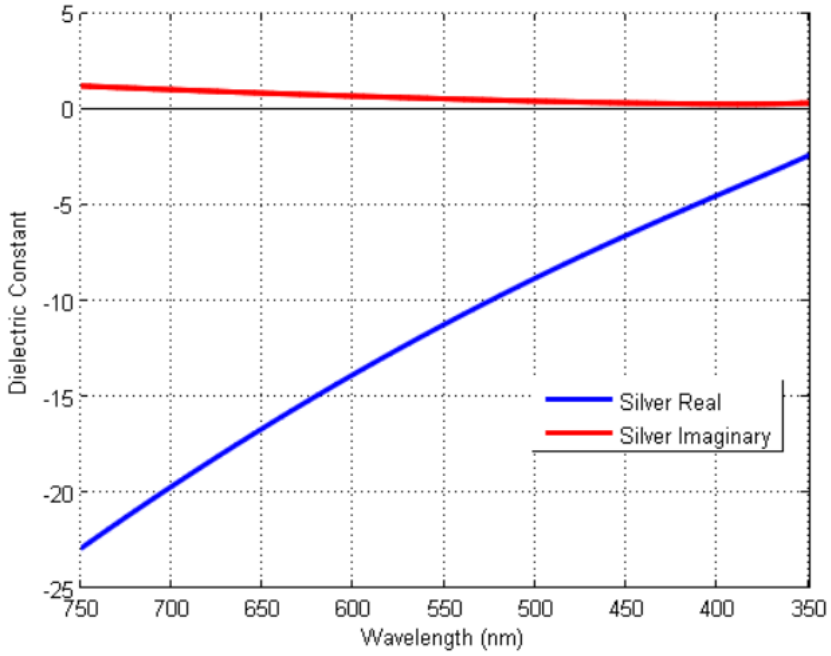

Figure 3.1: Dielectric Function of Silver

3.2.2 Dielectric Function of Barium Strontium Titanate

For the dielectric function of BST, the Sellmeier model was used with values for BTO. The dielectric function of BST was similar to BTO. Table 3.3 shows the values for the coefficients used in Equation 3.1 [42]. BST was modeled using the extraordinary refractive index values.

$$n^2(\lambda) = 1 + \sum_i \frac{B_i \lambda^2}{\lambda^2 - C_i} \tag{3.1}$$

Table 3.3: BST Values [42]

	B	C
n_o	4.187	0.223
n_e	4.064	0.211

Figure 3.2 shows the dielectric function used for BST. Since Equation 3.1 does not produce imaginary permittivity, very low values are substituted as part to form the imaginary part of the dielectric function.

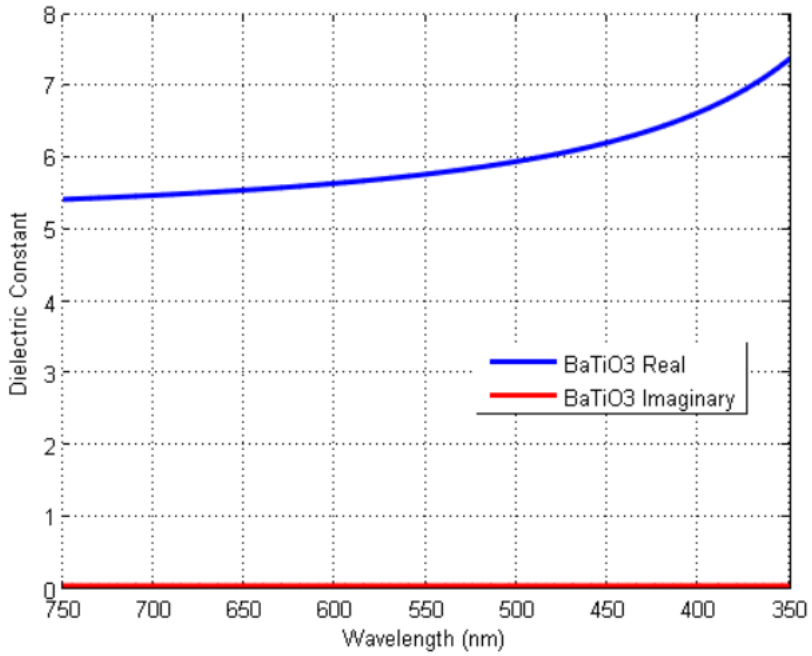

Figure 3.2: Dielectric Function of BST

3.3 Multiple Stack Design

During preliminary modeling of the structure, better results were achieved for multilayers with metal as both the top and bottom layers. This concept can be considered as inserting dielectric layers into metal. These structures are identified as MDM or MDMDM, where M represents a metal layer and D represents a dielectric layer [43].

These 3-layer and 5-layer structures, called stacks, can be fabricated on top of each other so the metamaterial is composed of multiple stacks. As an example, a 3-stack multilayer of MDM will can be considered as an MDM-MDM-MDM structure shown in Figure 3.3.

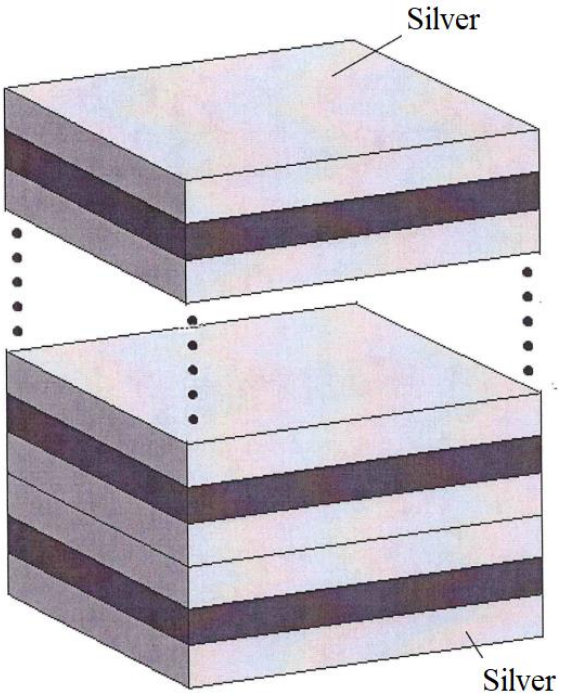

Figure 3.3: Three 3-layer Stacks [44]

Between stacks, there are two consecutive layers of metal deposited as a thicker layer. A single deposition of silver can replace two separate depositions in this case. Since the entire metamaterial is fabricated with similar repeating stacks, the Fill Fraction for the entire metamaterial is equal to the Fill Fraction for a single stack.

3.4 Range of Wavelengths

Based on preliminary modeling, the metamaterial can be designed for a limited range of wavelengths. As mentioned earlier, the negative dielectric function of silver drops very low. A dielectric with similar but positive dielectric function is needed to extend the range. Figure 3.4 shows the regions of hyperbolic metamaterials [8]. The range of Type I metamaterials will be within blue and violet light where $\varepsilon_{//}$ is positive and $\varepsilon_{\perp}$ is negative. Within this region, the dark blue lines show promise as values for near zero refractive index.

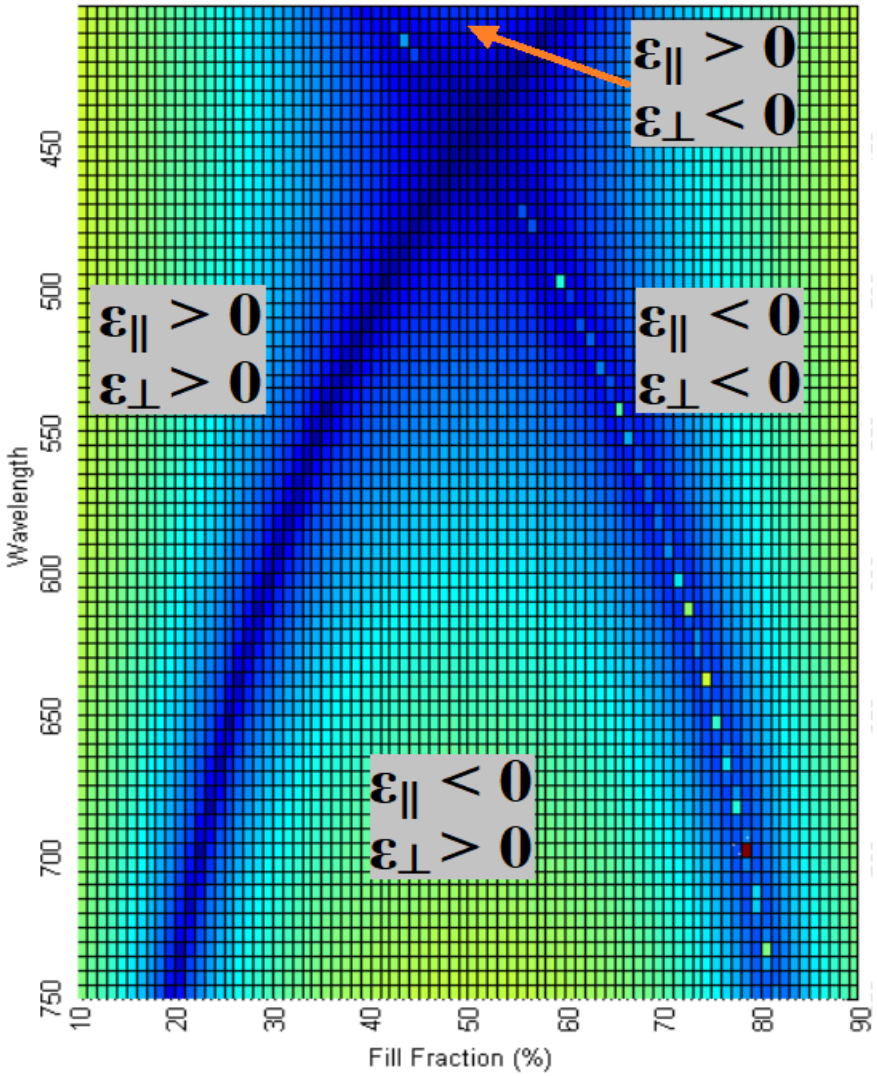

Figure 3.4: Hyperbolic Metamaterial Regions

The Type I region ranges from the edge of ultraviolet light into visible light at 400 nm to the point where the Type II region begins at 440 nm. A wavelength of 405 nm, violet light, was chosen as the operating wavelength for the design based on the availability of this laser, but the wavelength can be adjusted for different applications. Modeling and simulation will be based on the parameters of the chosen materials.

CHAPTER IV

MODELING AND SIMULATION

Before modeling of the hyperbolic metamaterial properties, the dielectric functions for Silver and BST (BTO) were written into the script. Arrays of epsilon parallel and perpendicular for wavelength versus Fill Fraction were created using Equations 2.15 and 2.16. The variables for the effective medium theory are thickness and epsillon. The thickness coincides with the Fill Fraction if thickness of the dielectric is constant and the thickness of silver changes. Since the permittivity of metal and dielectric change with wavelength, plots can be created for epsilon parallen and perpendicular for a single wavelength, as shown in Figure 4.1.

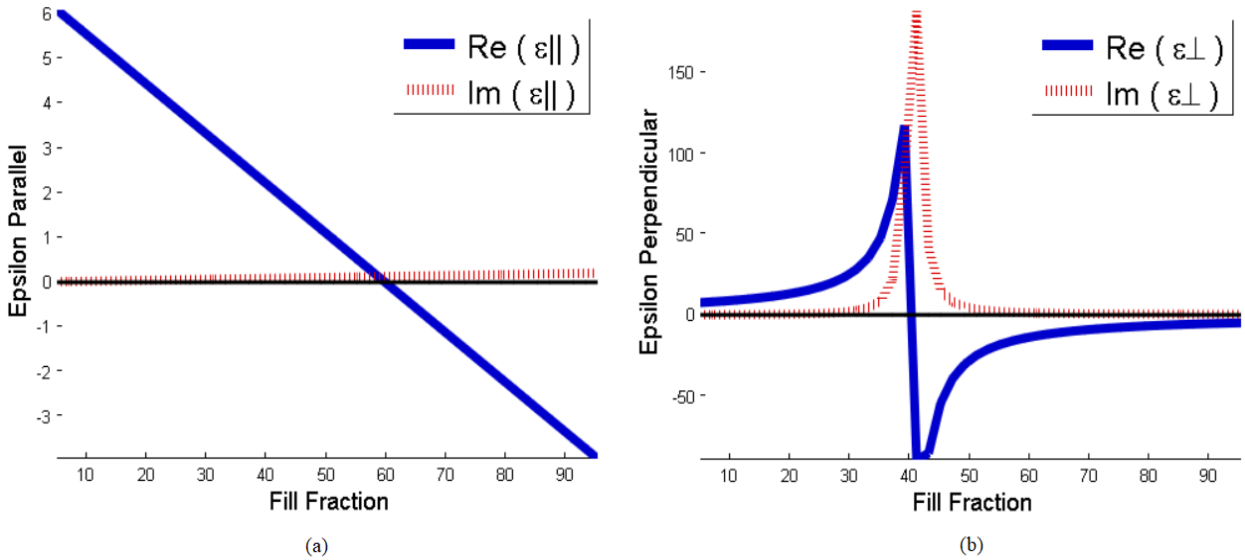

Figure 4.1: (a) Epsilon Parallel (b) Epsilon Perpendicular

Epsilon Parallel in Figure 4.1 (a) has a zero intersection at around 60%. The asymptote in Figure 4.1(b) is due to a pole in the epsilon parallel equation. Within this range of Fill Fraction, epsilon parallel is positive and epsilon perpendicular is negative. At 400 nm, this is the range of Fill Fraction for designing a hyperbolic metamaterial. The arrays calculated for epsilon parallel and perpendicular can be graphed across the range of the visible spectrum as shown in Figures 4.2 and 4.3.

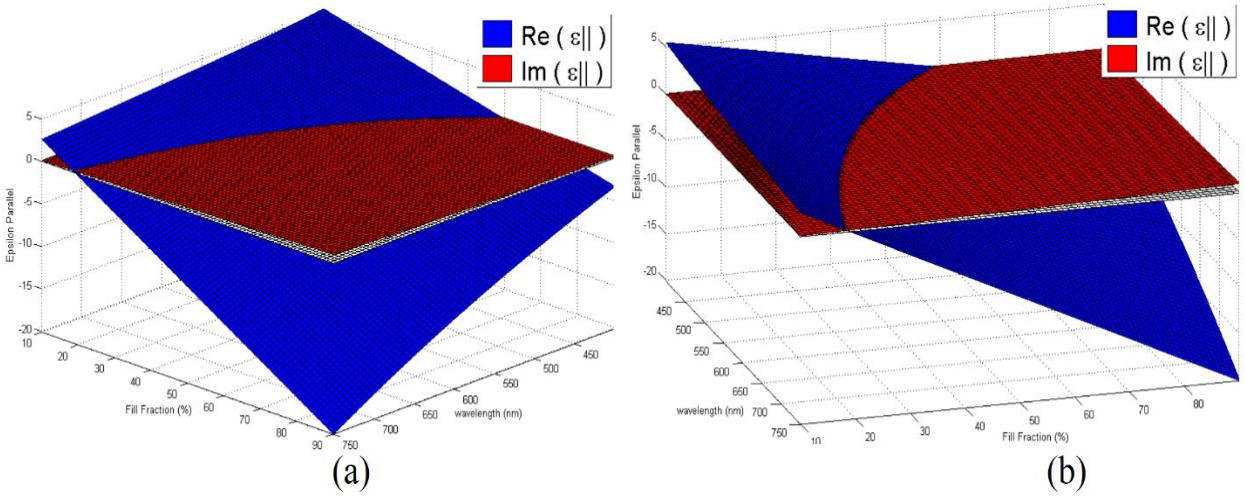

Figure 4.2: Epsilon Parallel Plots (a) and (b) at Different Angles

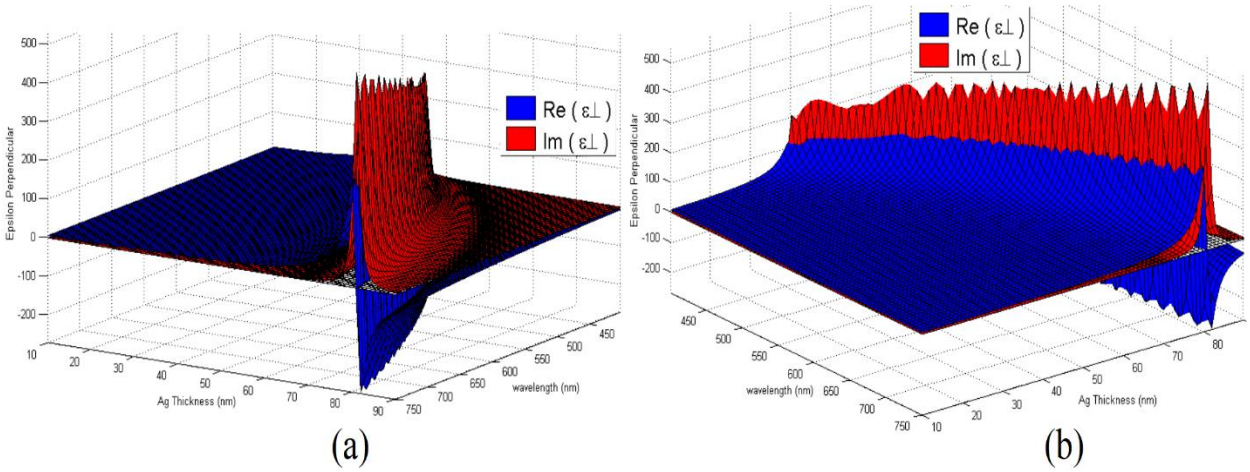

Figure 4.3: Epsilon Perpendicular Plots (a) and (b) at Different Angles

The dielectric functions of Silver and BST are graphed based on wavelength in Figure 4.4. Where the visible spectrum ranges between 700 nm and 400 nm, a Type I metamaterials would extended further into the visible spectrum between if the dielectric function of metal was equal in value and opposite in sign to the dielectric function of the dielectric material.

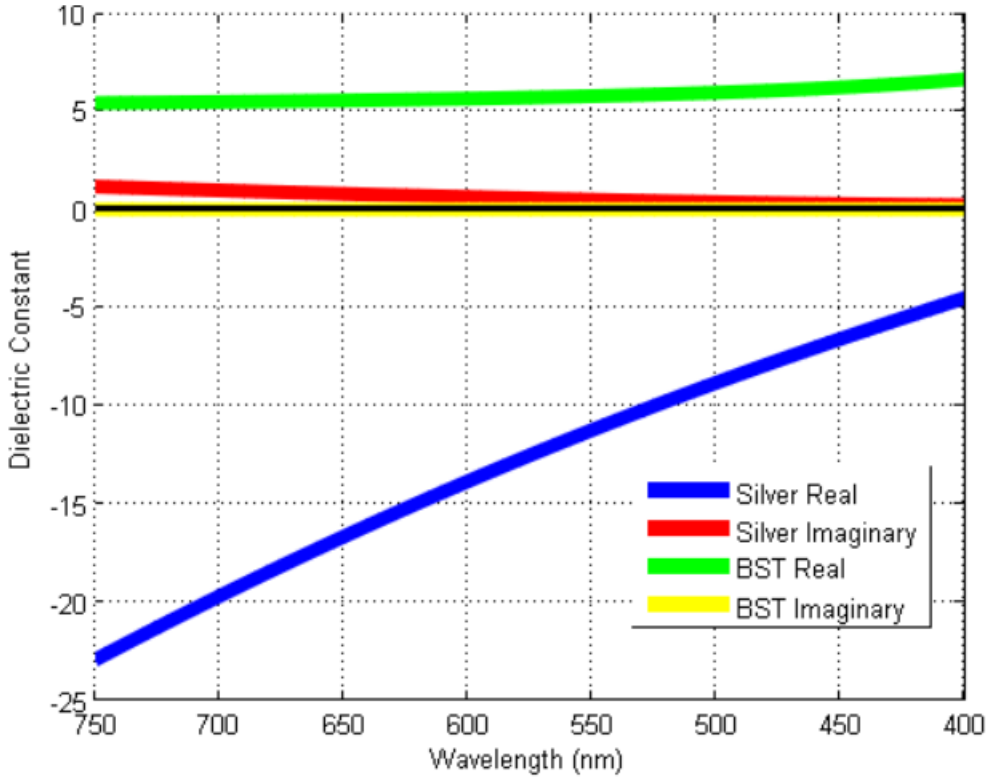

Figure 4.4: Material Parameters for Silver and BST

Figure 4.5 shows the graph for the angle of the ordinary wave. The region where angle goes to 90° indicates a complex angle. There is no propagation so the incident angle should reflect. The ordinary wave follows the regular equation for refractive index near zero.

The angles for the wave vector in Figure 4.6 appear similar to Figure 4.5. This graph shows the direction of the wave fronts. The angles do not go towards the negative so the wave fronts will always be positive.

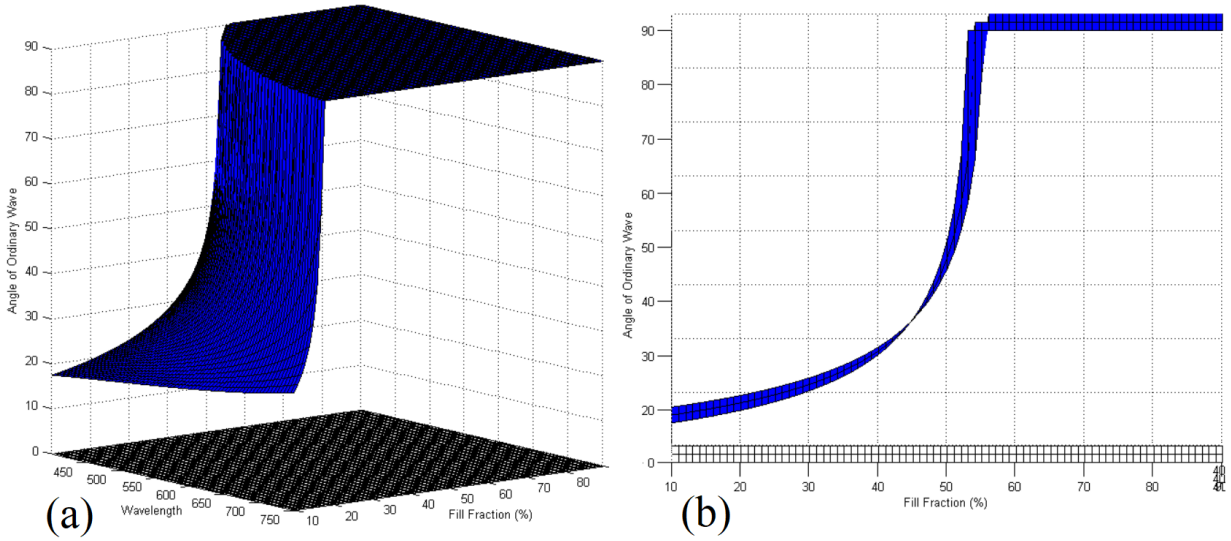

Figure 4.5: Angle of Ordinary Wave (a) Top View (b) 405 nm Cross Section

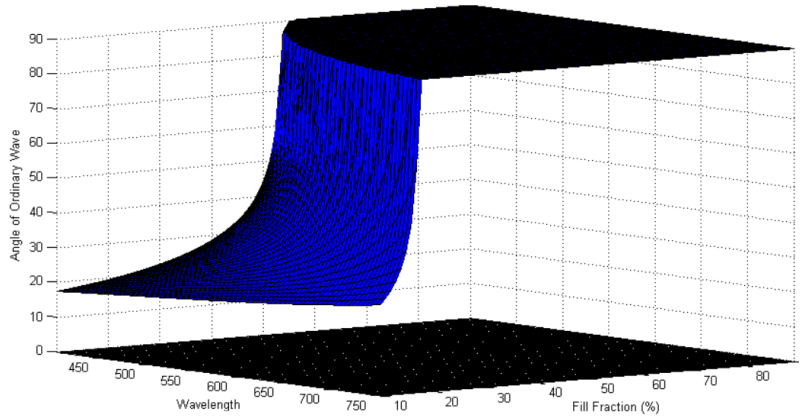

Figure 4.6: Angle of Wave Vector

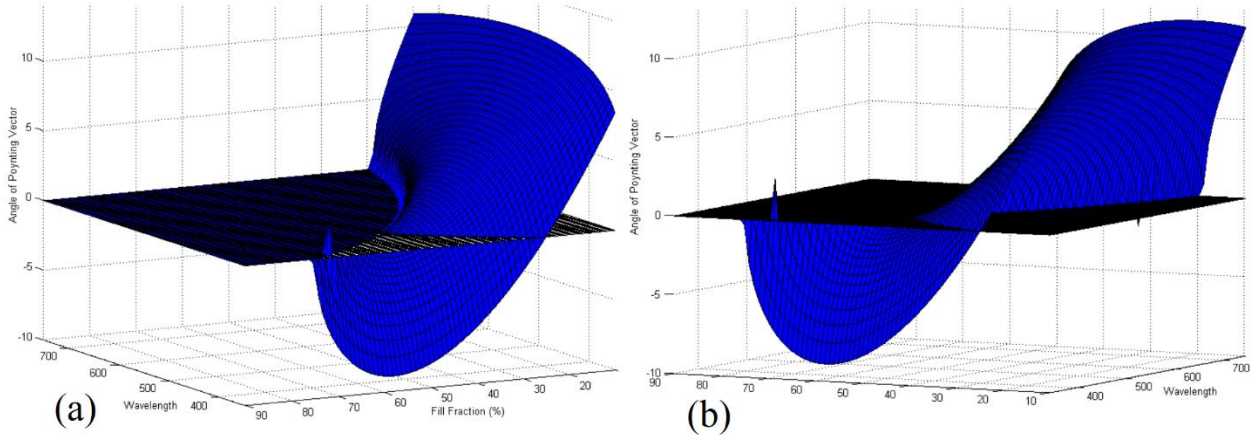

Figure 4.7: Angle of Poynting Vector (a) and (b)

The Poynting vector angles are shown in Figure 4.7. These angles indicate the direction of energy. The Type I hyperbolic metamaterial section has the angles becoming negative. Negative refractive index metamaterials are created where the graph intersects the x-y plane. Figures 4.8 and 4.9 illustrate these sections of the graph.

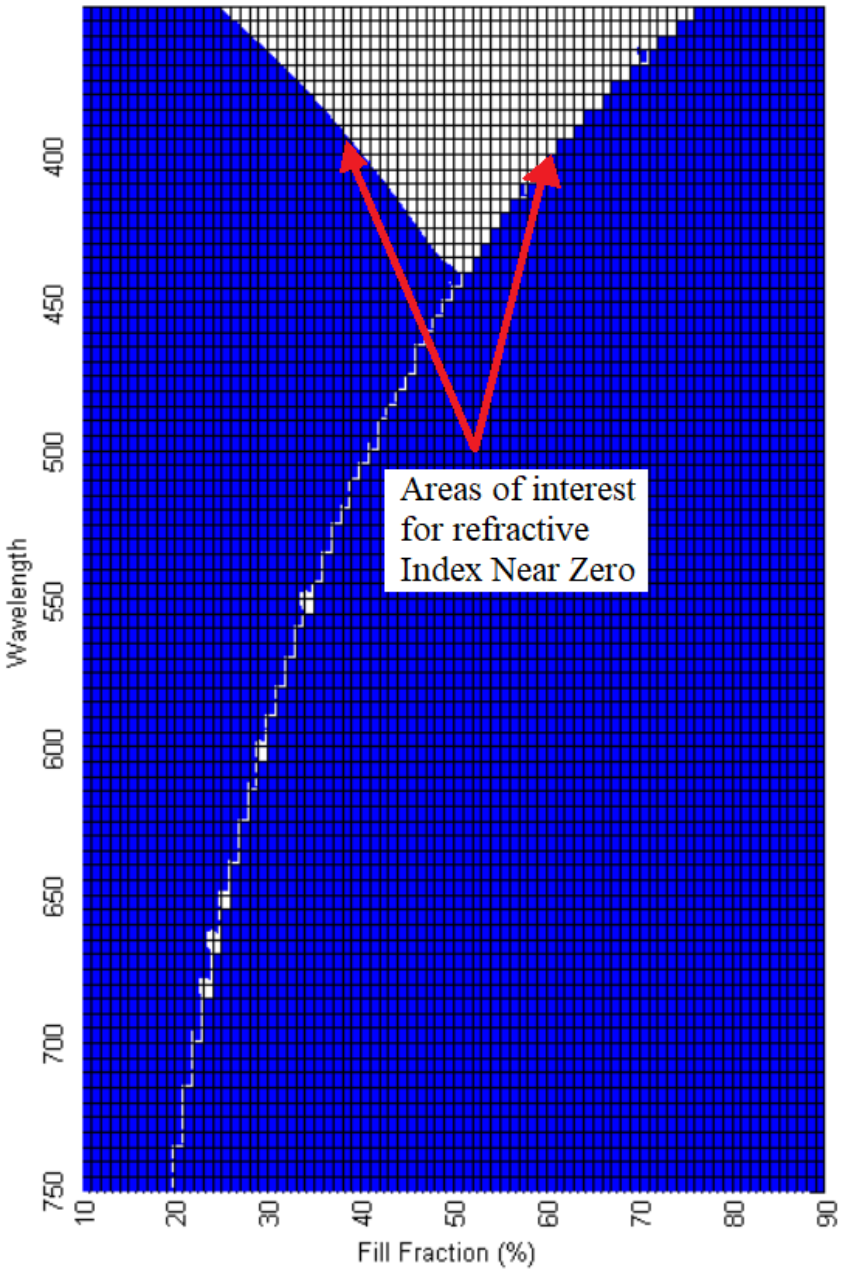

Figure 4.8: Angles of Poynting Vector on X-Y Plane View

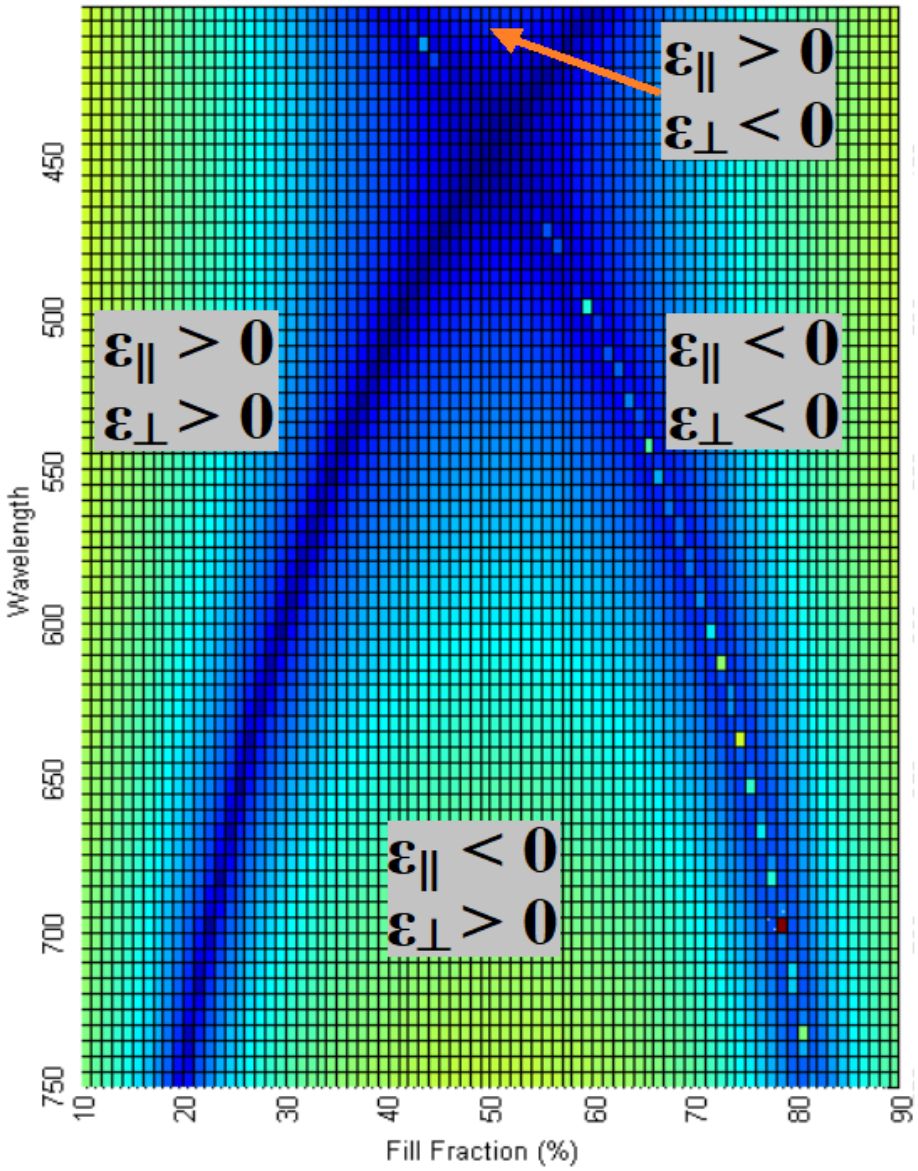

Figure 4.9: Hyperbolic Metamaterial Regions

The area in Figure 4.8 identified by the red arrows is where the graph intersects the x-y plane. The points along this intersection have potential in creating refractive index near zero metamaterials. The models do not show the refractive index observed by the Poynting vector travelling through the metamaterial [28].

Similar to equation 2.24 which calculates the refractive index that the wave vector observes, a refractive index term is needed for the Poynting vector. The group refractive index

was used to verify the results of the Poynting vector equation. [28]. This equation represents the group refractive index where the refractive index equals the speed of light divided by the group velocity. The Poynting vector should observe this refractive index rather than the indices previously obtained.

$$n_g = \frac{c}{v_g} = \sqrt{n_e^2 \cdot sin^2\theta_S + n_o^2 \cdot cos^2\theta_S} \tag{4.1}$$

The refractive index formed a strange shape in Figure 4.10. The plot gets close to zero at the Type I hyperbolic metamaterial region towards the right edge. Figure 4.11 shows the cross section at 400 nm where the real refractive index is in blue. The real refractive index gets close to zero around a Fill Fraction of 59%. Areas with complex angle, as found in the Type II region and effective metal region, were removed.

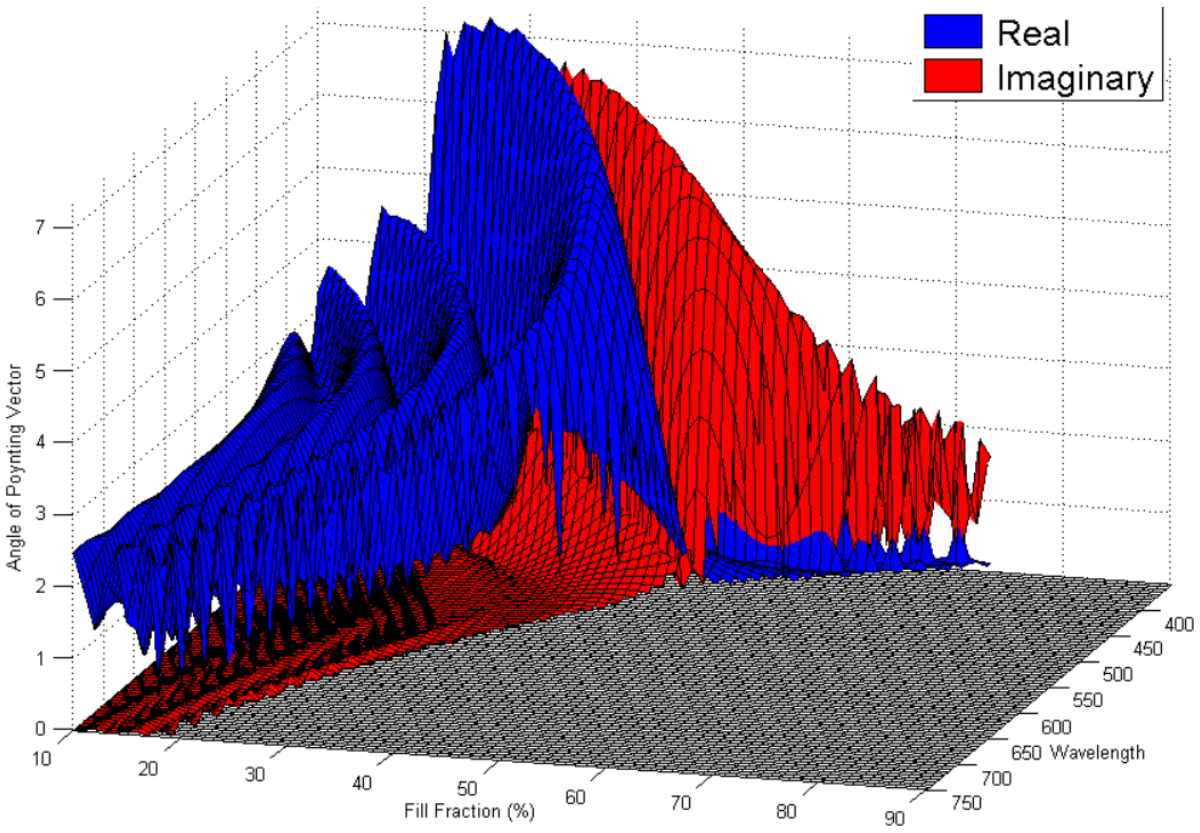

Figure 4.10: Group Refractive Index Graph

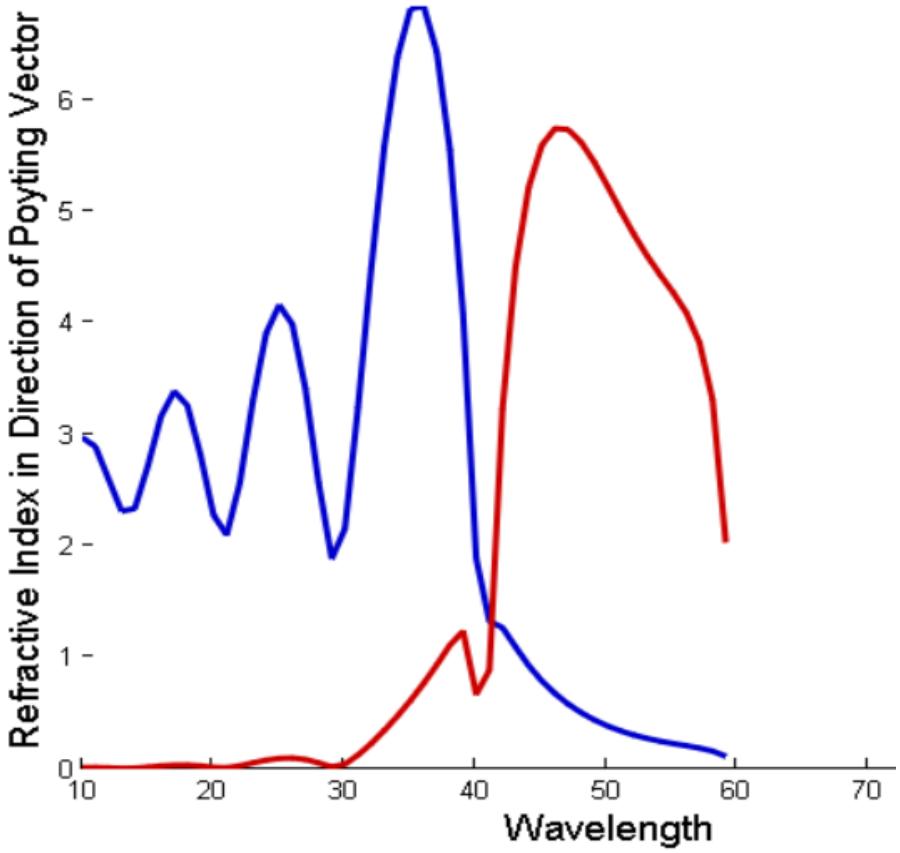

Figure 4.11: Group Refractive Index at 400 nm

The refractive index term to the right of the equal sign, in Equation 4.2, influences the curve of the Poynting vector angles in Figure 4.7.

$$tan(\theta_{S,e}) = \left(\frac{n_{\parallel}^2}{n_{\perp}^2}\right) \cdot tan(\theta_{t,e}) \tag{4.2}$$

Figure 4.12 shows the graph of this Poynting vector term. The result appears to highlight the four regions of hyperbolic metamaterials. Based on Figures 4.10 and 4.11, the zero intersections occurring between 400 nm and 440 nm and less than 50% Fill Fraction should have a high observed refractive index. While Equation 4.2 is very useful in determining Poynting vector, it should be noted that the area where epsilon perpendicular goes to positive infinity or negative infinity will calculate an angle of zero caused by the large number in the denominator.

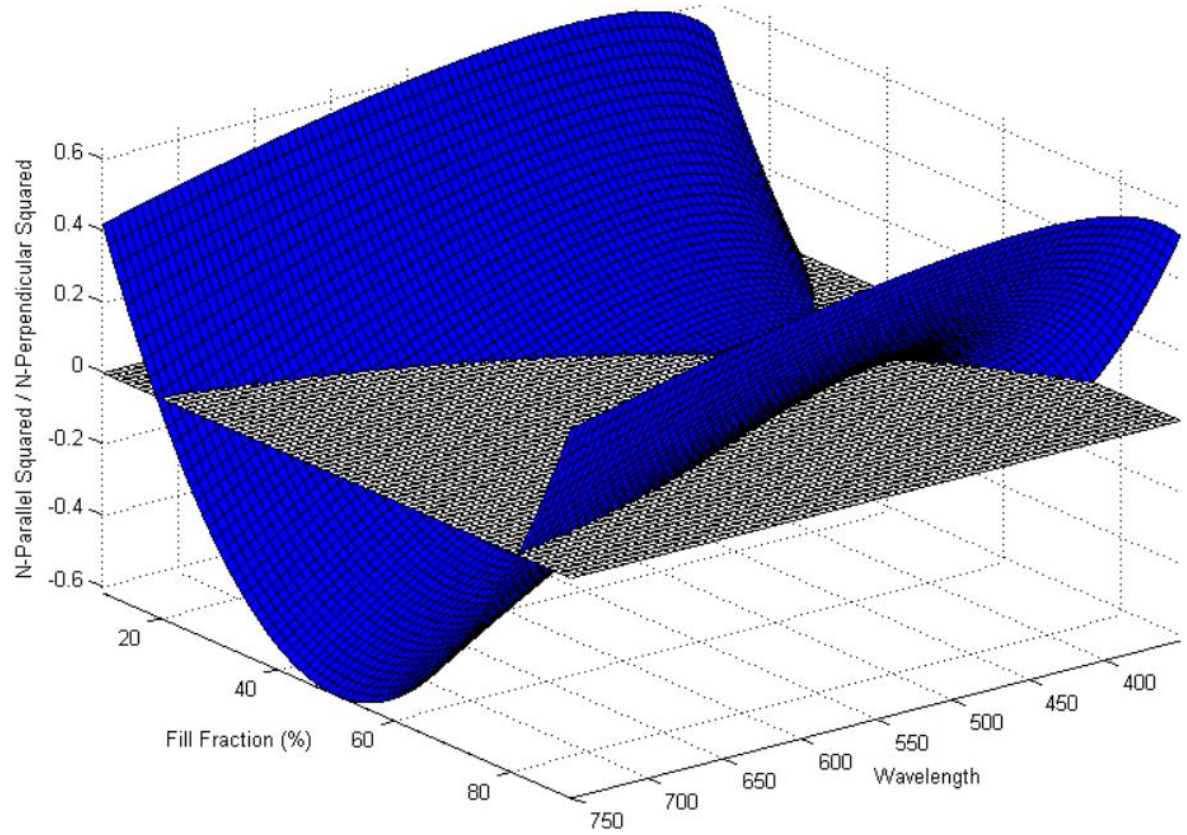

Figure 4.12: Index Parallel Squared Over Index Perpendicular Squared

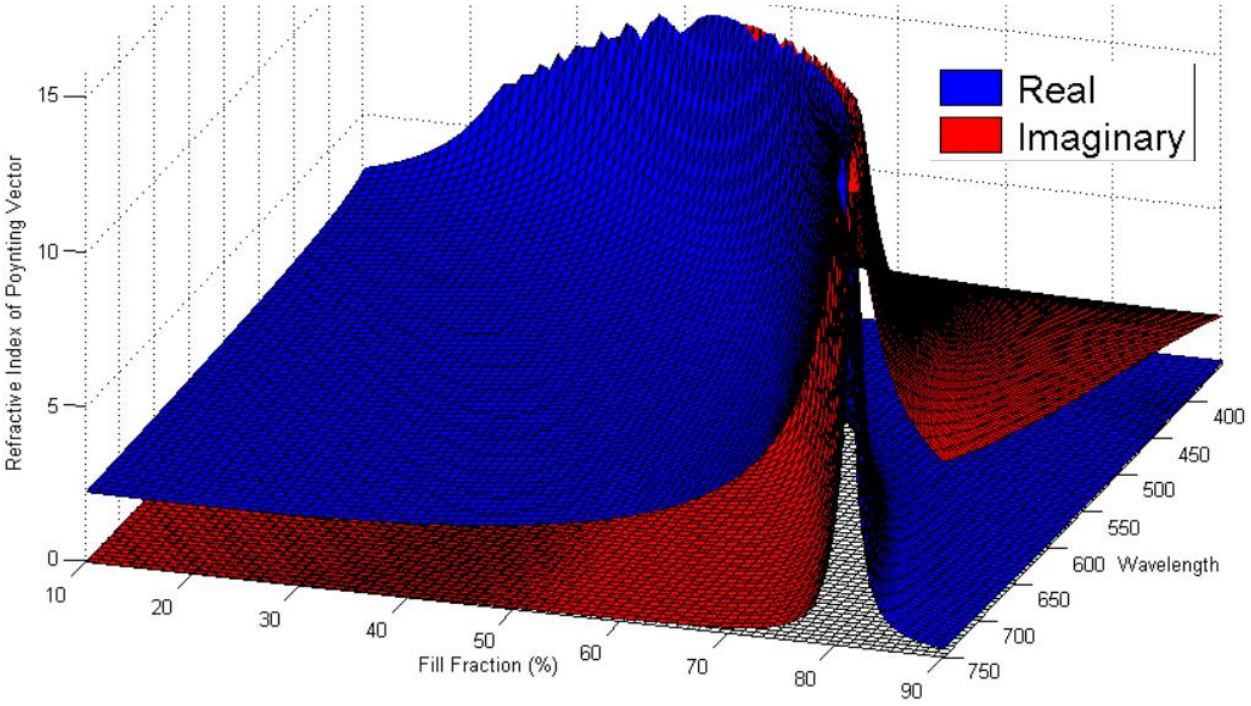

Figure 4.13: Group Refractive Index for Angle of 1°

By substituting a low angle into Equation 4.1 instead of the Poynting vectors, the refractive indices along the z axis can be found. Figure 4.13 characterizes the group refractive index for all wavelengths and Fill Fractions for a Poynting vector at 1° from the z axis. With high refractive index results near 40%, the locations with a pole in epsilon perpendicular appear less attractive than.

A closer inspection of the cross section at ranges 400 nm to 410, shown in Figure 4.14, indicate that better results for a refractive index near zero could be obtained for Fill Fractions above 50% to around 60%. The percentage will depend on the wavelength.

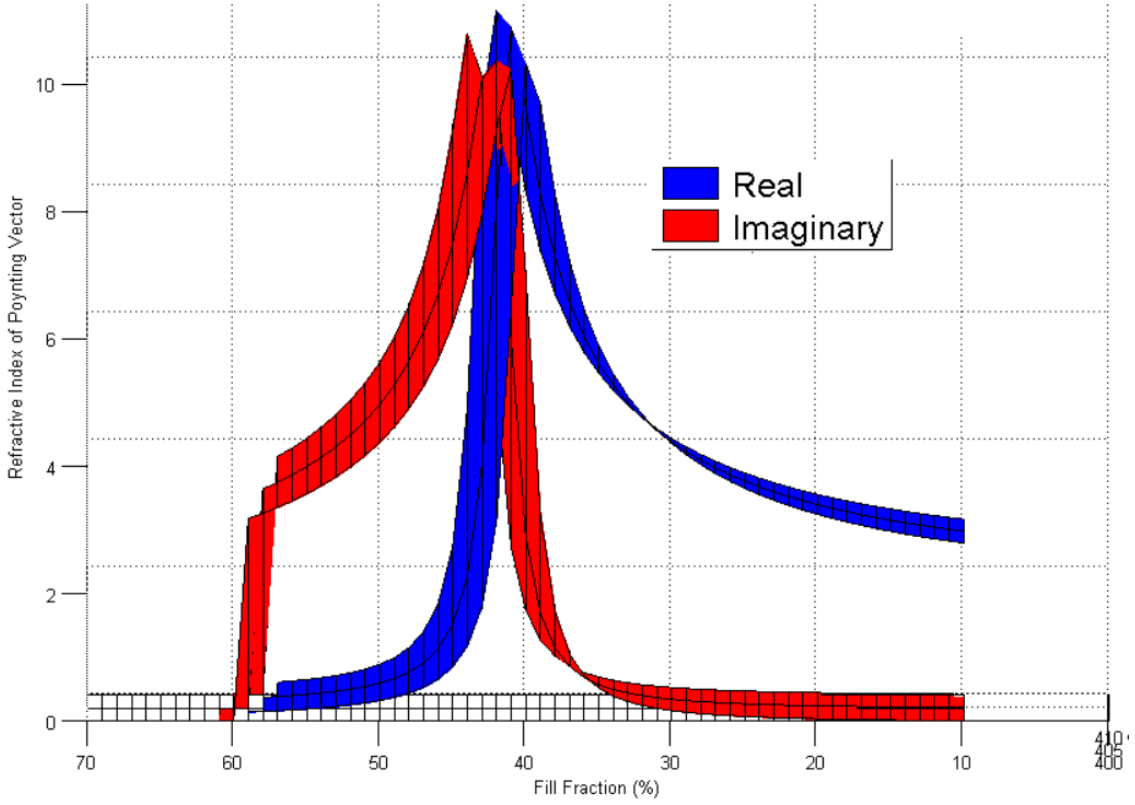

Figure 4.14: Group Refractive Index 400 nm to 410 nm

The results from modeling were simulated using CST. The design was based on results for 400 nm. The design is a three 5-layer stack for a total of 15 layers at 58% Fill Fraction.

Instead of setting the incident wave at an angle or rotating the source, the stack itself is rotated 30°, shown in Figure 4.15. The multilayer is approximately 2000 nm by 1000 nm. The values used for the dielectric function of BST are imported into CST. The materials library contained optical values for silver. Figure 4.15 shows the results at 450 nm. An s-polarized Gaussian source is used for the excitation which automatically sets the boundary conditions to open and requires a transient solver. Field monitors for the electric field, magnetic field and power flow were created for 350 nm, 400 nm and 450 nm.

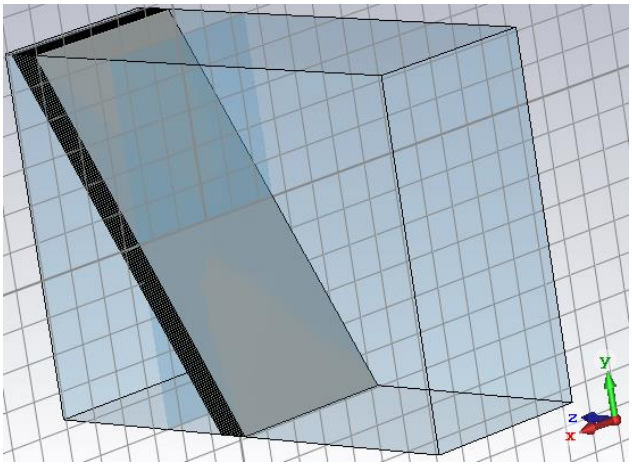

Figure 4.15: CST Model

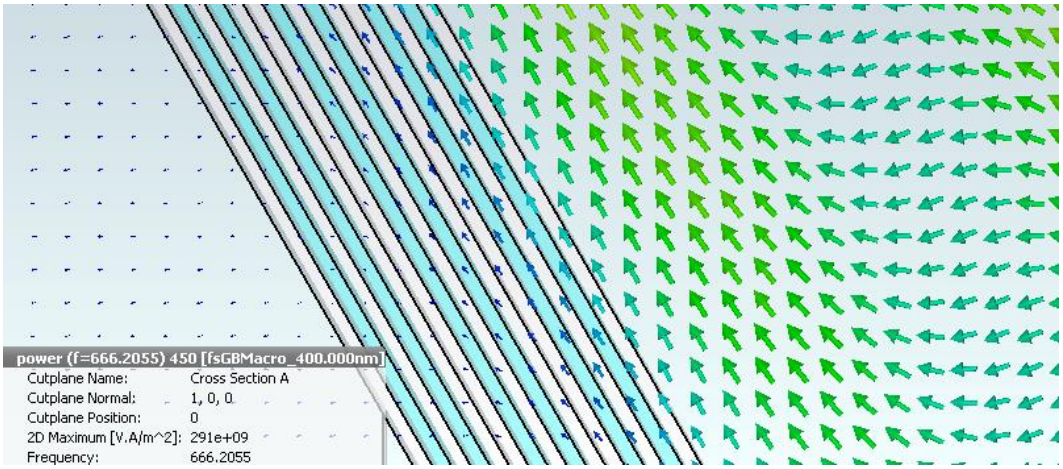

Figure 4.16: 68% FF at 450 nm

Figure 4.16 shows little propagation through the multilayer. The wave is being reflected as expect. In Figure 4.17 at 400 nm, the wave propagates through the metamaterial. The arrows showing the power flow are not pointing perpendicular to the service as predicted.

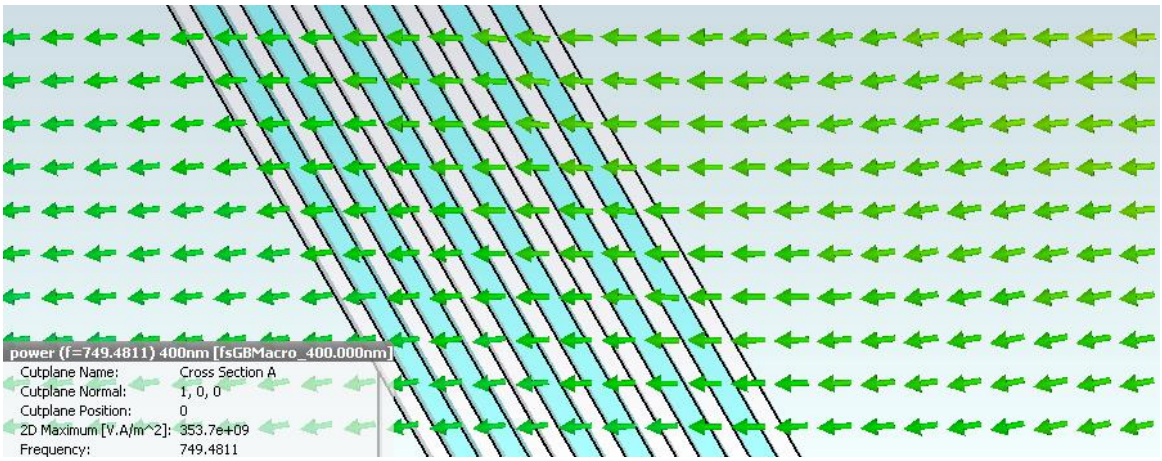

Figure 4.17: 68% FF at 400 nm

Figure 4.18 does show the arrows through the metamaterial pointing perpendicular creating a collimating effect. At 350 nm, this is in the ultraviolet spectrum.

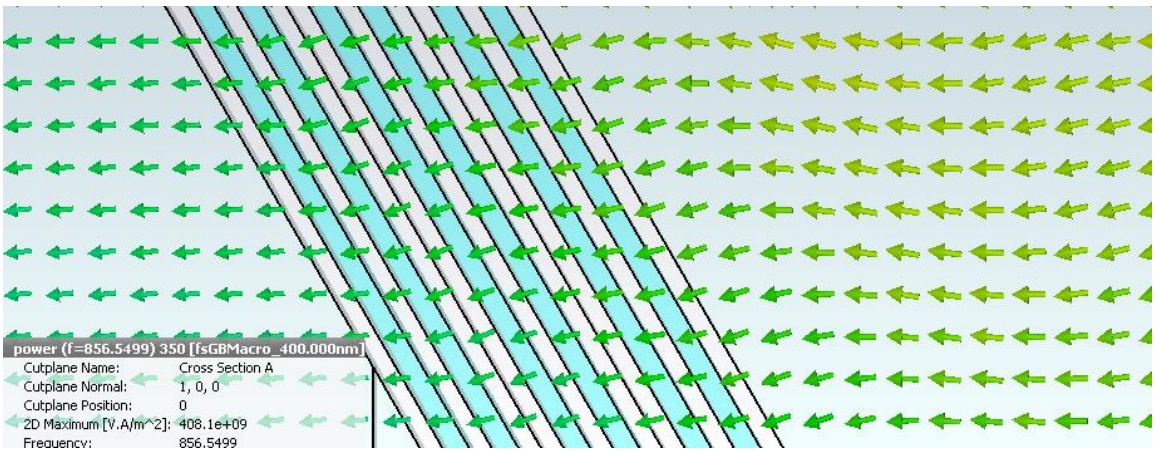

Figure 4.18: 56% FF at 350 nm

The CST simulations were more successful in the ultraviolet range at demonstrating near zero refractive index. Shifting the results into the visible range may require better modeling of materials at smaller thicknesses. The mesh could also affect the results of the CST simulations.

Besides observing the Poynting vector with power flow, interpretation of the results with the electric field and magnetic field monitors can be difficult with large waves for this application. A simulator specifically for optical applications might show different results using a specialized source. The simulation could be repeated in the future with different software to observe the wave vector and the Poynting vector.

CHAPTER V

FABRICATION

Before producing testable samples, there was the process of understanding the parameters for deposition, creating recipes and setting up measurements to obtain usable results. Samples were created between stretches of time due to availability of the magnetron sputtering system and measurement equipment. Where samples were created in the same group and measured to speed up the process measurement process.

The first five trials represent samples created before multilayers of silver and Barium Strontium Titanate (BST) were produced for x-ray photoelectron spectroscopy system (XPS) analysis. These trials were used to gain knowledge in operating the Magnetron Sputtering System and the parameters in RF and DC sputtering.

Samples from Group A through Group F produced more comprehensible results from the XPS from having access to technicians that could set up parameters and run measurements. MATLAB was used to process the data and demonstrate multiple layers and their thicknesses.

5.1 Initial Depositions

5.1.1 Copper on Glass Trials

Before the silver target was delivered, copper was used as a substitute for DC sputtering a metal target on glass slides while learning how to operate the magnetron. The first Copper trials used already existing layers for strike and clean were used before the copper deposition layers.

New copper layers were designed based on previously created layers to create thinner layers closer to 10 nm. All depositions showed visible thin films of copper. The 15 second deposition of copper was highly transparent while the 600 seconds (10 minutes) deposition had an opaque coating.

The samples were scanned by XPS. Figure 5.1 shows the existence of copper at a depth of 3.5 nm. The survey plot indicates evidence of other elements, but not as prominent as copper at 933 eV. Oxygen is highlighted since it would indicate the glass slide has been reached. The binding energy spike for oxygen is at 532 eV [45].

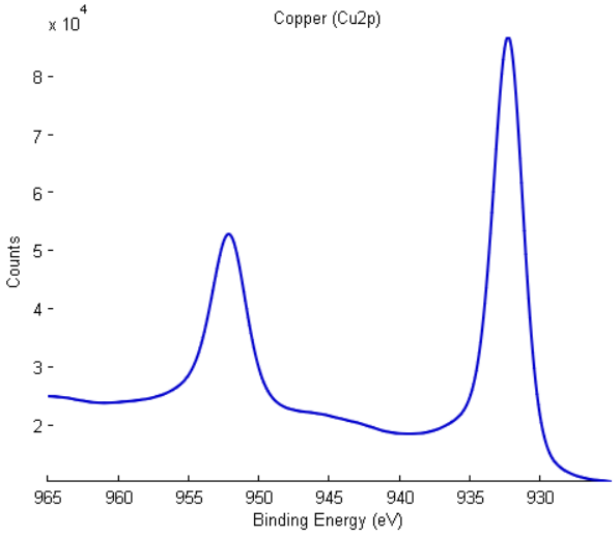

Figure 5.1: XPS Copper Results

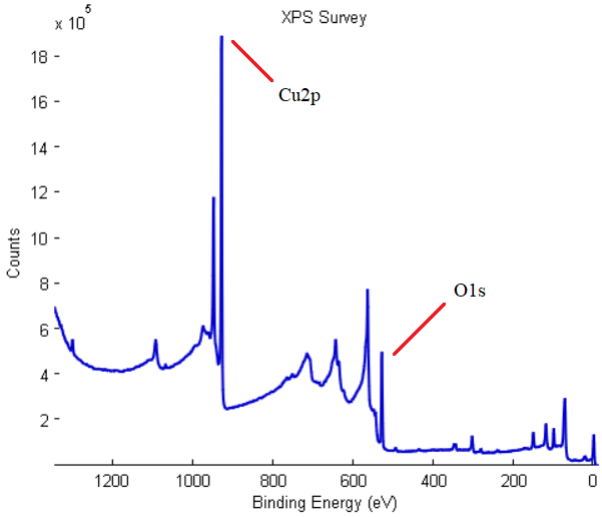

Figure:5.2: Survey (1 Minute)

Table 5.1: Copper Recipes

Cu on Glass			
Sample	Power (W)	Pressure (mTorr)	Time (Seconds)
1	50	3	15
2	50	3	60
3	50	3	120
4	50	3	600
*	Gas and flow rate undocumented		

The XPS produced 3D plots of the copper orbital counts versus the etch depth. The graphs, not displayed for copyright reasons, showed the test for copper was performed at 5 different etch depths with the lowest at 17.5 nm. Copper was still present at the lowest depth measured in the sample.

Figure 5.3 does not show presence of copper. The spike in the survey plot for copper is missing. The plot has an oxygen spike from the oxygen in silicon dioxide (SiO2) or silica. This is from misplacing the sample upside down on the sample holder causing the XPS to measure only the glass substrate.

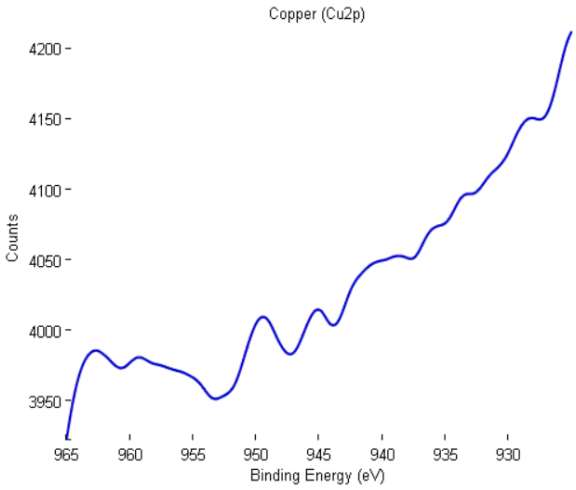

Figure 5.3: Copper Results (2 Minutes)

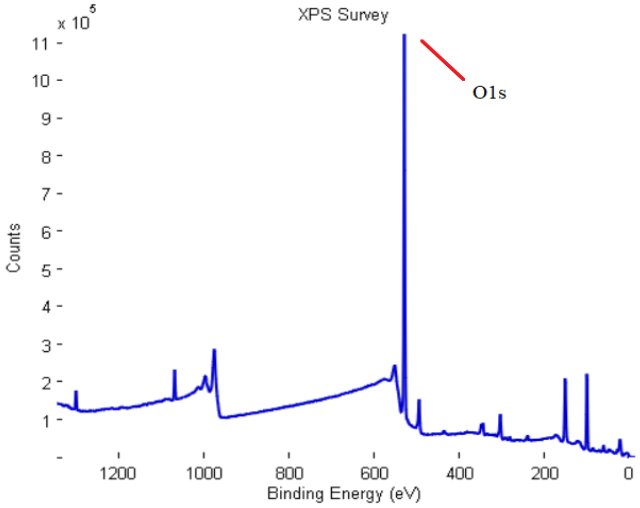

Figure 5.4: Survey (2 Minutes)

The XPS results in Figure 5.5 shows clear deposition at 3.5 nm. The maximum etch depth should have been adjusted in this case since the deposition would be thicker than the previous sample. The setback was in underestimating the deposition rate of copper for thicknesses close to 10 nm. The parameters for the XPS measurements were set based on estimations for the copper deposition rate, and the system was allowed to run overnight for two samples. Since running the XPS can last several hours, measurements are usually conducted when there are multiple samples in queue.

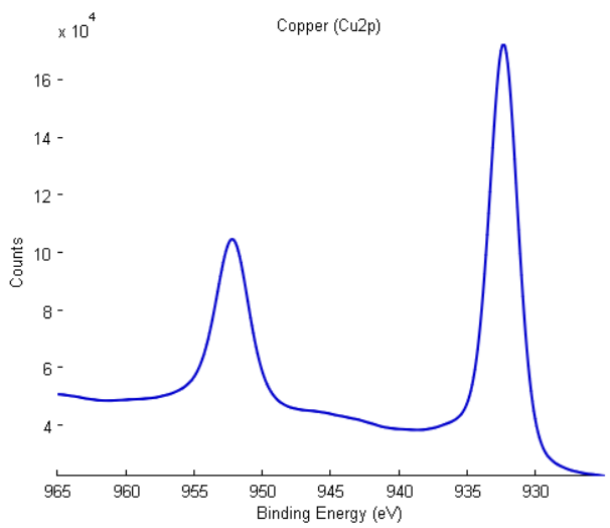

Figure 5.5: Copper Results (10 Minutes)

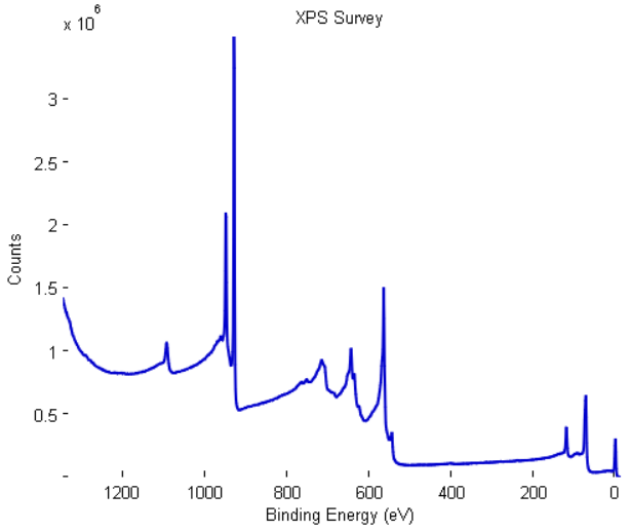

Figure 5.6: Survey (10 Minutes)

5.1.2 Copper and Gallium Oxide on Glass Trials

A second trial of copper on glass was performed with the addition of gallium oxide. Permission was requested to use the gallium oxide for training as a stand in for BST. The layers would be very thin, between 10 nm to 50 nm compared to layers deposited by other research students, 100 nm to 500 nm or larger.

The Gallium Oxide layer was created from an existing layer named GaO_9h_20mT_50W and renamed AO_GaO_15mT_30min_70W, as shown in Figure 5.7. The existing strike and clean layers for gallium oxide were also used. Copper was deposited at 50 W for 60 seconds while gallium oxide was deposited for 30 minutes. The table shows the recipes for the copper and gallium oxide layers.

Table 5.2: Copper and Gallium Oxide Recipe

Cu and GaO on Glass						
Sample	Cu (1st and 3rd Layers)			GaO (2nd and 4th Layers)		
	Power (W)	Pressure (mTorr)	Time (Seconds)	Power (W)	Pressure (mTorr)	Time (Seconds)
1	50	3	60	70	15	1800
*	Gas and flow rate undocumented					

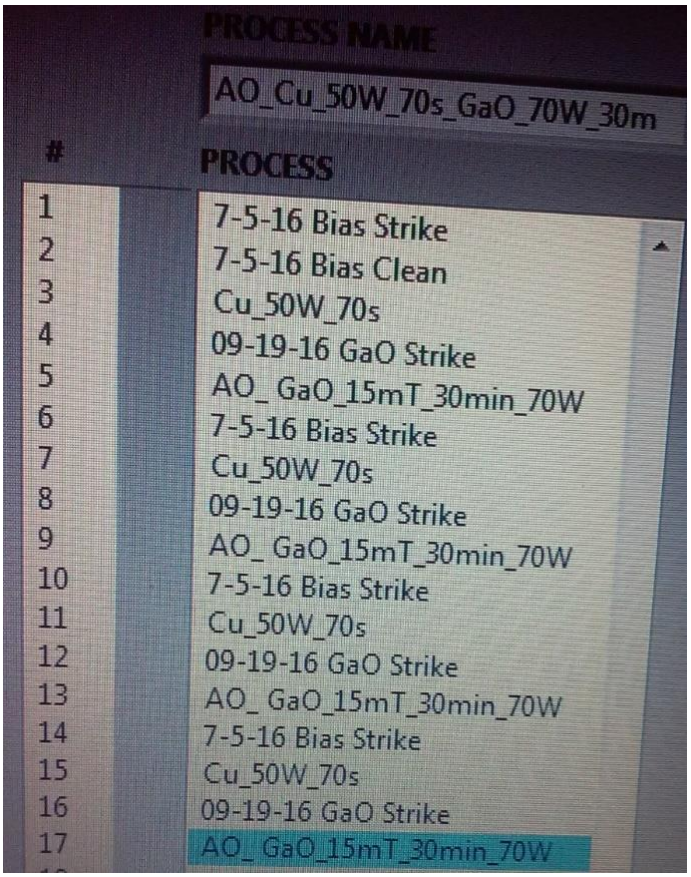

Figure 5.7: Process for GaO and Cu

The process aborted on its own. There was no plasma on the Gallium Oxide target. The pressure was changed to 15 mTorr on the advice of a fellow researcher. The pressure for the copper strike layer was changed to 3 mTorr. The pair of copper and gallium oxide layers were repeated three more times in the process to create a single eight-layer deposition with four layers of copper and four layers of gallium oxide.

The process successfully completed with no loss of plasma. The sample was prepared to be measured with an atomic force microscopy system (AFM), but was postponed and eventually dropped. The AFM was in disrepair when initially requested and the lab technician wasn't readily available. There was no lab technician to test the samples with a scanning electron microscope (SEM).

5.1.3 Silver on Glass Trials

The first silver trials were deposited on glass slides. Initial steps were taken to find the minimum power required to create plasma using the silver target. The pressure was set to 20 mTorr with an argon flow of 15 sccm. The minimum power was found to be 10 Watts. The strike and clean layers were set to 20 W.

Before depositing silver, new layers for striking and cleaning the substrate were created. The length of the strike time was initially set to 10 seconds at 3 mTorr, and the clean time was set to 60 seconds at 20 mTorr. The change in pressure between the strike and clean layers is used to dislodge loose particles from the substrate.

After deposition of the first four samples, the silver films appeared brownish in color. The adhesion on all the samples were very weak. The coatings came off easily with just the slightest touch. The layer would probably not withstand another deposition on top.

Another round of depositions was performed at 20 mTorr for 60 seconds. The one-minute deposition was to see if increasing the deposition time resulted in better adhesion and color. The first deposition showed the same brownish color. Another researcher advised that the color could be caused by Argon poisoning. Nitrogen was introduced into the chamber along with argon for another for the previous recipe. The strike and clean layers for the silver target were also switched to nitrogen.

Table 5.3: Silver on Glass Recipes

Ag on Glass					
Sample	Power (W)	Pressure (mTorr)	Time (Seconds)	Gas	Flow (sccm)
1	30	5	10	Ar	15
2	30	20	10	Ar	15
3	50	5	10	Ar	15
4	50	20	10	Ar	15
5	40	20	60	Ar	15
6	40	20	60	Ar : N	10 : 5

Both samples showed thicker coatings. The sample with nitrogen produced a more silver colored coating on the glass. All samples were sent for XPS measurements.

The data returned was in terms of the etch depth, shown in Figure 5.8. More information could be obtained by looking at the binding energy for silver versus etch depth. Figure 5.8 shows the profile of the XPS results for silver at 30 W at 5 mTorr. The presence of silver drops at around 10 nm.

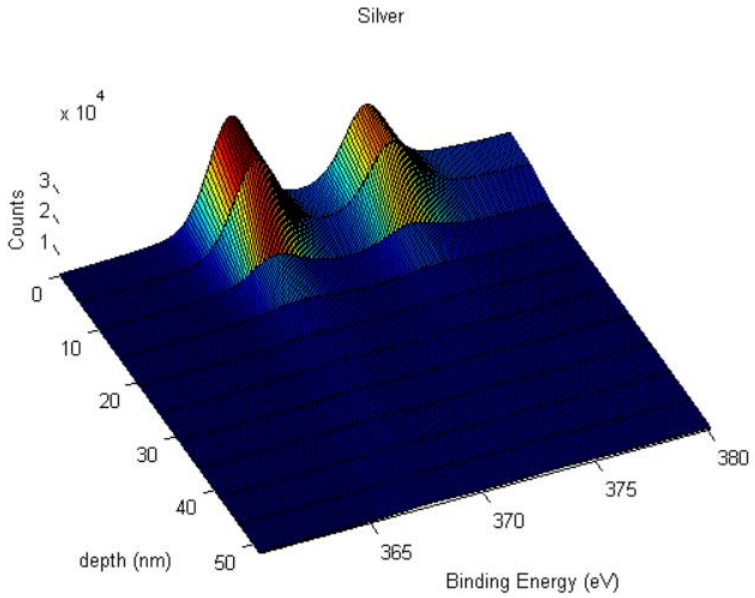

Figure 5.8: Silver Results

Figure 5.9 shows the 30 W at 20 mTorr deposition for silver and Figure 5.11 shows results for the 50 W at 5 mTorr deposition. There is a drop off in counts around 10 nm for the 5 mTorr deposition. The 30 W at 20 mTorr deposition dropped off around 20 nm.

Figure 5.12 shows the results for the 50 W at 5mTorr deposition. The drop in silver occurs between 5 nm and 10 nm. The thickness is around the desired size. The 50 W samples showed more counts for silver than the 30 W samples. The pressure at 20 mTorr for 50 W reduced the deposition rate while having the opposite effect for 30 W.

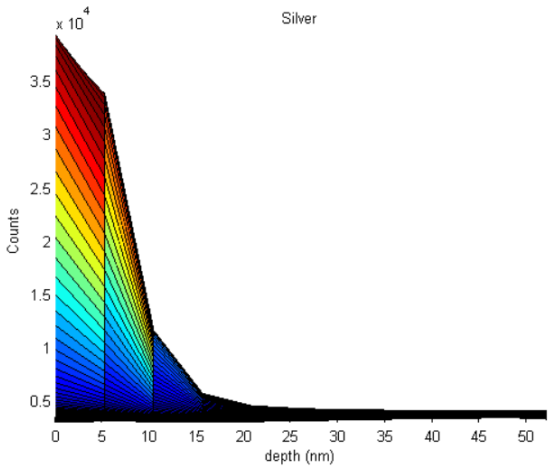

Figure 5.9: Ag, 30W, 5 mTorr

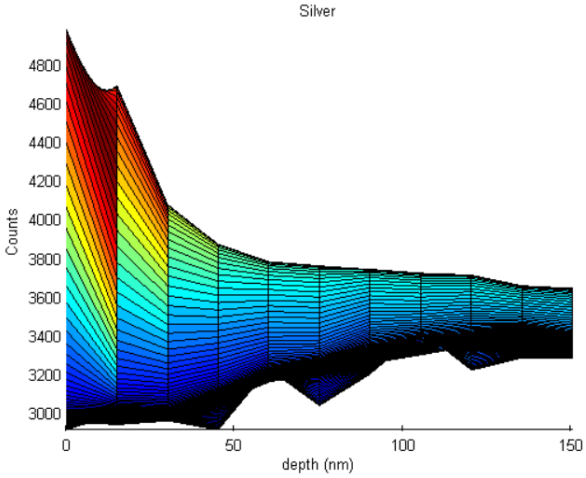

Figure 5.10: Ag, 30W, 20 mTorr

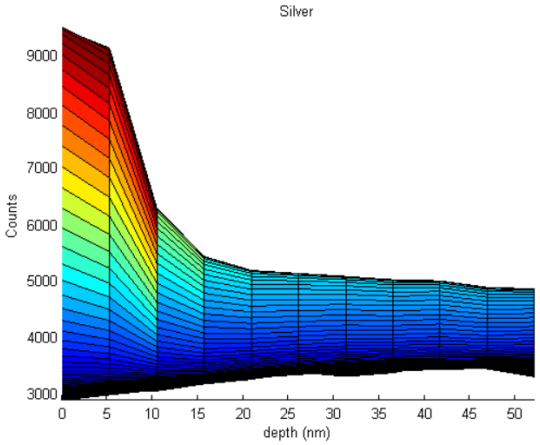

Figure 5.11: Ag, 50W, 5 mTorr

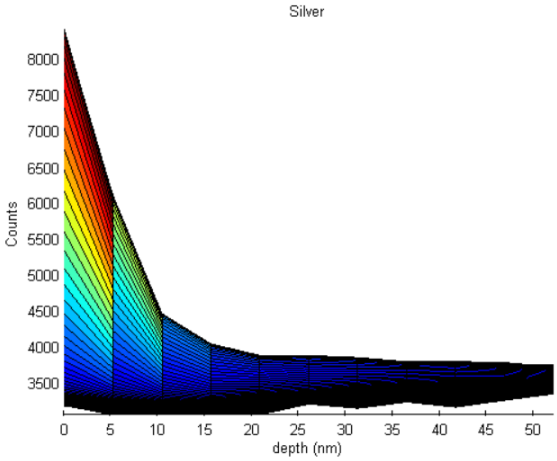

Figure 5.12: Ag, 50W, 20mTorr

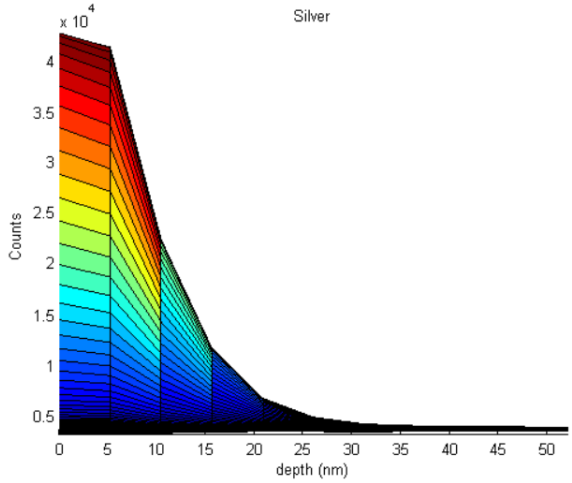

Figure 5.13: Ag, 40 W, 20 mTorr

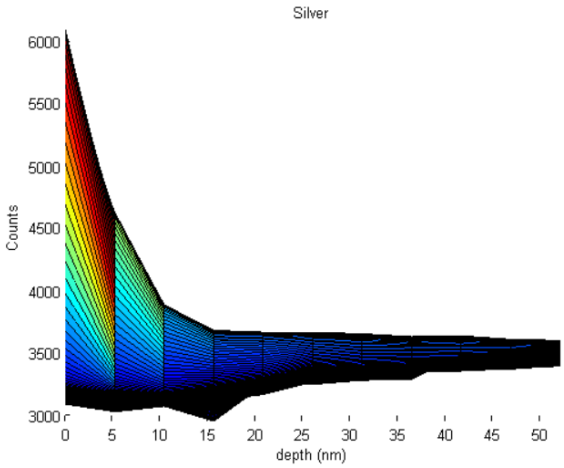

Figure 5.14: Ag, 40 W, 20 mTorr (N)

The last set of results for 40 W show the deposition of silver at 20 mTorr in Figure 5.13 and Figure 5.14 for the sample with nitrogen. Despite the difference in counts, Figure 5.13 indicates a thickness above 10 nm, while Figure 5.14 starts dropping before 5 nm.

It is possible that the weak adhesion created inaccuracies in the XPS measurements. Even though the thicknesses were around the goal of 10nm, some of the depositions could have less dense layers. The addition of nitrogen benefitted the last deposition of silver.

5.1.4 Silver on Fused Silica Trials

The silver trials were continued with fused silica wafers. An initial sample was created on glass with high power and low pressure to test the results of silver adhesion. The gas flowing into the chamber was changed to nitrogen only. The sample was cleaned afterwards with alcohol and showed stronger adhesion.

Fused silica wafers were cut into quarters to get multiple depositions out of a single wafer. The first sample on fused silica produced was at 70 W at 5 mTorr. The coat time was dropped to 15 seconds. The result was a similar brown color with weak adhesion.

A second and third run at 10 seconds and 20 seconds resulted in a silver color on the film with a semi-weak adhesion. The 10 second deposition showed a similar brown color while the 20 second deposition was silver in color. The first three results indicated a minimum of 20 seconds for silver deposition.

Not knowing the deposition rate, the coat time was kept to 20 seconds while the power and pressure were changed. Six samples were created at 50 W and 70 W for pressures at 5 mTorr, 15 mTorr and 20 mTorr, as shown in Table 5.4, to better control the variables of the experiment while making more samples during the session of using the magnetron.

Table 5.4: Silver Recipes

Ag on Fused Silica					
Sample	Power (W)	Pressure (mTorr)	Time (Seconds)	Gas	Flow (sccm)
1	50	5	20	N	15
2	50	15	20	N	15
3	50	20	20	N	15
4	70	5	20	N	15
5	70	15	20	N	15
6	70	20	20	N	15

With a new technician operating the SEM, all samples were prepared for SEM measurement. The SEM could not measure at levels below 100 nm. The samples could not be recovered and were considered a loss. The samples did show that there is a minimum limit to the deposition time. Additionally, the silver layers deposited at 5 mTorr had better adhesion than 15 and 20 mTorr.

5.1.5 Silver and BST on Fused Silica Wafer Trials

The new BST target required new strike and clean layers. The silver strike and clean layers were used as templates while switching the DC gun to the RF gun. The power to the RF gun was set to 30 W. The coat time for the BST clean layer was set at 120 seconds. Other parameters were kept the same.

While testing the BST strike layer, the sensor failed to detect plasma and the process would turn off during deposition. The threshold voltage for the plasma sensor was lowered to overcome the problem. An initial deposition was made at 60 W. The BST layer ran for 20 minutes.

A second layer was tested for 30 W. The process aborted near the start of the layer. The process was repeated for 40 W with the process aborting at around the same time. During the last

deposition, a visual inspection of the target holder showed that the plasma would not turn on until the shutter for the BST target opened. Plasma was also not seen for the strike and clean layers. Plasma was likely created when the power went up to 60 W and the shutter opened, whereas power up to 40 W was not high enough. The sudden creation of plasma at a high power could break the target.

The solution was to create a new layer, BST Ignite, to increase the pressure of the BST strike layer from 20 mTorr to 25 mTorr to create plasma. And instead of shutting off after the layer is finished, the power was held at 30 W and carried over to the BST clean layer before dropping to a lower pressure to avoid having to create plasma again. The same plasma was also carried over to the deposition layer while raising the power and pressure to deposition levels. The ramp up times for BST clean and the deposition layers were left at the same value.

Previous research into BST deposition had shown a higher refractive index for layers deposited at 10 mTorr compared to 5 mTorr with an applied RF power of 75 W on the target [46]. A slightly lower power of 70 W was chosen for BST depositions.

A test deposition was prepared for a one-minute deposition of silver and a one-hour deposition of BST. A sample was prepared and placed into the chamber. Silver was deposited on large section of the fused silica. The sample was retrieved and tape was place on top of the silver dividing the deposition. The sample was placed back into the chamber.

Before starting the BST deposition, the argon gas flow was lowered to 10 sccm based on advice from other researchers that ceramic deposition didn't not need a high argon flow. The process was started and plasma was observed five minutes into the BST deposition layer before leaving the magnetron operating overnight. The process completed successfully where the final layer deposited was the BST layer, as seen in Figure 5.15.

Table 5.5: Silver and BST Recipes I

Ag and BST on Fused Silica						
Sample	Ag (1st Layer)			BST (2nd Layers)		
	Power (W)	Pressure (mTorr)	Time (Secs)	Power (W)	Pressure (mTorr)	Time (Secs)
1	70	5	60	70	10	3600
*	Nitrogen: 15 sccm			Argon 10 sccm		

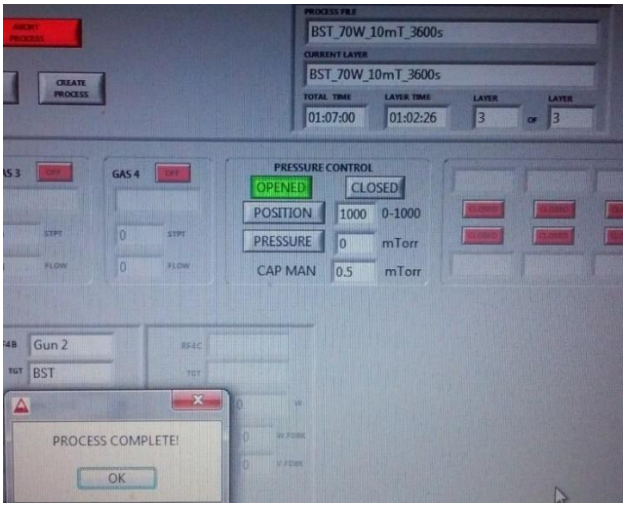

Figure 5.15: Process Complete for Ag BST Deposition

As shown in Figure 5.16, the deposition of BST on silver was clearly visible, but the bottom layer of silver appeared completely gone. The section of silver protected by the tape was still visible on this sample with a brownish color to the layer.

Figure 5.16: Ag BST Test Sample

The experiment was continued to anneal the sample. A layer was created without deposition where the temperature was set to 100º C and the soak time set to 1 minute and 30 seconds. While Figure 5.17 shows the layer annealing with argon at 20 sccm, actual annealing of BST was performed without additional gas flowing into the chamber. Metal sample holders were used to secure the glass onto the substrate holder.

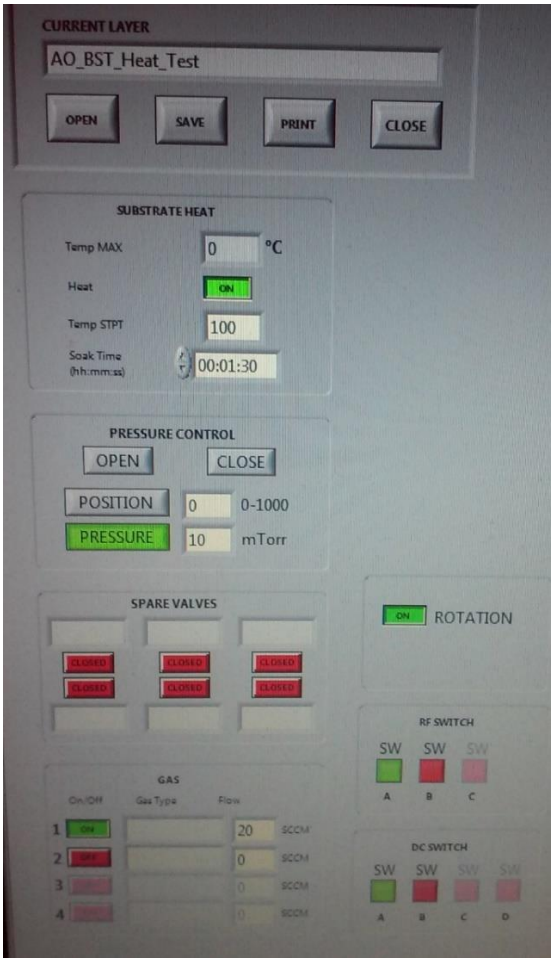

Figure 5.17: Annealing Layer

After the test annealing, the sample was brought out of the chamber. The glass appeared burnt, but the problem was a brown film developing on the bottom of the substrate, shown in Figure 5.18. Since the substrate holder contains depositions from previous use and the glass was

directly on top of the holder, some of the previous depositions was likely transferred to the bottom. The issue was resolved by using a separate, unbroken wafer to shield the bottom of the sample from the holder.

Figure 5.18: Substrate Contamination from Annealing

Six more samples were created for silver deposition for 30 seconds and BST deposition of 15 minutes, 30 minutes and 45 minutes as well as another set of samples for silver deposition for 60 seconds and BST deposition of 15 minutes, 15 minutes (80 W) and 30 minutes (80 W). The gas for silver was also adjusted to nitrogen only.

Table 5.6: Silver and BST Recipes II

Ag and BST on Fused Silica						
Sample	Ag (1st Layer)			BST (2nd Layers)		
	Power (W)	Pressure (mTorr)	Time (Secs)	Power (W)	Pressure (mTorr)	Time (Secs)
1	70	5	30	70	10	900
2	70	5	30	70	10	1800
3	70	5	30	70	10	2700
4	70	5	60	70	10	900
5	70	5	60	80	10	900
6	70	5	60	80	10	1800
*	Nitrogen: 15 sccm			Argon: 10 sccm		

The same process was repeated for all six samples where a large area was deposited with silver and then a strip is covered with tape and BST is deposited. The figures below show an example with two different samples.

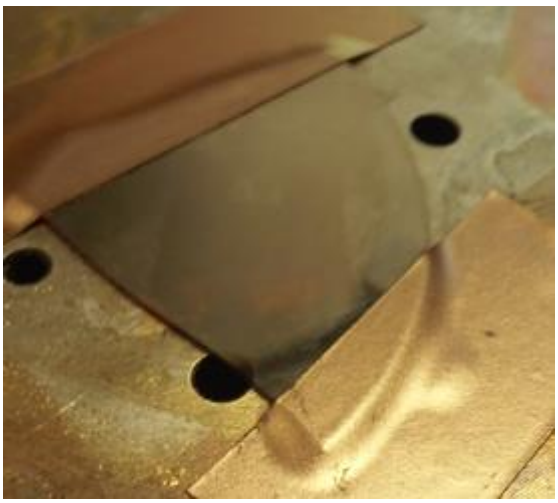

Figure 5.19: Ag Sample

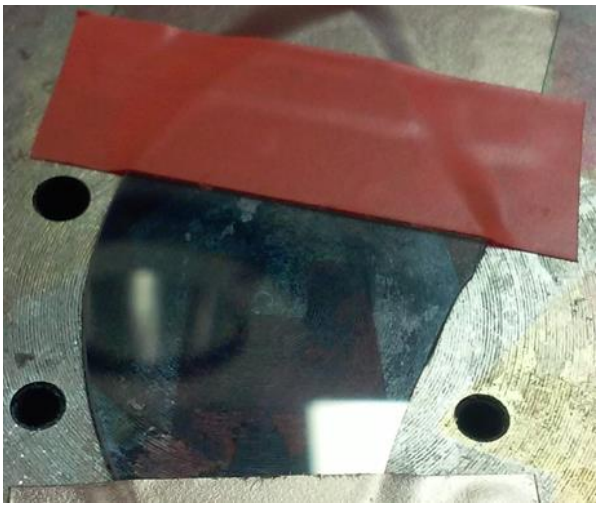

Figure 5.20: Tape on Ag Before BST

The samples were annealed at 750º C, above the Cure Temperature, using the same heating wafer below to protect the bottom surface [47]. The result was a clean sample with a visible strip of silver and an area of BST. It was still unknown what had happened to the silver under the BST layer.

Three additional samples were created with an additional layer of silver. These runs were set up so that a single process can deposit the three layers instead of running the depositions separately. One sample was annealed using a furnace at 800º C for one hour. The bottom silver layer became cloudy. The glass developed a crack after deposition.

A small piece from one of the samples was cut to be observed with the SEM. The piece came from a section of the sample with silver and BST layers, shown in Figure 5.21. The measurement can be seen in Figure 5.22. Despite the longer deposition time, the SEM could not

see close enough. While unconfirmed, the image was thought to show a deposition of BST (dark grey) on top of silver (light grey) where only a small section of silver was exposed.

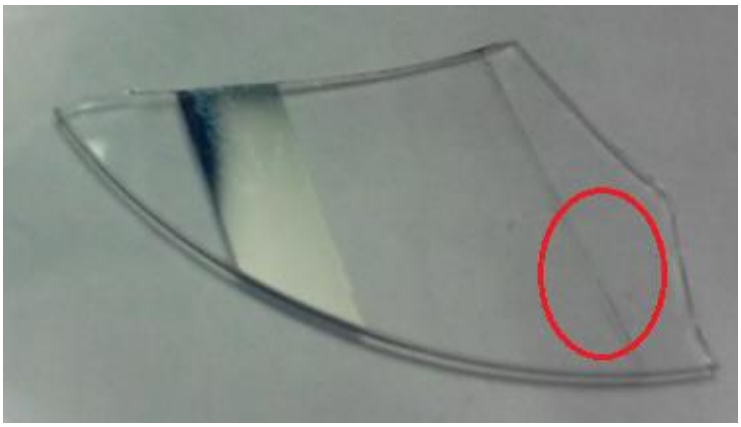

Figure 5.21: Location of Sample Cut for SEM

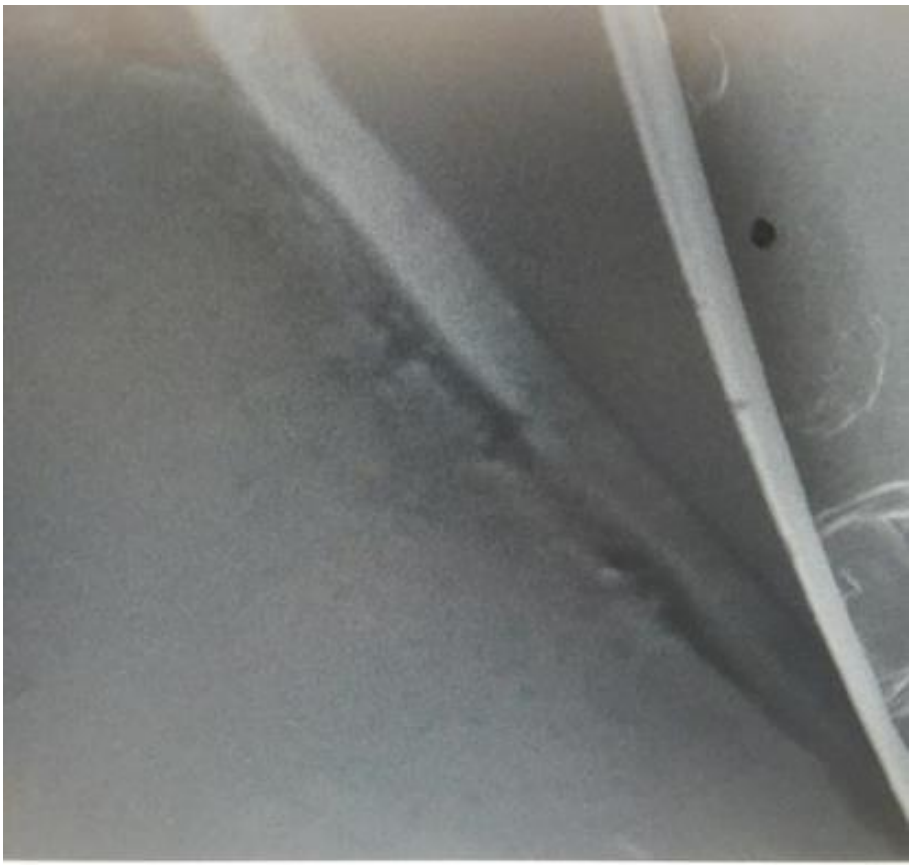

Figure 5.22: SEM Image of Sample

5.2 Complete Samples and Results

5.2.1 Group A

Samples for the first group were created with two layers of silver and two layers of BST. The first three samples used silver with 70 W at 5 mTorr for 30 seconds. The fourth and fifth samples had one minute of silver deposition, and the seventh sample had 20 seconds of silver deposition.

Sample A-1 had 5 minutes of BST deposition, samples A-2 and A-3 had 10 minutes of BST deposition, samples A-4 and A-5 had 15 minutes of BST deposition, and sample A-7 had 3 minutes of deposition. The fifth sample used a power of 80 W on the BST target. Depositions times were decreased due to time constraints. Table 5.7 shows the recipe of six samples fabricated in this group. Sample A-6 was omitted from the results.

Table 5.7: Group A - Silver and BST Recipes I

Ag and BST on Fused Silica							
Sample	Ag (1st & 3rd Layer)			BST (2nd & 4th Layers)			
	Power (W)	Pressure (mTorr)	Time (Seconds)	Power (W)	Pressure (mTorr)	Time (Seconds_	
						2nd Layer	4th Layer
A-1	70	5	30	70	10	900	300
A-2	70	5	30	70	10	1800	600
A-3	70	5	30	70	10	2700	600
A-4	70	5	60	70	10	900	900
A-5	70	5	60	80	10	900	900
A-6	–	–	–	–	–	–	–
A-7	70	5	20	70	10	180	180
*	Nitrogen: 15 sccm			Argon: 10 sccm			

Samples A-1, A-2 and A-7 were annealed using the magnetron. Samples A-3, A-4, A-5 and A-7 were annealed in by furnace. Sample 3 was accidentally left in the furnace for 23 hours. The deposition appeared yellowish with the silver layers missing. Samples A-4 and A-5 were also annealed by furnace for one hour. Three more samples were while waiting for a technician

to set up the XPS measurements. These samples were annealed in the magnetron all at once for 1 hour at 800º C.

Table 5.8: Group A - Silver and BST Recipes II

Ag and BST on Fused Silica								
Sample	Ag (1st & 3rd Layer)				BST (2nd & 4th Layers)			
	Power (W)	Pressure (mTorr)	Time (Seconds)		Power (W)	Pressure (mTorr)	Time (Seconds)	
			1st Layer	2nd Layer			2nd Layer	4th Layer
A-8	70	5	15	15	70	10	60	120
A-9	70	5	40	40	70	10	240	360
A-10	70	5	60	50	70	10	480	600
*	Nitrogen: 15 sccm				Argon: 10 sccm			

The data from the XPS is presented in a complete survey for sample A-1, shown in Figure 5.23. The data was normalized to the highest binding energy by the technician. Since elements have different binding energies, the plot can be focused on specific elements using known ranges of binding energy. The elements barium, strontium, titanium, oxygen, silver and silicon were selected for closer inspection.

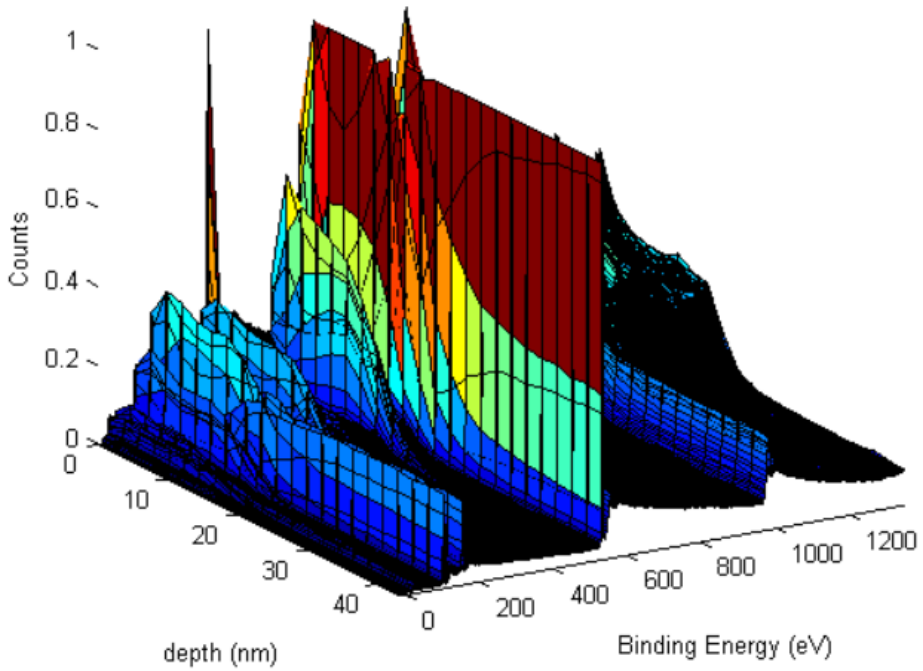

Figure 5.23: Sample A-1 Survey

Sample A-1 had an initial 30 second deposition of silver, a 15-minute deposition of BST, followed by another 30 second deposition of silver and a 5-minute deposition of BST. The range for Barium from Sample A-1 is show in Figure 5.24. The survey plot is limited from 775 eV to 800 eV to get a better view of Barium counts.

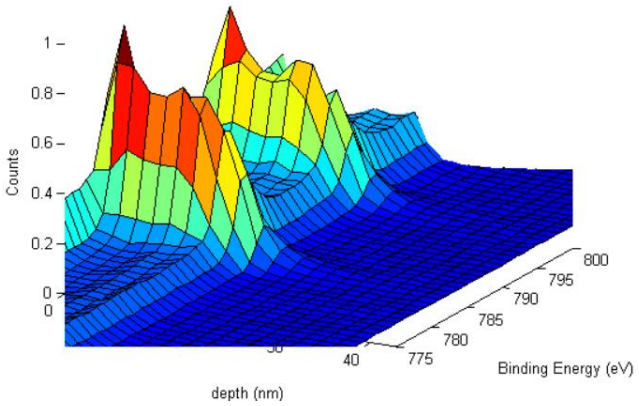

Figure 5.24: Sample A-1 Barium I

To better view the counts, the plot is shown on the depth and counts axes only. The Figure 5.25 shows the XPS detecting Barium down to around 18-19 nm. This is compared to the plot for silver. Figure 5.26 shows Silver detected down to 18 nm.

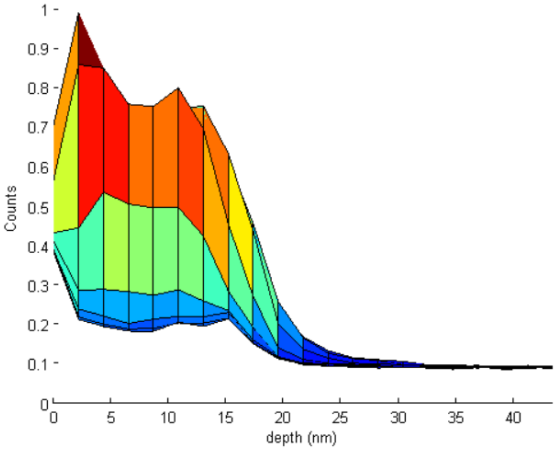

Figure 5.25: Sample A-1 Barium II

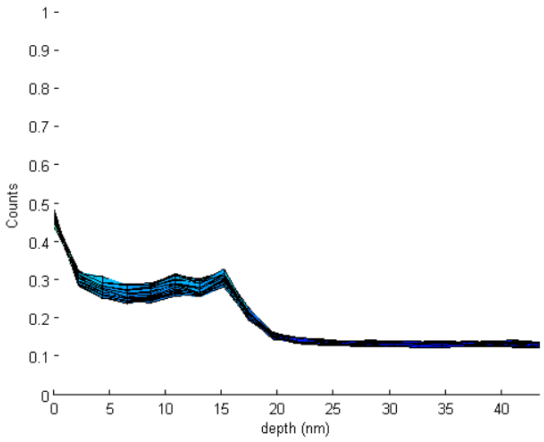

Figure 5.26: Sample A-1 Silver

Figures 5.25 and 5.26 indicate there was no clear separating between the silver and BST layers. While there are peaks in the figures influenced by the silver layers, the materials appear to have mixed together.

The oxygen plot can hold information in regards to the thickness. The binding energy of oxygen will shift when the XPS hits fused silica. Figure 5.27 shows Oxygen detected between the deposition and the substrate. Figure 5.28 is a rotated view from above the plot. The shift can be seen occurring at around 16 nm.

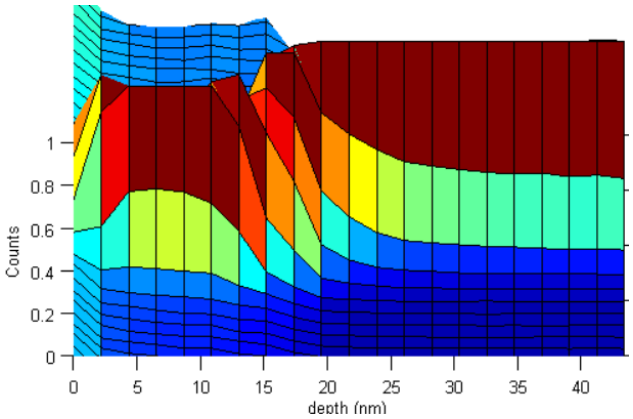

Figure 5.27: Sample A-1 Oxygen I

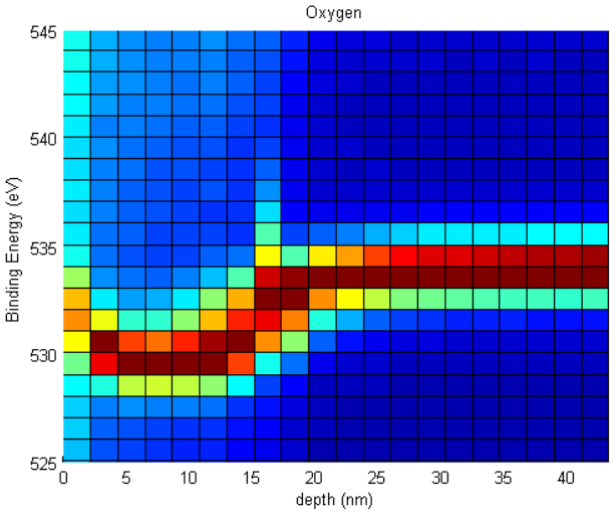

Figure 5.28: Sample A-1 Oxygen II

A profile of the peak counts of selected elements in the XPS was included in the data. Figure 5.29 shows all the chosen elements in a two-dimensional plot for sample A-1. It does not show the shift in binding energy for oxygen indicating the start of the substrate. Silver can be seen deposited on the substrate in red. BST was detected more toward the top, but throughout the deposition as well. Two XPS sample were prepared for sample A-7, shown in Figures 5.30 and 5.31. Both figures show that silver had migrated to the top instead of having two defined layers. Barium was found throughout the deposition, including into the fused silica substrate.

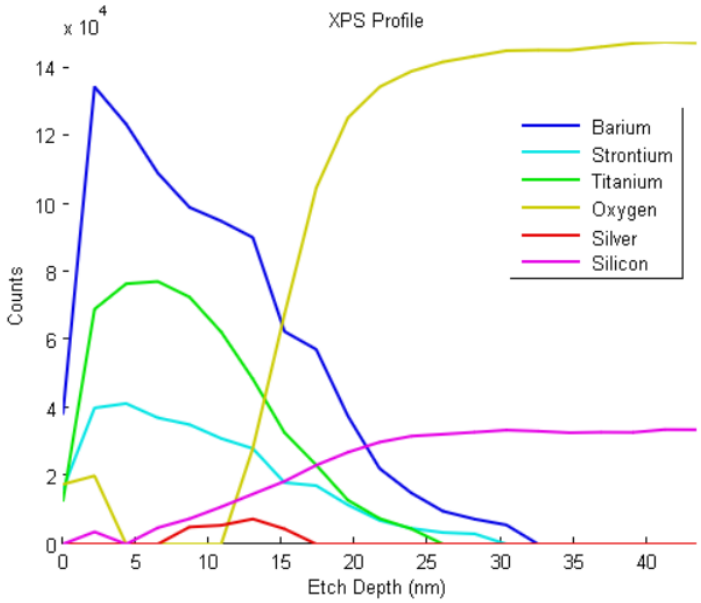

Figure 5.29: Sample A-1 Profile

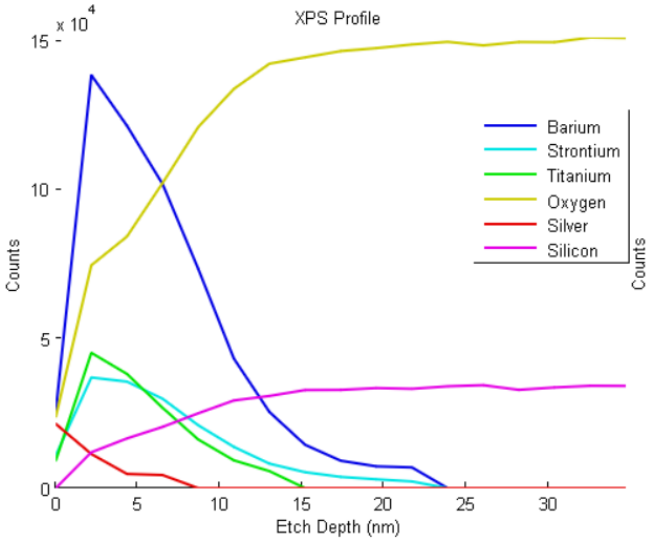

Figure 5.30: Sample A-7 Profile I

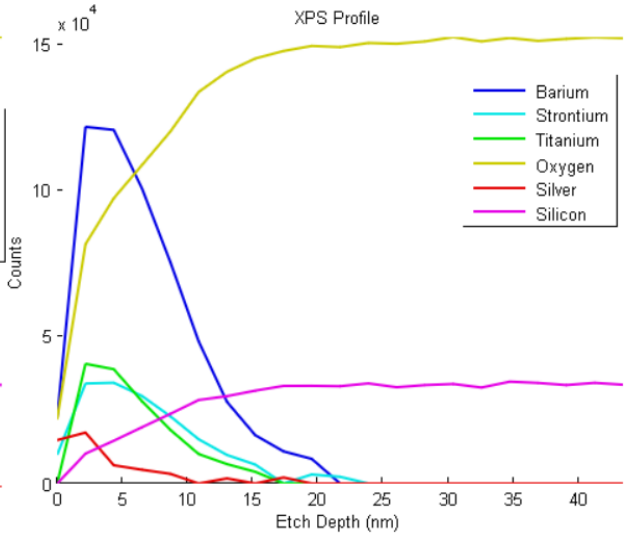

Figure 5.31: Sample A-7 Profile II

The mix in elements could have been cause by several reasons including the particles accelerating into the substrate too fast or the layers mixing during annealing. The recipe would have to be altered once all the measurements arrived. The elemental profiles for other samples were not provided.

The Figures 5.32 and 5.33 show the shift in oxygen's binding energy for samples A-3 and A-4. The shift for A-3 occurs at 78 nm while the shift for A-4 is at 38 nm.

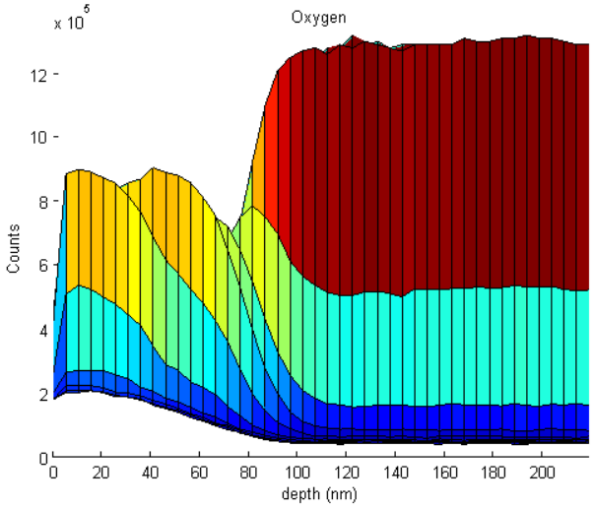

Figure 5.32: Sample A-3 Oxygen

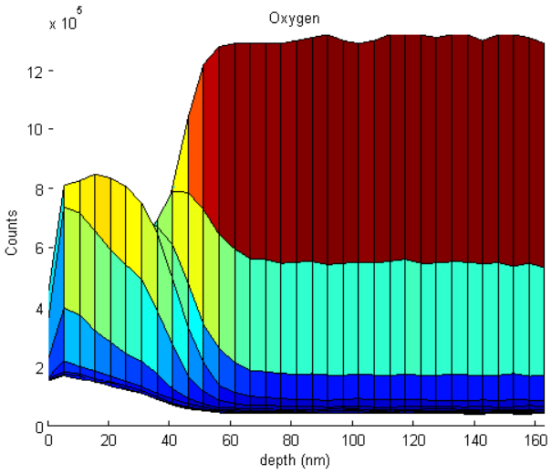

Figure 5.33: Sample A-4 Oxygen

The measurements for silver and barium were compared for both samples A-3 and A-4, but had similar results as samples A-1 and A7. There was no clear distinction between the layers. There was a larger count for barium for sample A-3 around 40 nm to 70 nm in Figure 5.34. This was most likely from the 45-minute deposition of BST.

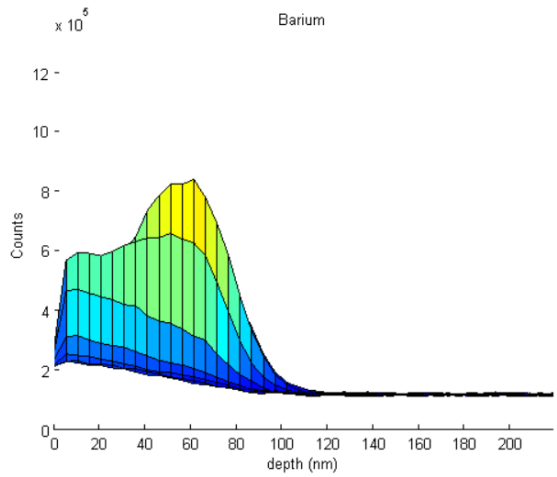

Figure 5.34: Sample A-3 Barium

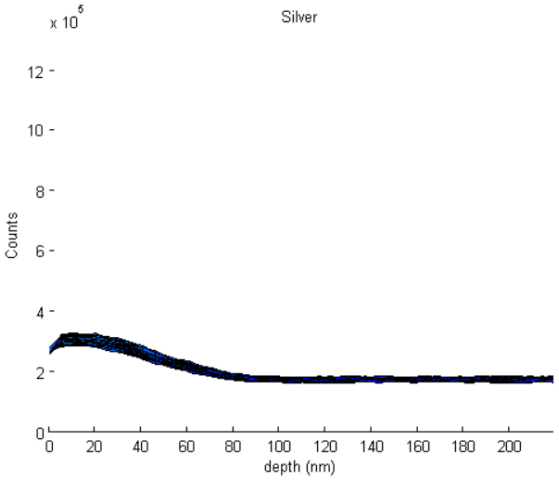

Figure 5.35: Sample A-3 Silver

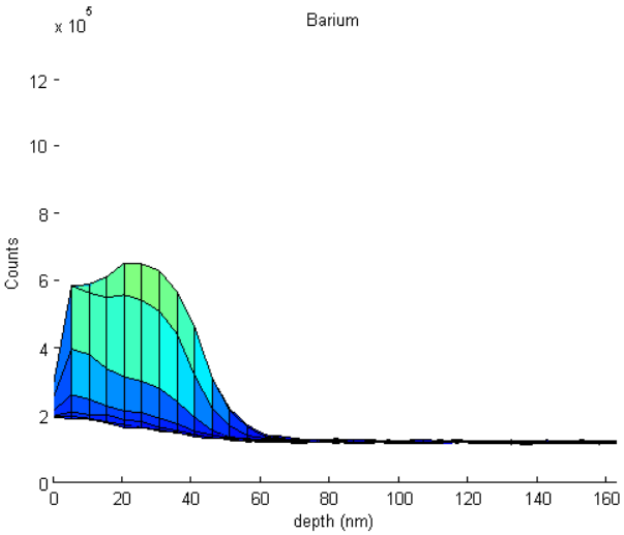

Figure 5.36: Sample A-4 Barium

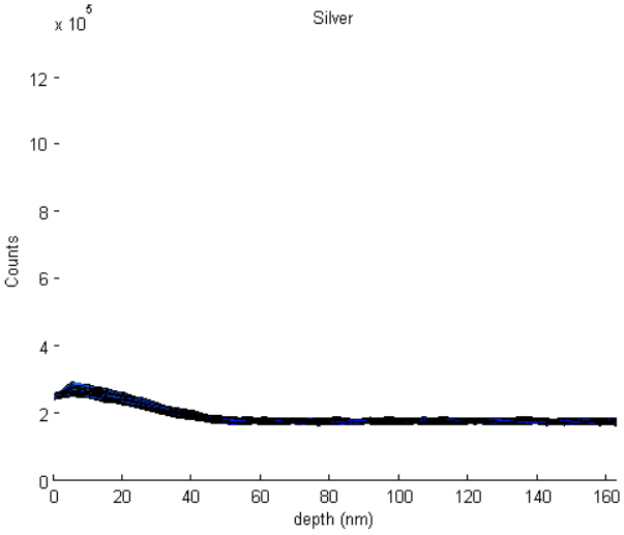

Figure 5.37: Sample A-4 Silver

There were other problems with samples A-8, A-9 and A-10. Sample A-8 was placed upside down on the sample holder of the XPS. Samples A-9 and A-10 did not measure deep enough having gone 24 nm and 37 nm into the sample respectively. The deposition times for BST were very short for all three samples so the layers would be thinner.

5.2.2 Group B

Depositions for Group B were performed after obtaining results from Group A. Three new layers for silver and two new layers for BST were created in the magnetron. Samples consisted of 4 layers with two layers of silver and two layers of BST. Deposition rates were still unknown, but estimations were made based on the total thicknesses from the Group A.

Samples B-3, B-4, and B-6 were annealed using the magnetron at 750ºC under vacuum to compare between annealed and non-annealed samples. XPS parameters were provided to narrow the results of the measurements to their estimated thicknesses. Table 5.9 shows the recipes for the separate layers and the samples that were annealed.

Table 5.9: Group B - Silver and BST Recipes

Ag and BST on Fused Silica							
Sample	Ag (1st & 3rd Layer)			BST (2nd & 4th Layers)			750ºC
	Power (W)	Pressure (mTorr)	Time (Seconds)	Power (W)	Pressure (mTorr)	Time (Seconds)	
B-1	70	5	90	70	10	300	
B-2	70	5	120	70	10	390	
B-3	70	5	90	70	10	300	✓
B-4	70	5	120	70	10	390	✓
B-5	70	5	180	80	10	480	
B-6	70	5	180	80	10	480	✓
*	Nitrogen: 15 sccm			Argon: 10 sccm			

The parameters entered in the XPS for the first four samples were accidentally switched by the technician. Samples B-1 and B-3 were supposed to be measured down to 30 nm and samples B-2 and B-4 down to 60 nm. Instead, B-1 and B-2 were measured to 60 nm and B-3 and B-4 only to 30 nm.

Sample B-3, not shown, had oxygen beginning to shift in binding energy, but 30 nm was not deep enough to confirm. No shift was visible for sample B-4 since the maximum etch depth was not deep enough. The XPS measurements for samples B-5 and B-6 were also not deep enough to see the substrate at a maximum etch depth of 85 nm. Between these four samples, only the layers in sample B-3 were slightly distinguishable. Since the only difference between samples B-1 and B-3 was the annealing, the mixing of the two materials with annealing must have caused the depositions to expand.

Sample B-1 had a total thickness of 13 nm based on the shift in oxygen binding energy shown in Figure 5.38. From Figure 5.39, about 6 nm of barium was measured at the top of the sample. Silver was also detected closer to the substrate for a thickness of 7 nm in Figure 5.39. The two layers of BST appeared to have migrated to the top of the substrate above the silver depositions.

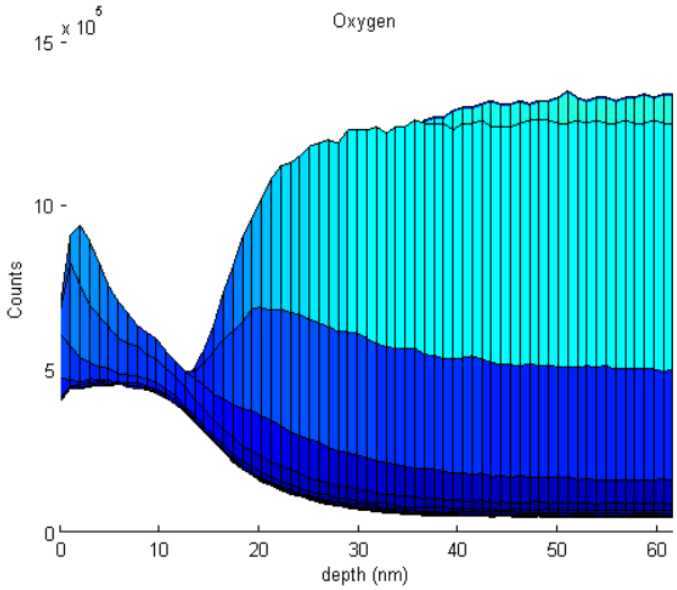

Figure 5.38: Sample B-1 Oxygen

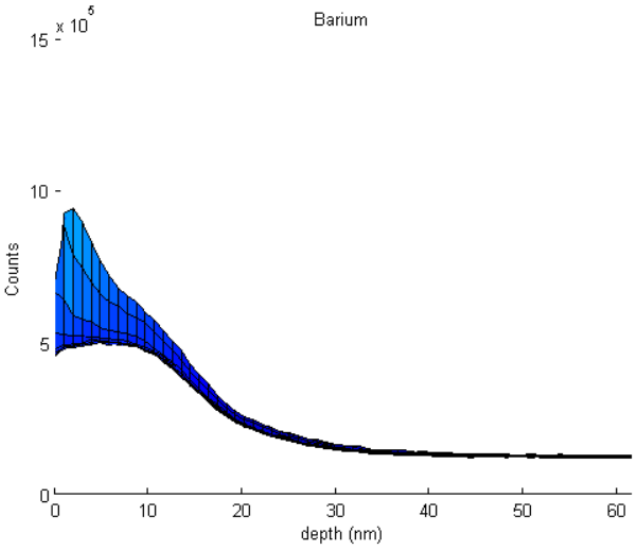

Figure 5.39: Sample B-1 Barium

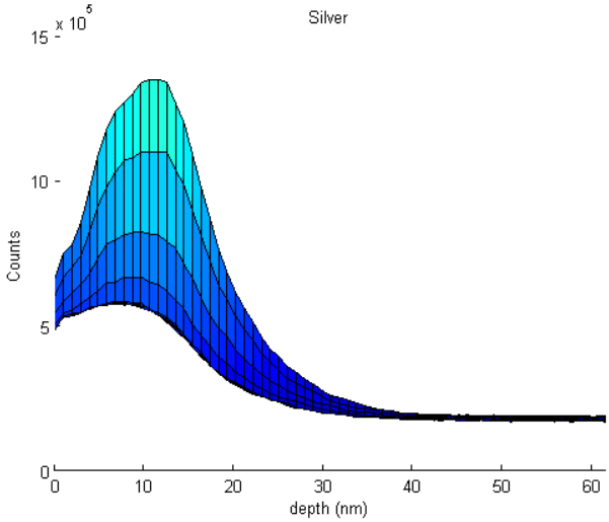

Figure 5.40: Sample B-1 Silver

The shift for sample B-2, in Figure 5.41, was at 20 nm. From Figure 5.42, about 7 nm of barium was measured. The barium results show a dip at 10 nm with another peak at 15 nm before dropping. Silver appeared at around 6 nm down to the substrate for a thickness of 13 nm.

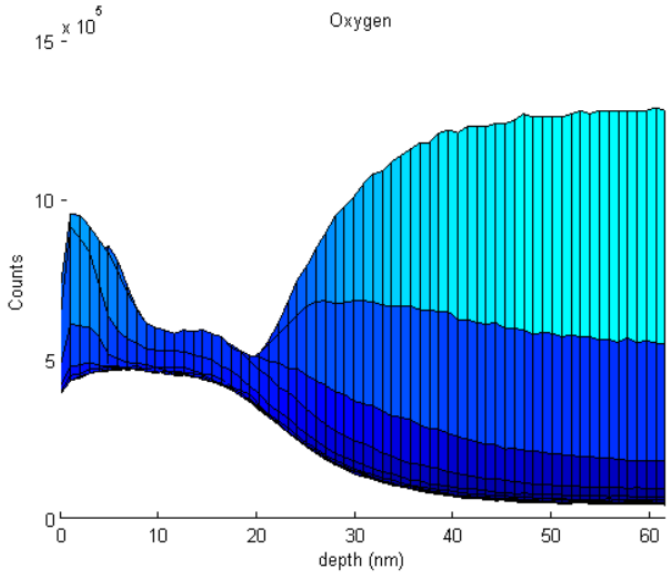

Figure 5.41: Sample B-2 Oxygen

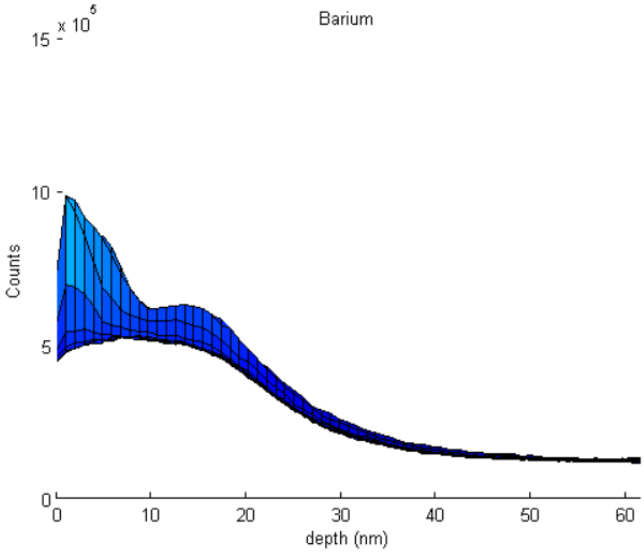

Figure 5.42: Sample B-2 Barium

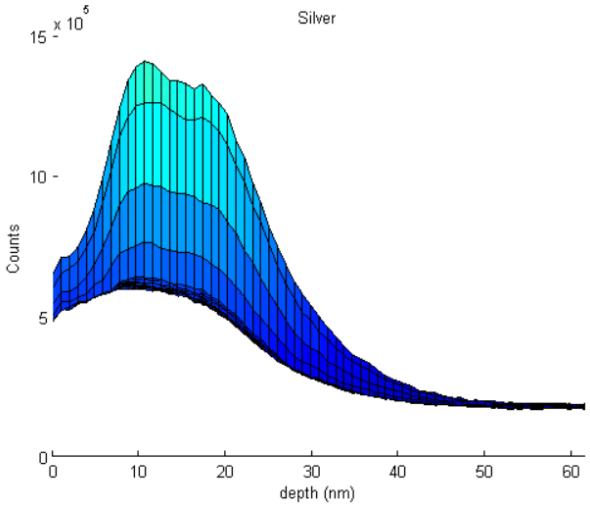

Figure 5.43: Sample B-2 Silver

Unlike the silver in Group A which appeared at the top, the silver in Group B stayed closer to the substrate. Since samples B-1 and B-3 were not annealed, something else was causing the layers to mix together. Some samples in Group A had longer depositions of BST which wound up in the bottom. The longer BST depositions could have pushed the particles

deeper into the other layers, but the same power was used in both groups. The power used on the silver target could also have been too strong for this deposition. A lower power could be used in future samples.

The process that contained the layers also included a bias strike and clean between each layer. Since the bias clean layer sends plasma to the substrate, this process could be weaking previous depositions. The first bias strike and clean layers were kept in the process for future depositions, but all the other bias strike and clean layers between silver and BST depositions were removed. And if a sample requires additional layers added onto the ones already on the sample, then the bias strike and clean layers are completely removed from the process so that only depositions layers are performed on the sample.

The reason for the samples expanding under heat also remained unknown. Since levels of barium were the same throughout B-3 and B-4 despite being lower than expected, the expansion of silver was likely due to BST mixed into the silver layers. Post-annealing thickness of entire deposition could remain closer to pre-annealing thickness if the process is corrected so that the individual layers stay intact.

Additionally, the pressure at which the depositions are annealed could also affect the melting point of silver. A lower pressure decreases the melting point of silver. The pressure could be brought up while letting gas flow into the chamber to allow the turbo pump to stabilize the pressure.

5.2.3 Group C

Samples for Group C were performed once the results for Group B were analyzed. Several parameters were changed for this group. The power applied to silver and BST was

lowered to 40 W, 50 W and 60 W. The deposition times were kept at 4 minutes for silver and 8 minutes for BST. Annealing was performed at 800ºC for one hour at 90 mTorr with nitrogen. Six new layers for the magnetron were created for silver and BST.

Table 5.10: Group C - Silver and BST Recipes

Ag and BST on Fused Silica						
Sample	Ag (1st & 3rd Layer)			BST (2nd & 4th Layers)		
	Power (W)	Pressure (mTorr)	Time (Seconds)	Power (W)	Pressure (mTorr)	Time (Seconds)
C-1	60	5	240	60	10	480
C-2	50	5	240	50	10	480
C-3	40	5	240	40	10	480
*	Nitrogen: 15 sccm			Argon: 10 sccm		

After the samples were created, a piece of sample C-1 was prepared for XPS analysis before running measurements on all samples in order to prevent from using the inaccurate parameters on all samples. The maximum etch depth was set to 23 nm on the XPS. The initial test detected barium as the top layer. The distinction between layers of BST and silver was not noticeable. The maximum etch depth for new measurements was extended to 68 nm for all three samples including C-1.

All three samples showed no oxygen binding energy shift within 68 nm. The XPS did not reach the substrate. The barium results for sample C-1, in Figure 5.44, show a peak at the top of the sample and a rising slope going past 68 nm. The silver results, in Figure 5.45, show a dip at the top of the sample and towards 68 nm.

Figure 5.44 also shows barium counts starting to rise. This meant that the XPS was only able to measure into the top layer of BST, the second layer of silver and into the first layer of BST. Despite not reaching the substrate, the layers are distinguishable. The deposition rate of silver was underestimated. The increase in deposition time created thicker layers of silver than expected.

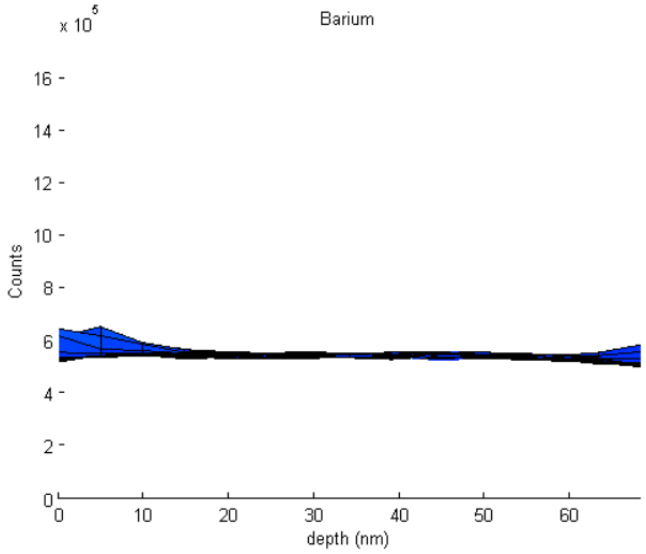

Figure 5.44: Sample C-1 Barium

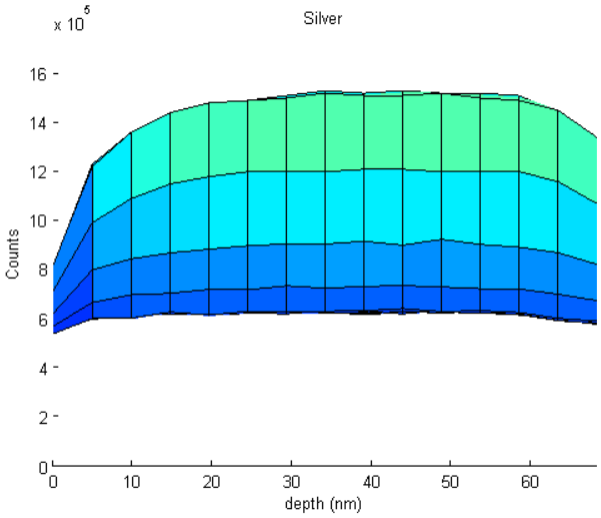

Figure 5.45: Sample C-1 Silver

Sample C-2, where power to both the silver target and BST target were 50 W, shows the peak of the bottom layer of BST at around 65 nm. The dip can also be seen in silver in Figure 5.47. The XPS measured past the center of the first BST layer but did not go into the bottom layer of silver.

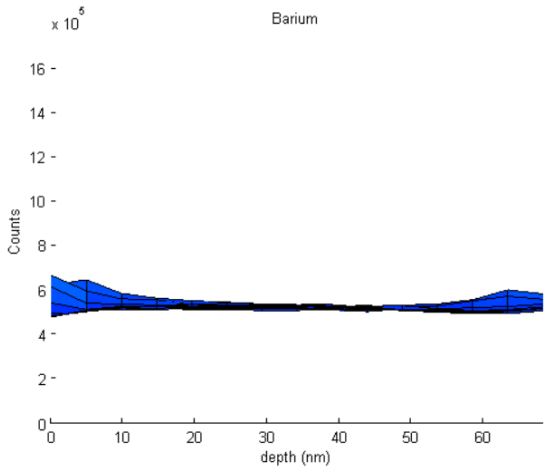

Figure 5.46: Sample C-2 Barium

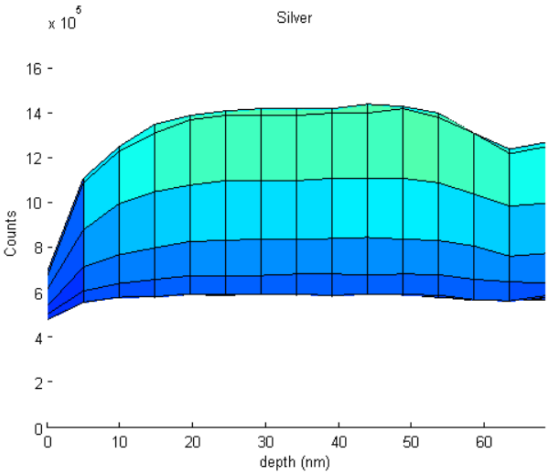

Figure 5.47: Sample C.2 Silver

Sample C-3 with power at 40 W showed a slightly thinner layer of silver with peaks in the first layer of barium at around 54 nm. The XPS measured past the top three layers and into the bottom layer of silver.

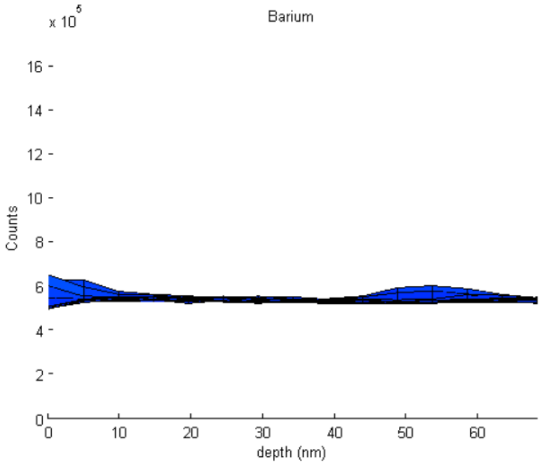

Figure 5.48: Sample C-3 Barium

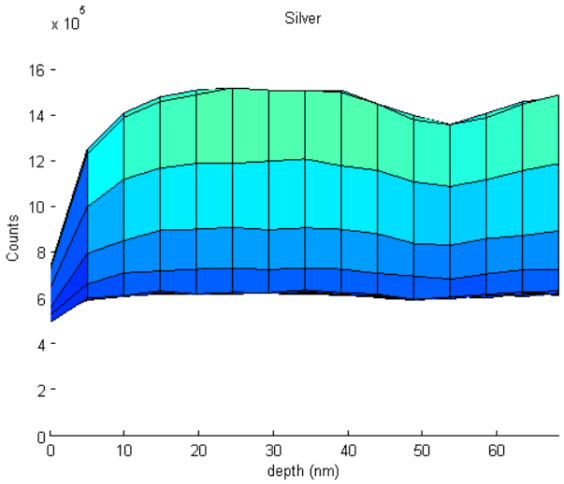

Figure 5.49: Sample C-3 Silver

There are now three results that can produce deposition rates for silver. The thicknesses for samples C-1, C-2 and C-3 were estimated to be 50 nm, 40 nm and 27.5 nm. The deposition rate for silver at 60 W was estimated at 12.5 nm/minute, 50 W was at 10 nm/min, and 40 W at 6.875 nm/min.

5.2.4 Group D

Two more samples were created using the results from Group C. The silver layers were deposited at 40 W for 90 seconds. A single BST layer was deposited at 40 W for 360 s. The lower power from Group C was used to see if mixing of layers was occurring during the BST deposition. Sample D-1 was annealed at 800ºC for 20 min and sample D-2 was annealed at 850ºC for one minute at 90 mTorr. The second sample was sent for XPS measurements.

Table 5.11: Group D - Silver and BST Recipes

Ag and BST on Fused Silica						
Sample	Ag (1st & 3rd Layer)			BST (2nd Layer)		
	Power (W)	Pressure (mTorr)	Time (Seconds)	Power (W)	Pressure (mTorr)	Time (Seconds)
D-1	40	5	90	40	10	360
D-2	40	5	90	40	10	360
*	Nitrogen: 15 sccm			Argon: 10 sccm		

At a maximum etch depth of 59 nm, the substrate was not detected, results not shown for Group C. The XPS results did not detect barium in the middle of the sample. Only silver was detected. The amount of silver deposited on the substrate was still more than estimated. Since the deposition time of BST was reduced, there was probably not enough time for the BST to adhere to the silver before building up.

5.2.5 Group E

While sample D-2 was undergoing XPS testing and since the magnetron became available, the first sample from Group E was deposited. The results from Group D were unknown at this point. Sample E-1 had increased deposition times of BST. Similar to Group D, sample E-1 was created with a BST layer between 2 silver layers. The sample was annealed at 800ºC for one minute.

Table 5.12: Group E - Silver and BST Recipes I

Ag and BST on Fused Silica						
Sample	Ag (1st & 3rd Layer)			BST (2nd Layer)		
	Power (W)	Pressure (mTorr)	Time (Seconds)	Power (W)	Pressure (mTorr)	Time (Seconds)
E-1	40	5	180	40	10	960
*	Nitrogen: 15 sccm			Argon: 10 sccm		

After receiving the D-2 results, the deposition times of silver for the rest of the Group E samples were decreased. The BST deposition times were increased further. Instead of depositing

three layers, these sample only had a layer of silver and a layer of BST. They were left unannealed. Sample E-1, E-2 and E-3 were submitted for XPS testing.

Table 5.13: Group E - Silver and BST Recipes II

Ag and BST on Fused Silica						
Sample	Ag (1st Layer)			BST (2nd Layer)		
	Power (W)	Pressure (mTorr)	Time (Seconds)	Power (W)	Pressure (mTorr)	Time (Seconds)
E-2	40	5	45	40	10	1440
E-3	40	5	50	40	10	1920
E-4	40	5	45	40	10	960
*	Nitrogen: 15 sccm			Argon: 10 sccm		

Similar to the samples in Group D, sample E-1 had no visible layer of BST between the two silver layers. The results are not shown, but this sample did have more silver than other group E samples.

Sample E-2 finally showed the binding energy shift of oxygen, in Figure 5.50. The shift occurred at 15 nm. BST and silver layers can be seen as the barium counts drop after a peak at 5 nm, in Figure 5.51, and the silver counts start to rise, in Figure 5.52. These results showed more barium than sample E.1.

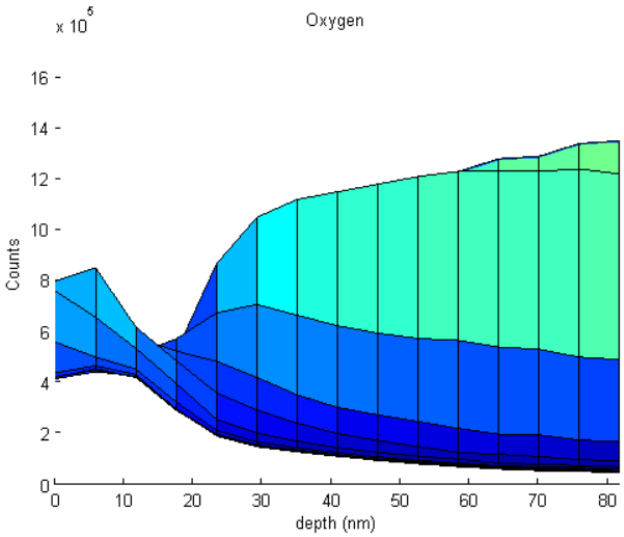

Figure 5.50: Sample E-2 Oxygen

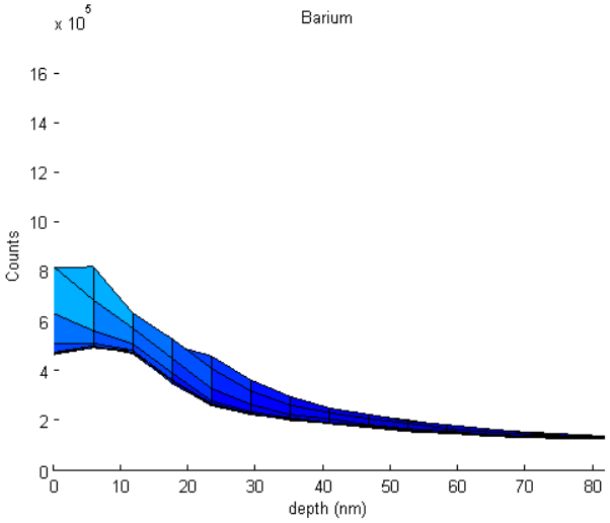

Figure 5.51: Sample E-2 Barium

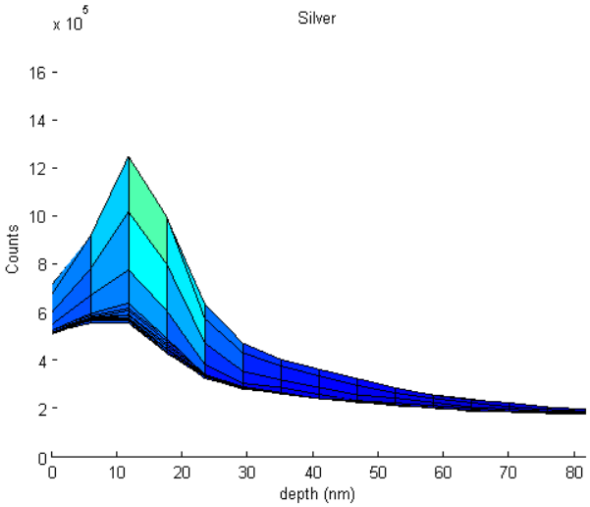

Figure 5.52: Sample E-2 Silver

Sample E-3 shows the start of the substrate at around 19 nm where the binding energy shift occurs for oxygen in Figure 5.53. The layer of silver on E-3 is thicker in Figure 5.55 than sample E-2. With a smaller number of layers to reduce the possibility of layers mixing with each other, these results can be used to develop a more accurate deposition rate of silver.

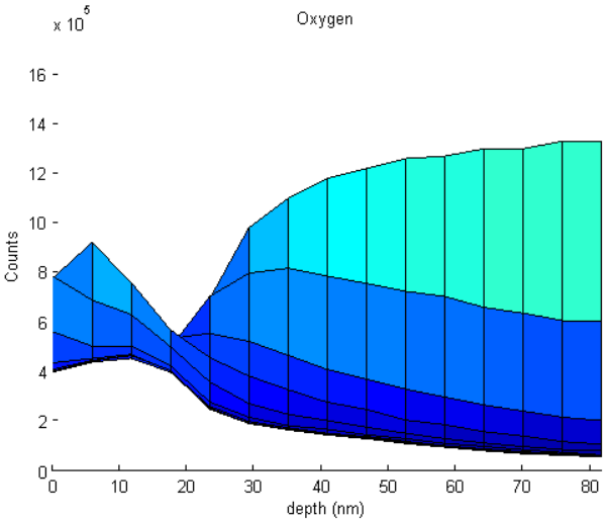

Figure 5.53: Sample E-3 Oxygen

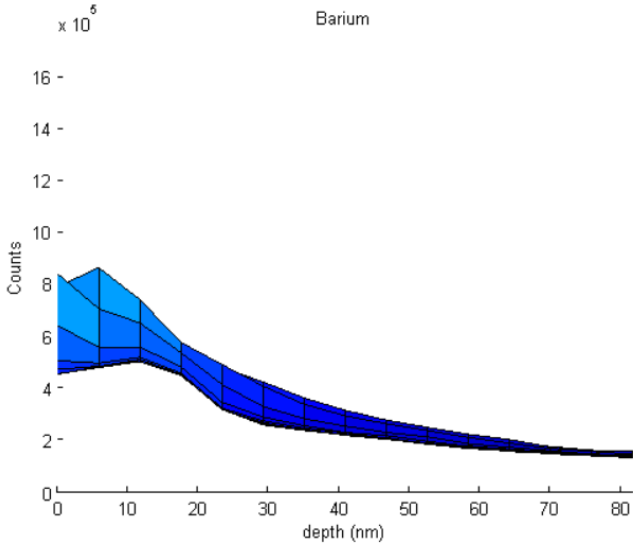

Figure 5.54: Sample E-3 Barium

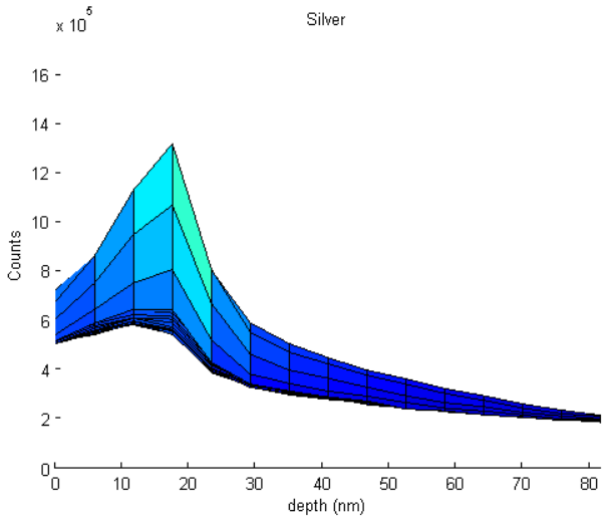

Figure 5.55: Sample E-3 Silver

Despite the longer deposition times of BST, the results were still around 10 nm. Considering that decreasing the pressure of silver helped with adhesion, BST could benefit from dropping the pressure to 5 mTorr. The pressure was originally kept at 10 mTorr based on prior research, but the conclusion was made that stronger adhesion was a higher priority for making a practical metamaterial. [46] Raising the power applied to the BST target could help with adhesion while increasing its deposition rate.

The deposition rate of silver was calculated again based on the data from samples E-2 and E-3. The results came out to 12 nm per minute, shown in Table 5.14. Further testing could be done to account for the flow of nitrogen during silver deposition, but the result was accurate based on samples E-2 and E-3.

Table 5.14: Deposition Rate of Silver

Ag on Fused Silica				
Deposition Rate	Power (W)	Pressure (mTorr)	Gas	Flow (sccm)
12 nm / minute	40	5	Nitrogen	15

5.2.6 Group F

With a working deposition rate of silver, depositions could be focused on finding the deposition rate of BST. Group F samples were again deposited as a single layer of BST between two layers of silver. The recipe for silver was adjusted to create a 20 nm layer of silver. Instead of having all samples measured for BST and waiting several days on the results, the samples were inspected visually. The layers of silver were transparent enough to notice a change in color. By keeping all silver depositions equal, the difference should be noticeable.

Table 5.15: Group F - Silver and BST Recipes

Ag and BST on Fused Silica							
Sample	Ag (1st & 3rd Layer)			BST (2nd Layer)			
	Power (W)	Pressure (mTorr)	Time (Seconds)	Power (W)	Pressure (mTorr)	Time (Seconds)	Visible Layer
F-1	40	5	100	70	10	1200	
F-2	40	5	100	40	5	300	
F-3	40	5	100	40	5	900	
F-4	40	5	100	60	5	1500	✓
F-5	40	5	100	70	5	1500	✓
F-6	40	5	100	80	5	1500	✓
F-7	40	5	100	60	5	2100	✓
F-8	40	5	100	70	5	2100	✓
F-9	40	5	100	80	5	2100	✓
F-10	40	5	100	50	5	1500	
*	Nitrogen: 15 sccm			Argon: 10 sccm			

Samples F-4 through F-9 were the only samples with visible BST film. Samples F-6 and F-9 appeared darker than the others. Before sending out all samples for testing, sample F-9 was sent first to avoid requesting an etch depth that is not deep enough. The maximum etch depth was set at 88.5 nm.

The F-9 plots showed counts smaller than previous results. The oxygen plot, in Figure 5.56, did not show the binding energy shift, however the upward slope at the start of the shift is visible past 85 nm so an approximate total thickness of 85 nm is assumed for sample F-9.

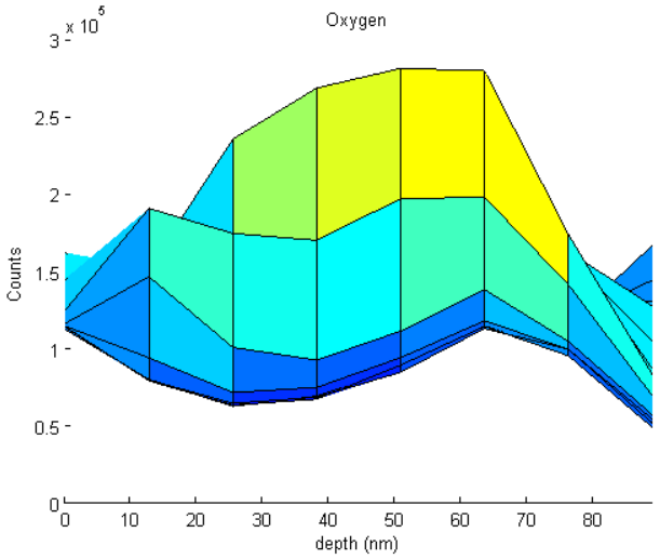

Figure 5.56: Sample F-9 Oxygen

The deposition rate of silver is confirmed in Figure 5.58 with layers at around 20 nm. The thickness of BST was estimated to be 45 nm. Samples F-4, F-5, F-7 and F-8 were sent to be measured with the XPS. Sample F-6 should have been sent as well, but similar results were expected for those four samples. At that time, 80 W was considered a high amount of power for sputtering BST.

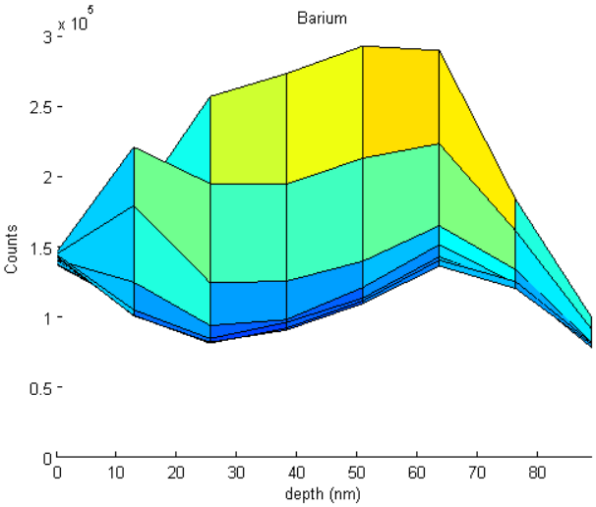

Figure 5.57: Sample F-9 Barium

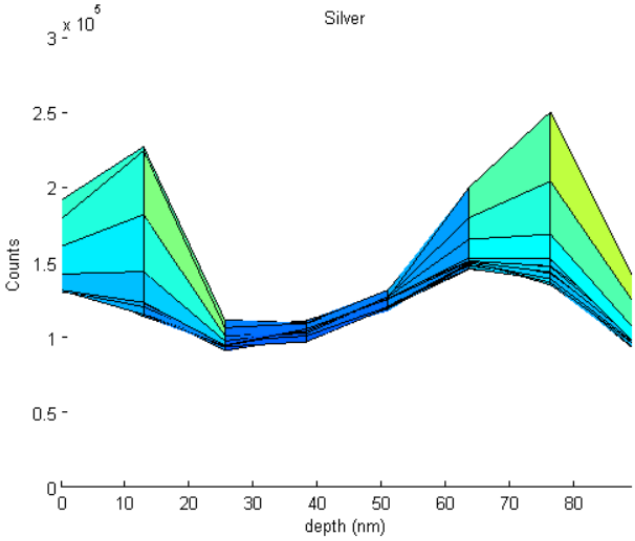

Figure 5.58: Sample F-9 Silver

For sample F-4, Figure 5.59 shows the shift for oxygen at around 24 nm. The structure should be more than 40 nm, accounting for the two silver layers. There is a small peak of silver at 5 nm, in Figure 5.61, but not as defined as in Figure 5.58 for sample F-9. Silver is also found at the center where only barium should have been detected. An expected sharp increase for barium is missing from Figure 5.60, meaning barium is found near the surface.

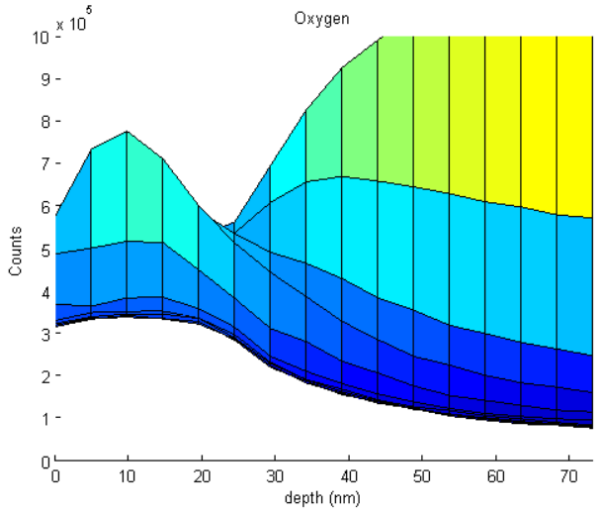

Figure 5.59: Sample F-4 Oxygen

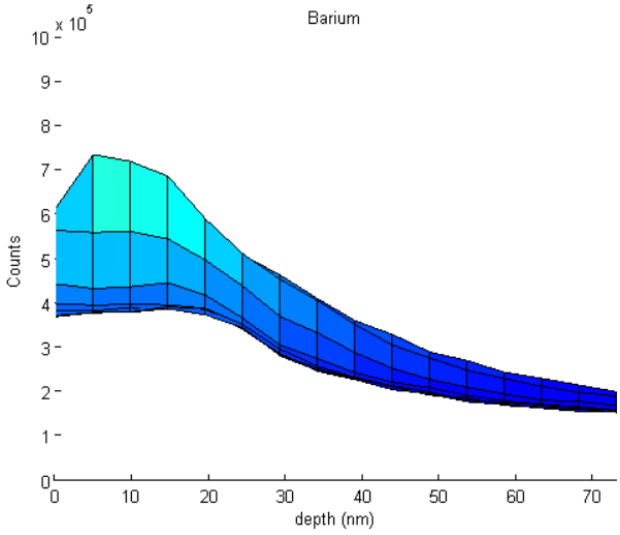

Figure 5.60: Sample F-4 Barium

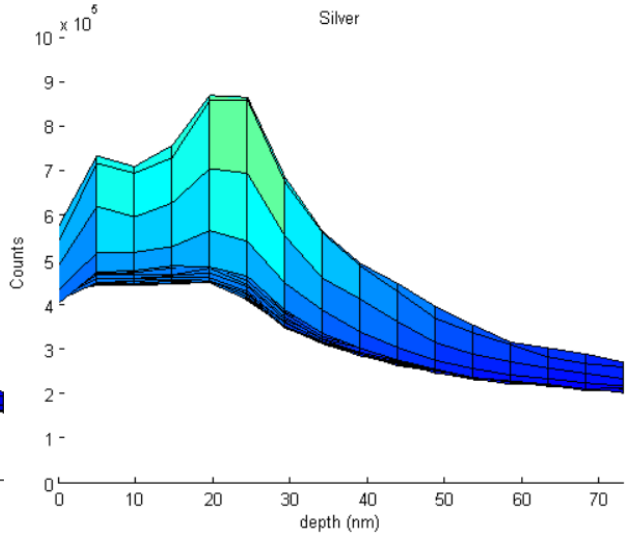

Figure 5.61: Sample F-4 Silver

Sample F-7 has a thickness of about 38 nm to 40 nm from comparing oxygen to silver. Figure 5.64 also shows that there is still silver where only the elements of BST should be found. Figure 5.62 shows some barium at the top of the deposition. With an increase in deposition rate between F-4 and F-7 from 25 minutes to 35 minutes, the total thickness was increased by 8 nm. Since the results were not similar to sample F-9 and the only difference was the power for BST, the conclusion can be made that 60 W is too small for a 2-inch target of BST.

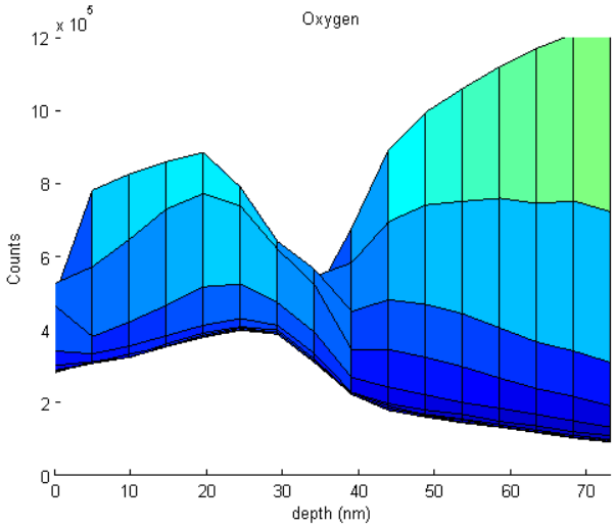

Figure 5.62: Sample F-7 Oxygen

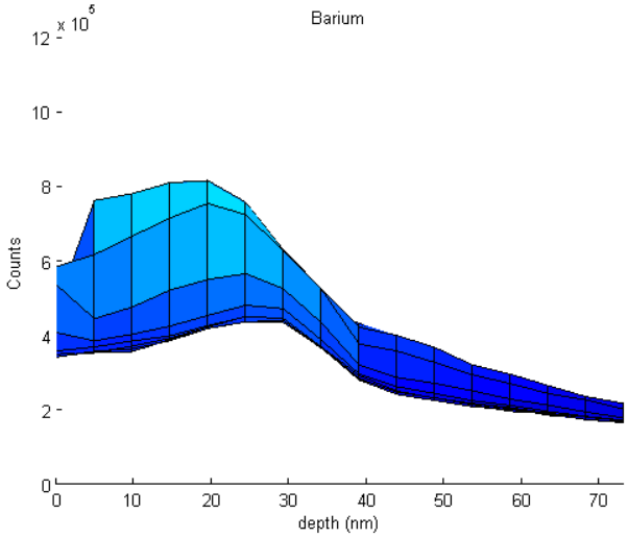

Figure 5.63: Sample F-7 Barium

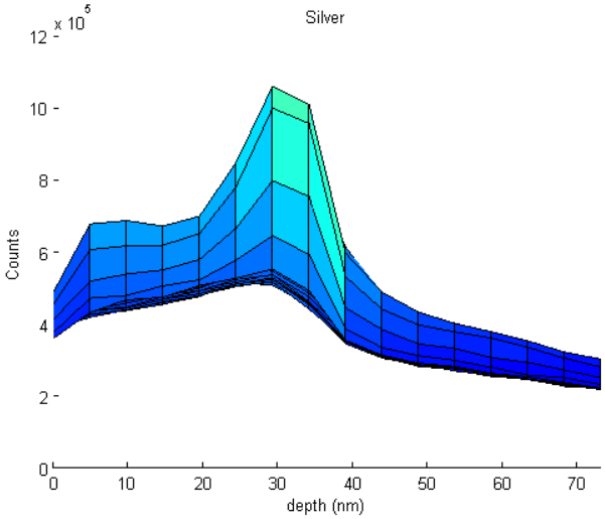

Figure 5.64: Sample F-7 Silver

Sample F-5 used 70 W for 25 minutes for sputtering BST. The thickness is about 38 nm from comparing oxygen and silver. The bottom layer of silver is around the 20 nm thickness as expected. Figure 5.66 still shows the problem of BST and the top layer of silver mixing together. Barium is still found at the top of the entire deposition. Initial conclusions show that even 70 W might not be suitable for BST deposition.

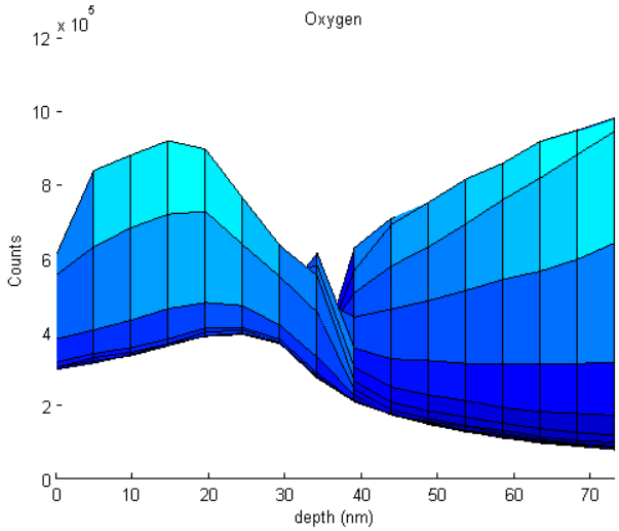

Figure 5.65: Sample F-5 Oxygen

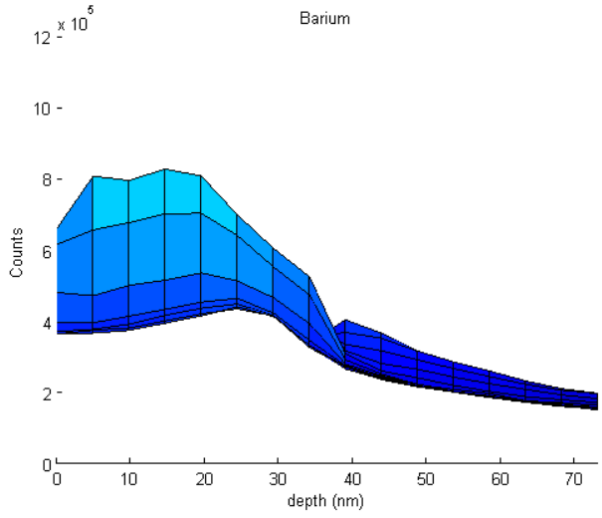

Figure 5.66: Sample F-5 Barium

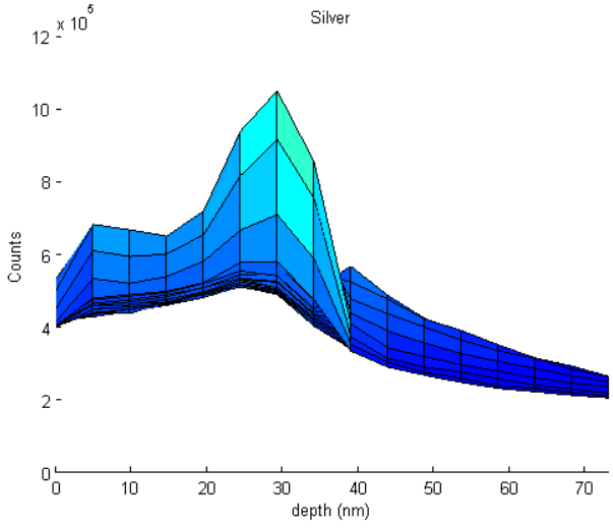

Figure 5.67: Sample F-5 Silver

Sample F-8 also uses 70 W, similar to sample F-5, but for 35 minutes. The total thickness appears to be 45 nm from comparing oxygen and silver. The peak for the top layer of silver in Figure 5.70 is missing. And just like sample F-5, barium is still found at the top. Even with a longer deposition, 70 W seems to be too low for sputtering BST as well. The power will have to be increased for future depositions.

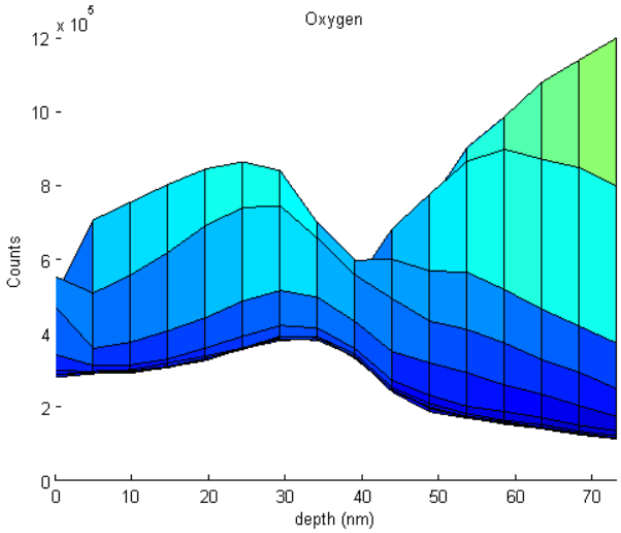

Figure 5.68: Sample F-8 Oxygen

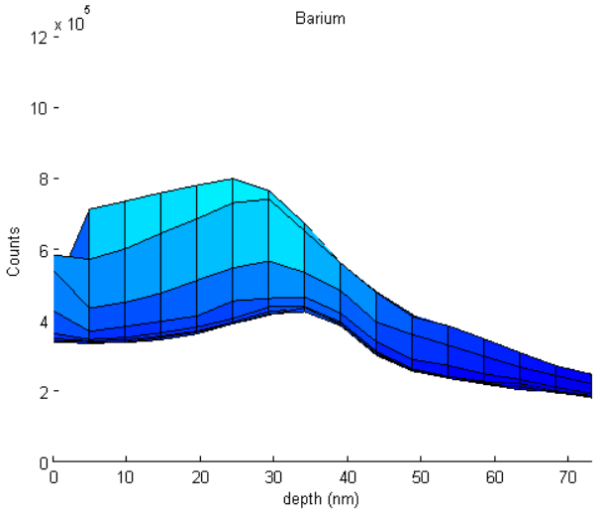

Figure 5.69: Sample F-8 Barium

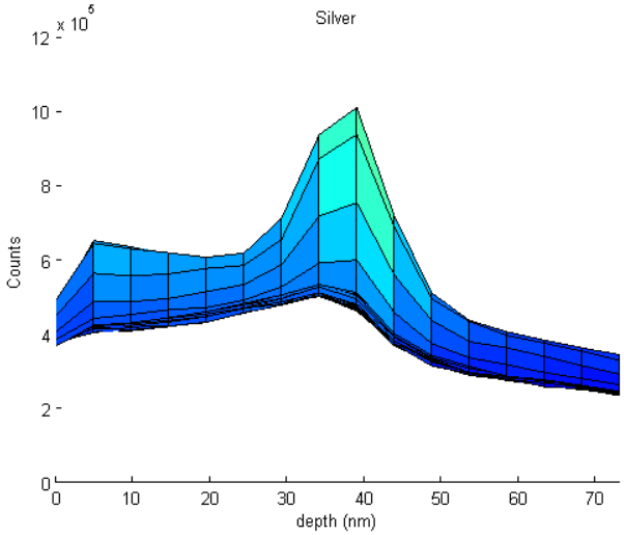

Figure 5.70: Sample F-8 Silver

5.3 Conclusions

The main conclusion from the Group F samples is that power below 80 W is too low for BST. Going back to Figures 5.56, 5.57 and 5.58, there is still some barium measured within the silver layer, but to a lesser degree than the 60 W and 70 W samples. This means that 80 W is still low but closer to the minimum power required for BST considering the drastic improvement between 70 W and 80 W. Other studies show power applied at higher values such as 150 W for a target diameter of 70 mm [48]. This would seem high for a 2-inch target. The power applied per area comes out to 3.8976 W per cm^2. For a 2-inch diameter target, the resulting power applied on the target would be 79 W which would be too low. A power of 150 W in only warranted if lesser power doesn't produce desired result. Based on the results for the target size, a power of 90 W or 100 W would be more appropriate with increases by 10 W if better results can be achieved. Low power can decrease the chance of a particle depositing on a substrate, but high power can accelerate particles too fast to a point where impacts on the BST surface can dislodge previously deposited particles out of the thin film [49]. This would create cavities in the layer.

CHAPTER VI

DISCUSSION AND FUTURE WORK

The results of the research showed that a hyperbolic metamaterial could be designed for the visible spectrum. The methods provided can be used in other designs where hyperbolic metamaterials or other anisotropic metamaterials are used in ultraviolet or infrared wavelengths.

The deposition of silver and barium strontium titanate (BST) multilayers can be continued at 90 W or 100 W with more study into the characteristics of the BST layer. Table 6.1 shows future trials for BST deposited on silver.

Table 6.1: BST Recipes

Sample	BST on Silver				
	Power (W)	Pressure (mTorr)	Time (Seconds)	Gas	Flow (sccm)
G-1	90	5	1200	Ar	10
G-2	100	5	1200	Ar	10
G-3	110	5	1200	Ar	10

Where only argon was used since oxygen was unavailable, the addition of oxygen during deposition is supposed to increase the refractive index of BST where oxygen vacancies are recovered [50]. If no oxygen is available, then future annealing should be performed in ambient pressure.

Other considerations for future samples would be to preheat the substrate to temperatures ranging from 300° C or 350° C before making depositions. [51]. Substrate temperatures at this range may lead to a denser layer of BST preventing silver from mixing into BST. Since BST has

to be annealed at temperatures above 700° C, the effects of thermal diffusion between silver and BST should be considered. Silver may be stable up to 650° C or 700° C depending on the dielectric [52]. Shorter annealing times may be required.

The refractive index of the final sample can be confirmed through spectroscopic ellipsometry or similar equipment. An ellipsometer can detect the refractive index of the individual layers.

The deposition rate of silver was successfully at 12 nm per minute for a minimum power of 40 W. The recipe was shared with other researchers for their own projects.

This research managed to produce a patent based on the finding of this research. The patent covers metamaterials produced with silver and barium strontium titanate designed as a multiple stack metal and dielectric metamaterial.

REFERENCES

[1] Veselago, V. G. (1967). Electrodynamics of substances with simultaneously negative and. Usp. fiz. nauk, 92, 517.

[2] Bait-Suwailam, M. (2019). Electromagnetic Field Interaction with Metamaterials. Electromagnetic Fields and Waves.

[3] Pendry, J. B., Holden, A. J., Stewart, W. J., & Youngs, I. (1996). Extremely Low Frequency Plasmons in Metallic Mesostructures. Physical Review Letters, 76(25), 4773–4776.

[4] Pendry, J. B., Holden, A. J., Robbins, D. J., & Stewart, W. J. (1999). Magnetism from conductors and enhanced nonlinear phenomena. IEEE Transactions on Microwave Theory and Techniques, 47(11), 2075–2084.

[5] Smith, D. R., Padilla, W. J., Vier, D. C., Nemat-Nasser, S. C., & Schultz, S. (2000). Composite Medium with Simultaneously Negative Permeability and Permittivity. Physical Review Letters, 84(18), 4184–4187.

[6] Shelby, R. A., Smith, D. R., & Schultz, S. (2001). Experimental verification of a negative index of refraction. *science*, *292*(5514), 77-79.

[7] Smith, D. R., & Schurig, D. (2003). Electromagnetic Wave Propagation in Media with Indefinite Permittivity and Permeability Tensors. *Physical Review Letters*, *90*(7).

[8] Cortes, C. L., Newman, W., Molesky, S., & Jacob, Z. (2012). Quantum nanophotonics using hyperbolic metamaterials. *Journal of Optics*, *14*(6), 063001.

[9] Ferrari, L., Wu, C., Lepage, D., Zhang, X., & Liu, Z. (2015). Hyperbolic metamaterials and their applications. Progress in Quantum Electronics, 40, 1–40.

[10] Papadakis, G. T., Fleischman, D., Davoyan, A., Yeh, P., & Atwater, H. A. (2018). Optical magnetism in planar metamaterial heterostructures. Nature Communications, 9(1).

[11] Guo, Y., Newman, W., Cortes, C. L., & Jacob, Z. (2012). Applications of Hyperbolic Metamaterial Substrates. Advances in OptoElectronics, 2012(12), 1–9.

[12] Korobkin, D., Neuner, B., Fietz, C., Jegenyes, N., Ferro, G., & Shvets, G. (2010). Measurements of the negative refractive index of sub-diffraction waves propagating in an indefinite permittivity medium. Optics Express, 18(22), 22734.

[13] Vulis, D. I., Reshef, O., Camayd-Muñoz, P., & Mazur, E. (2018). Manipulating the flow of light using Dirac-cone zero-index metamaterials. *Reports on Progress in Physics*, *82*(1), 012001.

[14] Basak, S., Bar-On, O., & Scheuer, J. (2021). Perovskite/Metal-Based Hyperbolic Metamaterials: Tailoring the Permittivity Properties of Coexisting Anisotropies in the Visible Region. Advanced Optical Materials, 9(1), 2001305.

[15] Stenzel, O. (2016). The Physics of Thin Film Optical Spectra. In *Springer Series in Surface Sciences*. Springer International Publishing.

[16] Peatross, J., & Ware, M. (2015). *Physics of light and optics*. Brigham Young University, Department of Physics.

[17] Saleh, B. E., & Teich, M. C. (2019). *Fundamentals of photonics*. john Wiley & sons.

[18] Javani, M. H., & Stockman, M. I. (2016). Real and Imaginary Properties of Epsilon-Near-Zero Materials. Physical Review Letters, 117(10).

[19] Caligiuri, V., Dhama, R., Sreekanth, K. V., Strangi, G., & De Luca, A. (2016). Dielectric singularity in hyperbolic metamaterials: the inversion point of coexisting anisotropies. *Scientific Reports*, *6*(1).

[20] Drachev, V. P., Podolskiy, V. A., & Kildishev, A. V. (2013). Hyperbolic metamaterials: new physics behind a classical problem. Optics Express, 21(12), 15048.

[21] Fullager, D. B., & Fiddy, M. A. (2015). Design theory of thin film hyperbolic metamaterial collimators. *Metamaterials, Metadevices, and Metasystems 2015*.

[22] Papadakis, G. T., Yeh, P., & Atwater, H. A. (2015). Retrieval of material parameters for uniaxial metamaterials. *Physical Review B*, *91*(15).

[23] Akafzade, H., & Sharma, S. C. (2020). New metamaterial as a broadband absorber of sunlight with extremely high absorption efficiency. AIP Advances, 10(3), 035209.

[24] Kim, M., & Rho, J. (2015). Metamaterials and imaging. *Nano Convergence*, *2*(1).

[25] Shen, L., Lin, X., Shalaginov, M. Y., Low, T., Zhang, X., Zhang, B., & Chen, H. (2020). Broadband enhancement of on-chip single-photon extraction via tilted hyperbolic metamaterials. Applied Physics Reviews, 7(2), 021403.

[26] Shekhar, P., Atkinson, J., & Jacob, Z. (2014). Hyperbolic metamaterials: fundamentals and applications. *Nano Convergence, 1*(1).

[27] Poddubny, A., Iorsh, I., Belov, P., & Kivshar, Y. (2013). Hyperbolic metamaterials. Nature Photonics, 7(12), 948–957.

[28] Avendaño-Alejo, M., & Rosete-Aguilar, M. (2006). Optical path difference in a plane-parallel uniaxial plate. JOSA A, 23(4), 926-932.

[29] Naik, G. V., Shalaev, V. M., & Boltasseva, A. (2013). Alternative Plasmonic Materials: Beyond Gold and Silver. *Advanced Materials*, *25*(24), 3264–3294.

[30] Naik, G. V., Schroeder, J. L., Ni, X., Kildishev, A. V., Sands, T. D., & Boltasseva, A. (2012). Titanium nitride as a plasmonic material for visible and near-infrared wavelengths. Optical Materials Express, 2(4), 478.

[31] Jellison, G. E., Boatner, L. A., Budai, J. D., Jeong, B.-S., & Norton, D. P. (2003). Spectroscopic ellipsometry of thin film and bulk anatase (TiO2). *Journal of Applied Physics*, *93*(12), 9537–9541.

[32] Chia, W.-K., Chen, Y.-C., Yang, C.-F., Young, S.-L., Chiang, W.-T., & Tsai, Y.-T. (2006). Characteristics of Bi4Ti3O12 thin films on ITO/glass and Pt/Si substrates prepared by R.F. sputtering and rapid thermal annealing. *Journal of Electroceramics*, *17*(2-4), 173–177.

[33] Ranjbar. (2018). Fabrication of Bismuth Titanate (Bi4Ti3O12) Thin Films: Effect of Annealing Temperature on their Structural and Optical Properties. *Scientia Iranica, 0*(0).

[34] Burnside, S., Moser, Jacques-E., Brooks, K., Grätzel, M., & Cahen, D. (1999). Nanocrystalline Mesoporous Strontium Titanate as Photoelectrode Material for Photosensitized Solar Devices: Increasing Photovoltage through Flatband Potential Engineering. *The Journal of Physical Chemistry B*, *103*(43), 9328–9332.

[35] Maneeshya, L. V., Anitha, V. S., Thomas, P. V., & Joy, K. (2015). Thickness dependence of structural, optical and luminescence properties of BaTiO3 thin films prepared by RF magnetron sputtering. *Journal of Materials Science: Materials in Electronics*, *26*(5), 2947–2954.

[36] Wang, J., Xiang, J., Duo, S., Li, W., Li, M., & Bai, L. (2008). Microstructure, optical and dielectric properties of compositional graded (Ba, Sr)TiO3 thin films derived by RF magnetron sputtering. *Journal of Materials Science: Materials in Electronics*, *20*(4), 319–322.

[37] Sharma, P. K., Messing, G. L., & Agrawal, D. K. (2005). Structural, ultraviolet-shielding, dielectric and ferroelectric properties of Ba1−xSrxTiO3 (x=0.35) thin films prepared by sol-gel method in presence of pyrrole. *Thin Solid Films*, *491*(1-2), 204–211.

[38] Venkata Saravanan, K., Sudheendran, K., Ghanashyam Krishna, M., James Raju, K. C., & Bhatnagar, A. K. (2006). Effect of process parameters and post deposition annealing on the optical, structural and microwave dielectric properties of RF magnetron sputtered (Ba0.5,Sr0.5)TiO3 thin films. *Vacuum*, *81*(3), 307–316.

[39] Panda, B., Dhar, A., Nigam, G. D., Bhattacharya, D., & Ray, S. K. (1998). Optical properties of RF sputtered strontium substituted barium titanate thin films. *Thin Solid Films*, *332*(1-2), 46–49.

[40] Rakić, A. D., Djurišić, A. B., Elazar, J. M., & Majewski, M. L. (1998). Optical properties of metallic films for vertical-cavity optoelectronic devices. *Applied Optics*, *37*(22), 5271.

[41] Sweatlock, L.A. (2008). Plasmonics: Numerical Methods and Device Applications.

[42] Wemple, S. H., Didomenico Jr, M., & Camlibel, I. (1968). Dielectric and optical properties of melt-grown BaTiO3. Journal of Physics and Chemistry of Solids, 29(10), 1797-1803.

[43] Xu, T., Agrawal, A., Abashin, M., Chau, K. J., & Lezec, H. J. (2013). All-angle negative refraction and active flat lensing of ultraviolet light. *Nature*, *497*(7450), 470–474.

[44] Wongkasem, N., & Ochoa, A. (2020). Method for fabricating a hyperbolic metamaterial having a near-zero refractive index in the optical regime (Patent Applicaton 20200036099A1) U.S. Patent and Trademark Office.

[45] Thompson, A. C., Berkeley, L., & Berkeley, L. (2009). X-ray data booklet (3rd ed.). Lawrence Berkeley National Laboratory, University of California.

[46] Bayrak, T., Ozgit-Akgun, C., & Goldenberg, E. (2017). Structural, optical and electrical characteristics BaSrTiOx thin films: Effect of deposition pressure and annealing. *Journal of Non-Crystalline Solids*, *475*, 76–84.

[47] Venkata Saravanan, K., & James Raju, K. C. (2013). Quasi-rapid thermal annealing studies on barium strontium titanate thin films deposited on fused silica substrates. *Journal of Alloys and Compounds*, *571*, 43–49.

[48] Li, S. Z., Yang, Y. Q., Liu, L., Liu, W. C., & Wang, S. B. (2008). The preparation and refractive index of BST thin films. Physica B: Condensed Matter, 403(17), 2618–2623.

[49] Gao, F., & An, J. (2016, October). BST thin films deposited by RF-magnetron sputtering and dielectric property research. In 2016 IEEE Advanced Information Management, Communicates, Electronic and Automation Control Conference (IMCEC) (pp. 1808-1811). IEEE.

[50] Zhang, R.-B., Yang, C.-S., & Ding, G.-P. (2005). The effects of oxygen partial pressure on BST thin films deposited on multilayered bottom electrodes. Materials Letters, 59(14-15), 1741–1744.

[51] Jha, G. C., Ray, S. K., & Manna, I. (2008). Effect of deposition temperature on the microstructure and electrical properties of Ba0.8Sr0.2TiO3 thin films deposited by radio-frequency magnetron sputtering. Thin Solid Films, 516(10), 3416–3421.

[52] Alford, T. L., Chen, L., & Gadre, K. S. (2003). Stability of silver thin films on various underlying layers at elevated temperatures. *Thin Solid Films, 429*(1-2), 248–254.

APPENDIX

APPENDIX

DERIVATIONS

Refractive Index of Extraordinary Wave Vector

$$n_{t,e}(\theta) = \frac{n_{\parallel} \cdot n_{\perp}}{\sqrt{n_{\parallel}^2 \cdot sin^2(\theta) + n_{\perp}^2 \cdot cos^2(\theta)}} \quad \text{A.1}$$

Snell's Law for Extraordinary Wave Vector

$$n_i \cdot \sin(\theta_i) = n_{t,e}(\theta) \cdot sin\left(\theta_{t,e}\right) \quad \text{A.2}$$

Equation A.1 substituted into Equation A.2

$$n_i \cdot \sin(\theta_i) = \left(\frac{n_{\parallel} \cdot n_{\perp}}{\sqrt{n_{\parallel}^2 \cdot sin^2\left(\theta_{t,e}\right) + n_{\perp}^2 \cdot cos^2\left(\theta_{t,e}\right)}} \right) \cdot sin\left(\theta_{t,e}\right) \quad \text{A.3}$$

$$n_i \cdot \sin(\theta_i) = \left(\frac{n_{\parallel} \cdot n_{\perp}}{\sqrt{n_{\parallel}^2 \cdot sin^2\left(\theta_{t,e}\right) + n_{\perp}^2 \cdot cos^2\left(\theta_{t,e}\right)}} \right) \cdot sin\left(\theta_{t,e}\right) \cdot \left(\frac{\frac{1}{sin\left(\theta_{t,e}\right)}}{\frac{1}{sin\left(\theta_{t,e}\right)}} \right) \quad \text{A.4}$$

$$n_i \cdot \sin(\theta_i) = \left(\frac{n_{\parallel} \cdot n_{\perp}}{\sqrt{n_{\parallel}^2 \cdot \frac{sin^2\left(\theta_{t,e}\right)}{sin^2\left(\theta_{t,e}\right)} + n_{\perp}^2 \cdot \frac{cos^2\left(\theta_{t,e}\right)}{sin^2\left(\theta_{t,e}\right)}}} \right) \cdot \frac{sin\left(\theta_{t,e}\right)}{sin\left(\theta_{t,e}\right)} \quad \text{A.5}$$

$$n_i \cdot \sin(\theta_i) = \left(\frac{n_\parallel \cdot n_\perp}{\sqrt{n_\parallel^2 + n_\perp^2 \cdot \frac{1}{tan^2(\theta_{t,e})}}} \right) \quad \text{A.6}$$

$$\sqrt{n_\parallel^2 + \frac{n_\perp^2}{tan^2(\theta_{t,e})}} \cdot n_i \cdot \sin(\theta_i) = n_\parallel \cdot n_\perp \quad \text{A.7}$$

$$\sqrt{n_\parallel^2 + \frac{n_\perp^2}{tan^2(\theta_{t,e})}} = \frac{n_\parallel \cdot n_\perp}{n_i \cdot \sin(\theta_i)} \quad \text{A.8}$$

$$\left[\sqrt{n_\parallel^2 + \frac{n_\perp^2}{tan^2(\theta_{t,e})}} \right]^2 = \left[\frac{n_\parallel \cdot n_\perp}{n_i \cdot \sin(\theta_i)} \right]^2 \quad \text{A.9}$$

$$n_\parallel^2 + \frac{n_\perp^2}{tan^2(\theta_{t,e})} = \frac{n_\parallel^2 \cdot n_\perp^2}{n_i^2 \cdot sin^2(\theta_i)} \quad \text{A.10}$$

$$\frac{n_\perp^2}{tan^2(\theta_{t,e})} = \frac{n_\parallel^2 \cdot n_\perp^2}{n_i^2 \cdot sin^2(\theta_i)} - n_\parallel^2 \quad \text{A.11}$$

$$\frac{n_\perp^2}{tan^2(\theta_{t,e})} = \frac{n_\parallel^2 \cdot n_\perp^2}{n_i^2 \cdot sin^2(\theta_i)} - n_\parallel^2 \cdot \frac{n_i^2 \cdot sin^2(\theta_i)}{n_i^2 \cdot sin^2(\theta_i)} \quad \text{A.12}$$

$$\frac{n_\perp^2}{tan^2(\theta_{t,e})} = \frac{n_\parallel^2 \cdot n_\perp^2 - n_\parallel^2 \cdot n_i^2 \cdot sin^2(\theta_i)}{n_i^2 \cdot sin^2(\theta_i)} \quad \text{A.13}$$

$$\frac{1}{tan^2(\theta_{t,e})} = \frac{1}{n_\perp^2} \cdot \frac{n_\parallel^2 \cdot n_\perp^2 - n_\parallel^2 \cdot n_i^2 \cdot sin^2(\theta_i)}{n_i^2 \cdot sin^2(\theta_i)} \quad \text{A.14}$$

$$\frac{1 - sin^2(\theta_{t,e})}{sin^2(\theta_{t,e})} = \frac{n_\parallel^2 \cdot n_\perp^2 - n_\parallel^2 \cdot n_i^2 \cdot sin^2(\theta_i)}{n_\perp^2 \cdot n_i^2 \cdot sin^2(\theta_i)} \quad \text{A.15}$$

$$\frac{1}{sin^2(\theta_{t,e})} - \frac{sin^2(\theta_{t,e})}{sin^2(\theta_{t,e})} = \frac{n_{\parallel}^2 \cdot n_{\perp}^2 - n_{\parallel}^2 \cdot n_i^2 \cdot sin^2(\theta_i)}{n_{\perp}^2 \cdot n_i^2 \cdot sin^2(\theta_i)} \quad \text{A.16}$$

$$\frac{1}{sin^2(\theta_{t,e})} - 1 = \frac{n_{\parallel}^2 \cdot n_{\perp}^2 - n_{\parallel}^2 \cdot n_i^2 \cdot sin^2(\theta_i)}{n_{\perp}^2 \cdot n_i^2 \cdot sin^2(\theta_i)} \quad \text{A.17}$$

$$\frac{1}{sin^2(\theta_{t,e})} = \frac{n_{\parallel}^2 \cdot n_{\perp}^2 - n_{\parallel}^2 \cdot n_i^2 \cdot sin^2(\theta_i)}{n_{\perp}^2 \cdot n_i^2 \cdot sin^2(\theta_i)} + 1 \quad \text{A.18}$$

$$\frac{1}{sin^2(\theta_{t,e})} = \frac{n_{\parallel}^2 \cdot n_{\perp}^2 - n_{\parallel}^2 \cdot n_i^2 \cdot sin^2(\theta_i)}{n_{\perp}^2 \cdot n_i^2 \cdot sin^2(\theta_i)} + \frac{n_{\perp}^2 \cdot n_i^2 \cdot sin^2(\theta_i)}{n_{\perp}^2 \cdot n_i^2 \cdot sin^2(\theta_i)} \quad \text{A.19}$$

$$\frac{1}{sin^2(\theta_{t,e})} = \frac{n_{\parallel}^2 \cdot n_{\perp}^2 - n_{\parallel}^2 \cdot n_i^2 \cdot sin^2(\theta_i) + n_{\perp}^2 \cdot n_i^2 \cdot sin^2(\theta_i)}{n_{\perp}^2 \cdot n_i^2 \cdot sin^2(\theta_i)} \quad \text{A.20}$$

$$sin^2(\theta_{t,e}) = \frac{n_{\perp}^2 \cdot n_i^2 \cdot sin^2(\theta_i)}{n_{\parallel}^2 \cdot n_{\perp}^2 - n_{\parallel}^2 \cdot n_i^2 \cdot sin^2(\theta_i) + n_{\perp}^2 \cdot n_i^2 \cdot sin^2(\theta_i)} \quad \text{A.21}$$

$$sin^2(\theta_{t,e}) = \frac{n_{\perp}^2 \cdot n_i^2 \cdot sin^2(\theta_i)}{n_{\parallel}^2 \cdot n_{\perp}^2 + (-n_{\parallel}^2 + n_{\perp}^2) \cdot n_i^2 \cdot sin^2(\theta_i)} \quad \text{A.22}$$

$$sin^2(\theta_{t,e}) = \frac{n_{\perp}^2 \cdot n_i^2 \cdot sin^2(\theta_i)}{n_{\parallel}^2 \cdot n_{\perp}^2 + (n_{\perp}^2 - n_{\parallel}^2) \cdot n_i^2 \cdot sin^2(\theta_i)} \quad \text{A.23}$$

$$sin^2(\theta_{t,e}) = \left(\frac{\frac{1}{n_{\perp}^2}}{\frac{1}{n_{\perp}^2}} \right) \cdot \frac{n_{\perp}^2 \cdot n_i^2 \cdot sin^2(\theta_i)}{n_{\parallel}^2 \cdot n_{\perp}^2 + (n_{\perp}^2 - n_{\parallel}^2) \cdot n_i^2 \cdot sin^2(\theta_i)} \quad \text{A.24}$$

$$sin^2(\theta_{t,e}) = \frac{n_i^2 \cdot sin^2(\theta_i)}{n_{\parallel}^2 + \frac{(n_{\perp}^2 - n_{\parallel}^2)}{n_{\perp}^2} \cdot n_i^2 \cdot sin^2(\theta_i)} \quad \text{A.25}$$

$$\sqrt{sin^2(\theta_{t,e})} = \sqrt{\frac{n_i^2 \cdot sin^2(\theta_i)}{n_{\parallel}^2 + \left(\frac{n_{\perp}^2 - n_{\parallel}^2}{n_{\perp}^2}\right) \cdot n_i^2 \cdot sin^2(\theta_i)}} \quad \text{A.26}$$

$$sin(\theta_{t,e}) = \frac{n_i \cdot sin(\theta_i)}{\sqrt{n_{\parallel}^2 + \left(\frac{n_{\perp}^2 - n_{\parallel}^2}{n_{\perp}^2}\right) \cdot n_i^2 \cdot sin^2(\theta_i)}} \quad \text{A.27}$$

$$\sqrt{n_{\parallel}^2 + \left(\frac{n_{\perp}^2 - n_{\parallel}^2}{n_{\perp}^2}\right) \cdot n_i^2 \cdot sin^2(\theta_i)} \cdot sin(\theta_{t,e}) = n_i \cdot sin(\theta_i) \quad \text{A.28}$$

Snell's Law for Uniaxial Crystals with Optic Axis Parallel to Z-axis

$$n_i \cdot sin(\theta_i) = \sqrt{n_{\parallel}^2 + \left(\frac{n_{\perp}^2 - n_{\parallel}^2}{n_{\perp}^2}\right) \cdot sin^2(\theta_i)} \cdot sin(\theta_{t,e}) \quad \text{A.29}$$

Refractive Index of Extraordinary Wave Vector

$$n_{t,e}(\theta_i) = \sqrt{n_{\parallel}^2 + \left(\frac{n_{\perp}^2 - n_{\parallel}^2}{n_{e\perp}^2}\right) \cdot n_i^2 \cdot sin^2(\theta_i)} \quad \text{A.30}$$

BIOGRAPHICAL SKETCH

Andres Ochoa attended the University of Texas Pan American earning a Bachelor of Science in Electrical Engineering in 2008. Andres later enrolled in a Master of Science degree program at the University of Texas Rio Grande Valley focusing on electromagnetics, antennas, metamaterials and specializing in photonic metamaterials. Through internships, he has worked with government and industry experts involving program management of technological systems. Andres was awarded a Master of Science in Engineering degree in Electrical Engineering in December 2021. Email: aochoaz@yahoo.com